SELF-SUSPENDED NANOPARTICLE FLUIDS

A Dissertation

Presented to the Faculty of the Graduate School

of Cornell University

In Partial Fulfillment of the Requirements for the Degree of

Doctor of Philosophy

by

Praveen Agarwal

May, 2012

SELF-SUSPENDED NANOPARTICLE FLUIDS

Praveen Agarwal, Ph. D.

Cornell University 2012

This work undertakes the fundamental study of structure and dynamics of an entirely new class of organic-inorganic hybrid material created by densely grafting polymer chains to the nanoparticle surface. These systems can display fluid behavior even in the absence of any external solvent and have been termed as self-suspended nanoparticle fluids. This materials platform offers several technical opportunities and presents an entirely new system for fundamental studies. Nanoparticle volume fraction and tethered polymer molecular weight in this system can be changed in a straightforward way, allowing the structure and dynamics to be studied over a wide range. We have studied rheology, nanoparticle structure, tethered polymer dynamics and nanoparticle dynamics in this system to understand the governing interaction forces. Flow behavior has been studied by conventional steady and oscillatory shear rheology, nanoparticle structure has been studied by Small Angle X-ray Scattering (SAXS), tethered polymer dynamics has been studied by Broadband Dielectric Spectroscopy and Nanoparticle dynamics has been studied by X-ray Photon Correlation Spectroscopy (XPCS). We have discovered that these materials display characteristic rheological features of soft glassy materials and can be used as model systems to study soft colloidal glasses. In this work we have discovered several unexplored feature of soft glassy materials like the enhanced jamming with increasing temperature and accelerated dynamics with the application of shear strain. We have described our finding in the framework of soft glassy rheology (SGR) model. Tethered

polymers in this system exhibit unexpected slow relaxation dynamics irrespective of their low molecular weight, which resembles the features observed in highly entangled polymers. We have proposed a simple theoretical framework to describe the relaxation dynamics of densely grafted polymers that captures the observed behavior. Nanoparticle dynamics in these materials exhibits slow and hyperdiffusive behavior, which follows the similar trends observed in rheology, indicating that the particle dynamics primarily governs the rheology. We have further extended this platform to create hybrid polymer networks having nanoparticles as junction points. These polymer networks exhibit unprecedented mechanical properties and display shape memory properties.

BIOGRAPHICAL SKETCH

Praveen Agarwal was born in Agra, India. He was always interested in science and mathematics from his childhood. He went to Indian Institute of Technology, Bombay to pursue Bachelor of Technology in Chemical Engineering. During his undergraduate studies he was inspired to work on polymeric materials. He came to Cornell University to pursue his PhD in Chemical Engineering and worked on polymer nanoparticle hybrid materials.

Dedicated to my parents

ACKNOWLEDGMENTS

I would like to express my sincere gratitude to my advisor Professor Lynden Archer for his support and guidance throughout the course of my PhD. I have learned from him about several different aspects of research and life in general. His enthusiasm and positive attitude have been a source of great inspiration for me and always helped me overcome the difficult times during my PhD. I consider myself to be very fortunate to get a chance to work with him.

I appreciate the help from my committee members Professor Donald Koch, Professor Ulrich Wiesner and Professor Christopher Ober.

I would like to thank members of Archer group, Zhenyu Qian for teaching me anionic polymerization and Samanvaya Srivastava for working closely with me on many projects. I am grateful to the masters and undergraduate students Dawei Liu, Adnan Kapadia and Madhur Chopra for their help in my experimental work. I am thankful to all members of the Archer group for their supportive and collaborative nature. The friendly environment provided the group members has certainly made my stay here very enjoyable.

I am indebted to Dr. Suresh Narayanan at Advanced Photon Source for his expert assistance and advice on X-ray photon correlation spectroscopy measurements. Without his help, it would not have been possible to get the much needed insight into the nanoparticle dynamics of these systems.

I would like to thank Hsiu-yu Yu, Professor Fernando Escobedo and Sushmit Goyal for many valuable discussions. Work done by Koch and Escobedo group has greatly helped to my understanding of this system.

I want to express my gratitude to Dr.Yuanming Zhang at Cornell Center for Materials Research, and Dr. David Jung and Brenda Fisher at KAUST-CU center for energy and

sustainability for helping me with several experimental tools and techniques.

I would like to thank the funding agencies KAUST, NSF and CCMR for providing the financial support. The infrastructure support from KAUST-CU center for energy and sustainability and CCMR is highly appreciated.

TABLE OF CONTENTS

CHAPTER 1

Introduction

1.1 Polymer nanocomposites

Polymer nanocomposites are materials made by dispersing inorganic nanoparticles into polymer matrix [1-5], as shown in the schematic in figure 1.1. Polymer nanocomposites provide a unique combination of the functionality of inorganic nanoparticles and the processability of polymers, which has rendered them hosts of lot of commercial applications ranging from coating, packaging and flame retardants etc. Incorporation of inorganic nanoparticles also provides a pathway to incorporate electrical, optical and magnetic properties to the polymer matrix which can be further tuned by changing the weight fraction of the nanoparticles or the molecular weight of the polymer matrix. Potential advantages presented by polymer nanocomposites on both the scientific and technical fronts have led to an enormous amount of research activity in past few decades [1-5]. Surge in the research activity in polymer nanocomposites is also due to great advances in the synthetic schemes of inorganic nanoparticles [6, 7], which has made possible the design of nanocomposites with filler length scale dependent properties [8].

Nanoparticle fillers provide significant property improvement as compared to the conventional fillers due to their high surface area to volume ratio, however, owing to their small size, nanoparticles tend to irreversibly aggregate due to strong Van der Walls attractive forces [9, 10]. Dispersion of nanoparticle in the polymer matrix still remains a substantial challenge, hindering the complete utilization of the potential technological applications of polymer nanocomposites. Grafting polymers to the nanoparticle surface provides one effective strategy to mix the inorganic nanoparticles with the polymer matrix, nevertheless the phase space for miscibility of the grafted nanoparticles and dispersing polymer matrix is often limited depending on the ratio of the molecular weight of the grafted and the matrix polymer chain [11, 12]. This calls for a unique materials platform that can avoid the miscibility issue between the inorganic nanoparticles phase

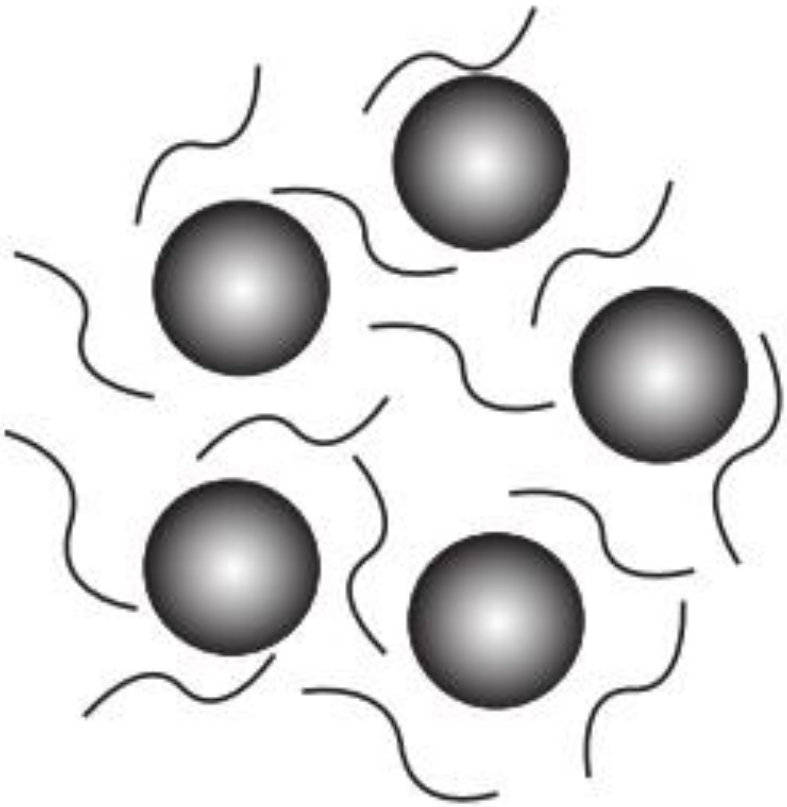

Figure 1.1 Schematic description of a polymer nanocomposite.

and the organic polymer phase and concurrently retains the potential advantages of the conventional nanocomposites.

1.2 Self suspended nanoparticle fluids

In the present work, we have mitigated the issue of nanoparticle aggregation and phase separation by creating a single phase nanocomposite, wherein the polymer matrix is chemically attached to the nanoparticle itself, as shown in the schematic in figure 1.2. We are particularly interested in the regime where the grafting density of the polymer chains is high, which enables these systems to display fluid like properties even in the absence of any external dispersing medium. These materials will henceforth be referred as self-suspended nanoparticle fluids, implying that the suspended phase and suspending phase are essentially the same. Physical properties of these systems can be continuously tuned by changing the polymer molecular weight and grafting density, allowing a wide spectrum of properties to be achieved. Moreover, taking advantage of the wide array of nanoparticle chemistries, these systems can be designed to exhibit the unique functional properties of inorganic nanoparticles [13-15].

More importantly, this platform is fundamentally unique, considering these materials are single component nanoparticle fluids. Core-core interactions in these systems are mediated by tethered polymer chains, which have to uniformly fill the interparticle space. Theoretical work of Yu et al. [16] has demonstrated that these self-suspended nanoparticles act as incompressible single component fluids, resulting in the structure factor, $S(q)$, which goes to zero in the limit of low wave vector, q. Owing to this fundamentally unique aspect, these materials present an entirely new materials platform for applications like carbon dioxide

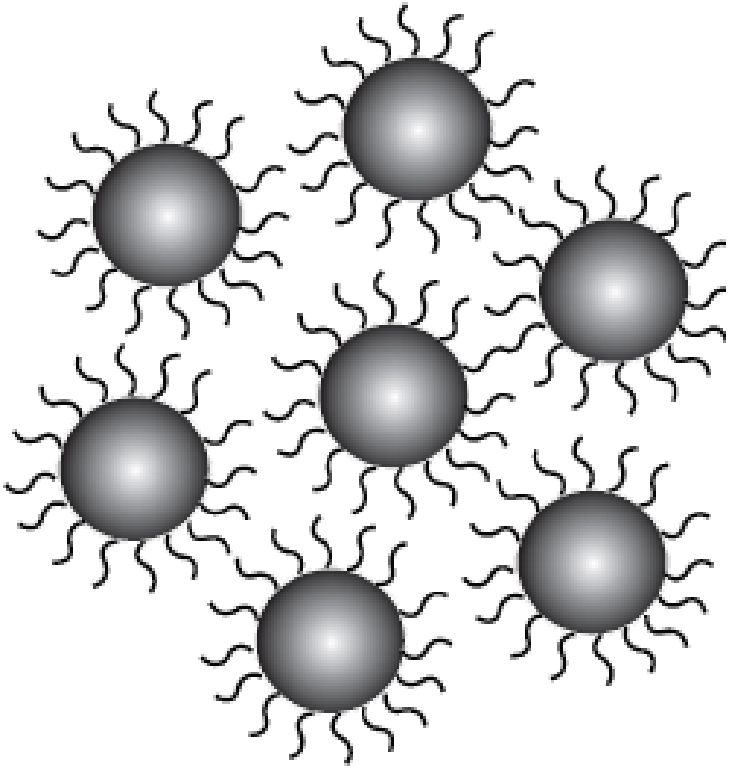

Figure 1.2 Schematic representation of the self-suspended fluids, showing polymer grafted nanoparticles with no additional solvent present.

capture, where the entropic frustration of the tethered polymer chains could be utilized to capture carbon dioxide.

1.3 Goals and methods

Self-suspended nanoparticle fluids present excellent targets for fundamental study. Present system can be visualized as a colloidal suspension wherein each particle carries its own share of fluid [16]. Furthermore it is a highly coupled system, where the polymer dynamics should be affected by the particle dynamics, which is in turn mediated by the polymers filling the interparticle space. Goal of the present study is to understand the interaction forces that govern the structure and dynamics of these systems. We have studied the rheology, polymer dynamics, nanoparticle structure and nanoparticle dynamics of these materials over a wide range of nanoparticle volume fraction, polymer molecular weight and temperature to understand the fundamental aspects of their structure and dynamics.

Furthermore, these self-suspended nanoparticle fluids can be used as model systems to understand a broad class of materials. As discussed in detail later, these materials have displayed characteristic features of soft colloidal glasses and serve as excellent model systems for soft glassy materials [17, 18]. Additionally, we have also used them as model systems to study polymers in confinement. Present system is analogous to a special case of branched polymers [19, 20] where the branch point is macroscopic in size and can be directly visualized with X-ray scattering techniques.

We have studied the flow behavior using conventional oscillatory and steady shear rheology. Nanoparticle structure has been studied using our in house Small Angle X-ray scattering

(SAXS) setup. Polymer dynamics has been studied by Broadband dielectric spectroscopy, using polyisoprene (PI) as the tethered chain, which allows global chain dynamics to be studied. Nanoparticle dynamics has been studied using X-ray photon correlation spectroscopy (XPCS) at Argonne national laboratory.

1.4 Self-suspended nanoparticle fluids as model system for colloidal glasses

Glass transition still remains one of the biggest unresolved puzzles of soft condensed matter physics [21-23]. Physics of glass transition and the slow dynamics of materials approaching glass transition still remain poorly understood [21-23]. Recently, it has been demonstrated that colloids can be used as model systems for glasses, which has led to significant advances in the understanding of glass transition considering the ease of visualization of colloidal glasses compared to molecular glasses [24-26]. Utility of hard sphere glasses as model systems for colloidal glasses is however limited due to their fragile behavior. Recently, it has been proposed that soft colloids provide a wider phase space for studying the glassy dynamics [27-29]. A key feature of soft glassy materials is the prominent maximum in the loss modulus, G'', in a strain sweep measurement [17, 18]. We have discovered that these self-suspended fluids display this characteristic feature of soft colloidal glasses. These materials therefore serve as ideal model systems for soft glasses which are composed of inorganic nanoparticle, allowing the particle structure and dynamics to be probed separately in a scattering experiment.

A significant advantage of the present system over conventional soft glassy materials is the absence of any temporal dependence of material properties under quiescent conditions, usually termed as aging [30-32]. Effect of aging introduces an extra variable of waiting time while studying the rheology soft glassy materials and intermixes the system dynamics with

the aging kinetics. Presumably owing to their spatial homogeneity, the current systems exhibit negligible aging effects and allow the properties of soft glassy material to be studied, decoupled from aging. Additionally, these systems are attractive as model systems for colloidal glasses due to absence of any enthalpic effects between the suspending and the suspended phase, which allows the effect of temperature on the rheology to be studied.

1.5 Self-suspended nanoparticle fluids as model systems for polymers in confinement

Even after decades of scientific study, dynamics of polymers in confinement is not clearly understood. In some of the very early works it was demonstrated that glass transition temperature, T_g, of a molecular glass former depends on the degree of confinement [33]. Subsequently, several studies have revealed acceleration or retardation of polymer dynamics due to confinement [34-36]. A significant detail of physics of confined polymers has been revealed by studying the polymer thin films [37, 38]. Nevertheless, thin film measurements are difficult to perform and the interpretation of such measurements is always controversial due to the interfacial effect associated with polymer thin films, usually supported by a substrate. This inherent limitation has been avoided by using polymer nanocomposites as model systems for polymers in confinement [39, 40].

However, even with polymer nanocomposites there are limitations due to often poor dispersion of the inorganic nanoparticle into polymer matrix and enthalpic interactions between the dispersed phase and dispersing medium [41, 42]. Self-suspended nanoparticle studied here serve as ideal model systems to study polymers in confinement, wherein the degree of confinement can be changed by changing the polymer grafting density, molecular weight and the nanoparticle spacing. Enthalpic interaction between the dispersed phase and dispersing medium are absent due to the single component nature of these systems, which

allows the thermal properties to be studied over a wide range of temperature. Further, the biggest advantage of these systems is that they allow the confined polymer dynamics to be probed in a bulk experiment. Finally, the fluid like behavior of the materials studied here allows the comparison of rheology results with the separately probed polymer dynamics.

1.6 Applications based on hybrid nanoparticles

In the present work we have explored some of the applications of self-suspended fluids with an effort toward further extending this materials platform to create polymer networks. Polymer chain ends in these self-suspended fluids can be interconnected to form polymer networks which have nanoparticles as junction points, as opposed to small organic molecules in conventional polymer networks. Such hybrid polymer networks display unprecedented mechanical properties, where their elastic modulus is of the order 100 MPa. Additionally, these hybrid polymer networks are shape memory polymers which can be pre-programmed to remember a temporary shape and return to their original shape when acted upon by a stimulus. Shape memory polymers are an active class of polymers that can be used as implants for minimally invasive surgery, smart fabric and self-tightening sutures [43-46]. Present platform can potentially provide additional advantages like radio-opacity, high mechanical strength and remote actuation to the already existing properties of shape memory polymers.

1.7 Outline of this dissertation

In the present work, we have undertaken the study of fundamental aspects of structure and dynamics of self-suspended fluids. In chapter 2, we have proposed the concept of a self-suspended fluid and discussed the procedures followed to synthesize these materials. Further, we have tried to answer the questions whether the rheology of this system is close to a

polymer like behavior or a colloidal suspension by performing steady shear viscosity measurements for materials with different nanoparticle volume fraction and corona molecular weight. We also discuss an unusual finding in the nonlinear oscillatory shear rheology of these systems which provides access to long time rheology of jammed systems.

In chapter 3, we have described the study of the relaxation dynamics of the tethered polymer chains in these materials, using cis 1-4 polyisoprene as the tethered polymer chain. We have proposed a simple theory that provides estimate of the ratio of relaxation time of the tethered and untethered polymer.

In chapter 4, we have studied the rheology and nanoparticle dynamics of these systems at different temperature and nanoparticle volume fraction. Both rheology and nanoparticle dynamics follow similar trends and display intriguing features in the temperature dependence.

As mentioned previously, these self-suspended fluids have exhibited characteristic features of soft glassy materials. Chapter 5 describes the effect of temperature on the soft glassy rheology of these materials. We have found that irrespective of polymer chain chemistry, increase in temperature causes more jamming in the system. We have discussed our experimental findings within the framework of soft glassy rheology (SGR) model.

A characteristic feature of soft glassy materials is their slow dynamics. Chapter 6 describes the effect of deformation on the dynamics of soft glassy rheology of self suspended fluids made from a range of polymer chain chemistry. We have found that strain considerably accelerates the dynamics of these materials and this effect can be predicted from calculations from the SGR model. We have found an agreement between the experimental data and SGR model predictions.

Chapter 7 describes the synthesis and mechanical properties of the polymer networks synthesized by crosslinking the free end of the polymer chain in these materials. We show that these polymer networks have shape memory properties that could be utilized as biomedical implants for minimally invasive surgery.

REFERENCES

1. K. I. Winey, R.A. Vaia, MRS Bull. **32**, 314 (2007).
2. Q. Zhang, L. A. Archer, Langmuir **18**, 104335 (2002).
3. A. C. Balazs, T. Emrick, T. P. Russell, Science **314**, 1107 (2006).
4. E. P. Giannelis, R. Krishnamoorti, E. Manias, Prog. Polym. Sci. **138**, 107 (1999).
5. E. P. Giannelis, Adv. Mater. **8**, 29 (1996).
6. J. Park et al., Nature Mater. **3**, 891 (2004).
7. Y. G. Sun, Y. N. Xia, Science **298**, 2176 (2002).
8. S. A. Mcdonalds et al., Nature Mater. **4**, 138 U14 (2005).
9. M. E. Mackay et al., Science **311**, 1740 (2006).
10. P. Ackora et al., Nature Mater. **8**, 354 (2009).
11. N. Dutta, D. Green, Langmuir **24,** 5260 (2008).
12. J. H. Mass et al., Langmuir **18**, 8871 (2002).
13. A. B. Bourlinos, Adv. Mater **17**, 234 (2005).
14. R. Rodriguez, R. A. Herrera, L. A. Archer, E. P. Giannelis, Adv. Mater. **20**, 4353 (2008).
15. S. K. Goyal, F. A. Escobedo, J. Chem. Phys. **135**, 184902 (2011).
16. H.Y. Yu and D.L. Koch, Langmuir, **26**, 16801 (2010).
17. P. Sollich, Phys. Rev. E. **58**, 738 (1998).
18. P. Sollich et al., Phys. Rev. Lett. **78**, 2020 (1998).
19. W. W. Graessley, Adv. Polym. Sci. **47**, 67 (1982).
20. J. Klien, Macromolecules **19**, 105 (1986).
21. S. Torquato, Nature **450**, 521 (2000).
22. L. Berthier et al., Science **310**, 1797 (2005).

23. D. A. Weitz, Science **323**, 214 (2009).

24. P. N. Pusey and W. van Megen, Nature **320**, 340 (1986).

25. T. G. Mason and D. A. Weitz, Phys. Rev. Lett. **75**, 2770 (1995).

26. E. R. Weeks et al., Science **287**, 627 (2000).

27. J. Mattson et al. Nature **462**, 83 (2009).

28. C. A. Angell, K. L Ngai. G. B. Mckenna, P. F. Mcmillan, S. W. Martin, J. Appl. Phys. **88**, 3113 (2000).

29. A. J. Liu, S. R. Nagel, Nature **396**, 21 (1998).

30. G. B. Mckenna, T. Narita and F. Lequeux, J. Rheol. **53,** 489 (2009).

31. M. Warren, J. Rottler, Phys. Rev. Lett. **104**, 205501 (2010).

32. S. M. Fielding, P. Sollich, and M. E. Cates, J. Rheol. **44**, 323 (2000).

33. C. L. Jackson, G. B. Mckenna, J. Non. Cryst. Solids. **131**, 221 (1991).

34. J. L. Keddie, R. A. L. Jones, R. A. Cory, Europhys. Lett. **27**, 59 (1994).

35. Z. Yang, Y. Fujii, F. K. Lee, C.-H. Lam, C. O. Tsiu, Science **328**, 1676 (2010).

36. J. A. Forrest, K. D.-Veress, Adv. Colloid Interface Sci. **94**, 167 (2001).

37. C. J. Ellison, J. M. Torkelson, Nat. Mater. **2**, 695 (2003).

38. P. Rittigstein, R. D. Priestly, L. J. Broadbelt, J. M. Torkelson, Nat. Mater. **6**, 278 (2007).

39. E. P. Giannelis, R. Krishnamoorti, E Manias, Adv. Polym. Sci. **138**, 107 (1999).

40. A. Bansal, H. Yang., C. Li, K. Cho, B. C. Benicewicz, S. K. Kumar, L. S. Schalder, Nat. Mater. **4**, 693 (2005).

41. J. M. Kropka, V. G. Sakai, P. F. Green, Nano Lett. **8**, 1061 (2008).

42. L. Meli, P. F. Green, ACS Nano **6**, 1305 (2008).

43. A. Lendlein, A. M. Scmidt, R. Langer, Proc. Nat. Acad. Sci. **98**, 842 (2001).

44. A. Lendlein, S. Kelch, Angew. Chem. Int. Ed. **41**, 2034 (2002).

45. C. Liu, H. Qin, P. T. Mather, J. Mater. Chem. **17**, 1543 (2007).

46. P.T. Mather, X. Luo, R. Rousseau, Annu. Rev. Mater. Res. **39**, 441 (2009).

CHAPTER 2

The Ages in a Self-suspended Nanoparticle Liquid

Reproduced with permission from

Nano Lett. 10, 111 (2010)

P. Agarwal, H. Qi, L. A. Archer

2.1 Abstract

Telomers ionically tethered to nanometer-sized particles yield self-suspended nanoparticle-laden liquids with unusual dynamical features. By subjecting these suspensions to controlled, modest shear strains we find that their flow behaviors observed using experiments performed on timescales of tens of seconds can be projected to obtain maps of their dynamical response on geological timescales. That such extraordinarily slow dynamic processes can be uncovered from real-time measurements by simply stretching a system, provides a simple yet powerful tool for interrogating extremely slow motions in other jammed states.

2.2 Introduction

The effect of suspended particles on transport properties of liquids has been the subject of intense scientific interest since Einstein's seminal works [1, 2]. Historically, suspensions have played an important role in revealing thermal motion of molecules in fluids, in understanding colloidal forces and hydrodynamics of particles in liquids, for visualizing crystallization processes in solids and most recently for studying aging of glasses [3-6].

Here we report on a class of self-suspended nanoparticle liquids created by densely grafting charged telomers (short polymers) to the surface of inorganic nanoparticles. Termed Nanoscale ionic materials (NIMs) [7-9] these particle-laden fluids offer multiple handles through which near molecular-scale control can be exerted upon liquid-state physical properties. Because the suspending fluid, the organic corona, is permanently anchored to the particles, each particle can be thought of as carrying around its full share of the suspending liquid.

Polymer grafted nanoparticles have received significant, recent scientific attention in a variety of fields as novel platforms for polymer synthesis [10,11], studying dispersion and blending of

nanostructures in polymers [12-14], developing models for understanding the glass transition and rheology of jammed systems [15-18] and studying self-assembly in nanoparticle-polymer hybrids [19, 20]. Although these studies have generally focused on systems where: (a) long polymer chains are grafted at low/modest areal densities on the nanoparticle surface; and (b) the nanoparticle-polymer hybrids interact via a simple fluid or untethered polymeric host, a plethora of new phenomena have already been reported [12-20]. The list includes formation of anisotropic phases from isotropic nanostructures due to entropic effects of the tethered chains, non-Einstein dependence of suspension viscosity on particle volume fraction due to free volume effects of nanoparticles, tunable glass transition temperatures due to tethered and free polymer interactions in composites, and metal nanoparticle self-assembly into mesoporous phases templated by diblock copolymers [12-20].

2.3 Results and Discussion

In the present study we consider an arguably simpler material system in which telomers are densely grafted onto silica nanoparticles to create self-suspended nanoparticle liquids. Because the suspending medium and suspended particles are one and the same, this arrangement removes complications arising from free polymer-particle, and free-polymer tethered-polymer interactions [13-17], but simultaneously introduces strong correlations between grafted chains and their nanoparticle support. The results reported in this letter focus on silica nanoparticles (diameter = 10 ± 2 nm, surface area 300 nm^2.) functionalized with a dense brush (~150 chains/particle) of polyethylene glycol chains with a range of molecular weights (Table 2.1).

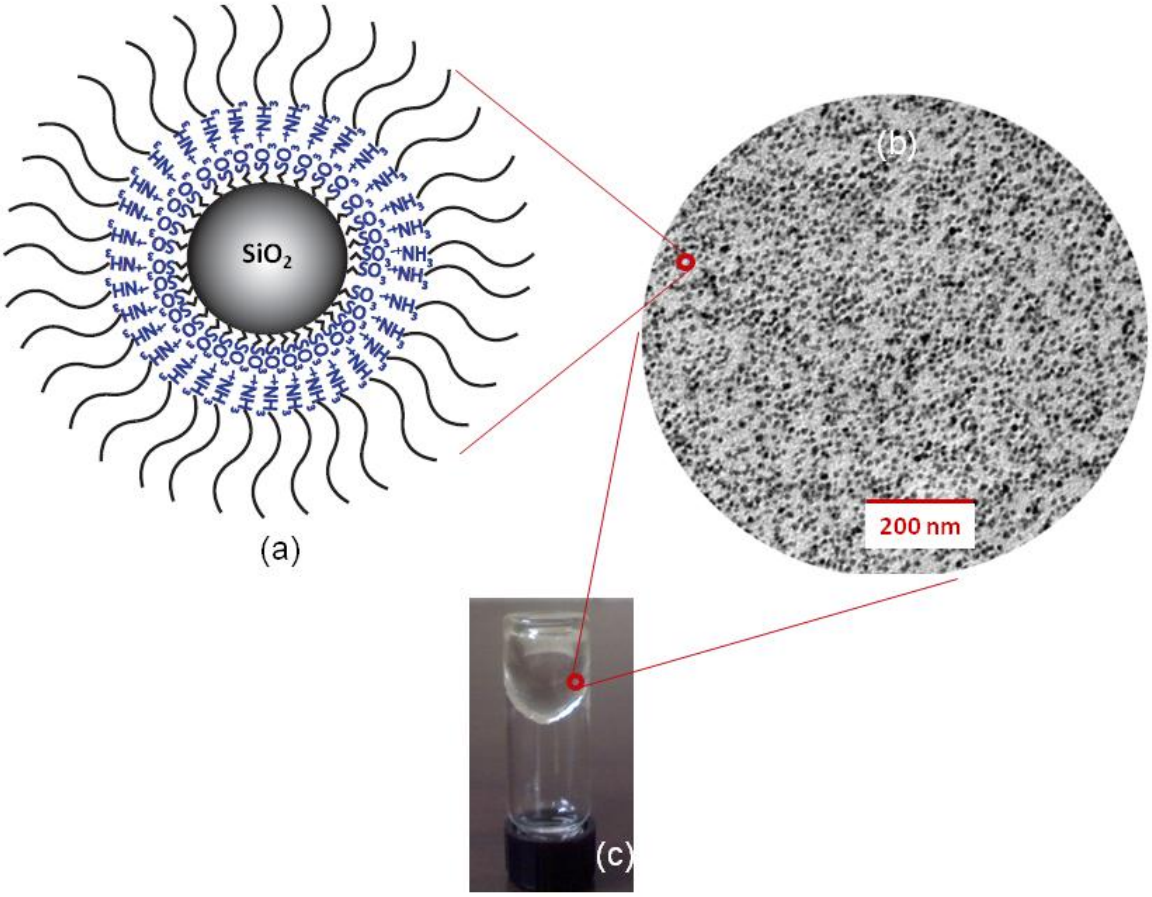

Figure 2.1 Building blocks for NIMs: **(a)** PEG chain tethered to silica nanoparticle by ionic linkage between sulfonic acid and amine groups. **(b)** TEM micrograph of NIMs illustrating that the nanoparticles are well dispersed. **(c)** Upturned vial showing NIMs flow as neat, homogeneous liquids.

Figure 2.1 (a) illustrates the building blocks for the nanoscale ionic materials used in this study. A silica nanoparticle core is densely functionalized (1-2 molecules/nm^2) with an ionic species. The counterions charge is balanced by neutralization with nearly monodisperse polyethylene glycol (PEG) (see Supporting Information). Figure 2.1 (b) is a transmission electron micrograph (TEM) of the NIMs material; it indicates that the material is comprised of well-dispersed spherical nanoparticles of size ≈ 10 nm, with no evidence of aggregation. Both features have been confirmed using photon correlation spectroscopy and small-angle x-ray scattering (SAXS).

The grafting density and molecular weight of the PEG corona can be varied to produce a spectrum of liquids of controlled viscosity. On one end of the spectrum are systems comprised of relatively long telomers with grafting densities $\sigma \approx$ (1-2) chains/nm^2, which have consistencies similar to simple liquids (Figure 2.1(c)). At the opposite extreme, are particle-rich NIMs, comprised of more densely grafted $\sigma \approx 2$ chains/nm^2, but shorter telomers, which have the appearance of soft waxes.

Steady-shear viscosity data for NIMs liquids at both ends of the spectrum reveal Newtonian fluid behavior at low shear rates (lowest shear rate probed ~10^{-8} sec^{-1}), and shear-thinning characteristics at high rates (Figure 2.2). These features are readily observed in polymeric liquids, but the Newtonian flow regime is generally not seen in nanoparticle suspensions. This follows from the tendency of particles with high surface area/volume ratios to exert strong short-range attractive forces in suspension, leading to aggregated structures, which can percolate up to macroscopic length scales. The presence of a Newtonian regime in our self-suspended nanoparticle suspensions indicates that these liquids are able to reach an equilibrium state, which allows the effect of the particle core on the suspension viscosity to be systematically studied.

Table 2.1 Molecular and surface characteristics of NIMs samples used in the study

Weight %	Chain M_w	PDI	σ chains/nm^2	ξ (nm)
29.7	2000	1.05	2.1	0.70
23.5	5000	1.08	1.1	0.94
18.7	5000	1.08	1.5	0.81
13.4	5000	1.08	2.2	0.67
9.5	9000	1.06	1.9	0.73
8.5	14000	1.10	1.3	0.86
4.5	19000	1.08	2.0	0.72

PDI is the polydispersity index of the polymer.

σ is the grating density of polymer chains on the nanoparticle surface.

ξ is the spacing between the polymer chains.

Figure 2.3 shows the relative shear viscosity, $\eta_r \equiv \mu_0 / \mu_c$ deduced from the steady-shear data for fluids with similar corona grafting density, but widely varying molecular weight, as well as for fluids with fixed corona molecular weight, but variable graft density. Both effects are captured by plotting η_r versus the core-particle volume fraction ϕ, bottom horizontal axis, and η_r versus reduced corona molecular weight, , $\widehat{M} = \varphi Mw$, top horizontal axis. Here μ_0 and μ_c are, respectively, the Newtonian viscosity of the NIMs liquid and the unattached telomeric corona.

The dashed line in the figure is the relative viscosity predictions based on Batchelor's analyses for suspensions [21]. It is clear from the figure, that but for the lowest core particle volume fractions, the relative viscosity of NIMs suspensions are dramatically higher than those predicted using the Batchelor model. The high η_r values are consistent with published results for soft glassy liquids and jammed colloidal suspensions [22], but, notably are observed here at core volume fractions well below those required for random close-packing of the spherical nanoparticles, $\phi_c \approx 0.64$ [23].

There are two physical frameworks that can be used for understanding viscous properties of a self-suspended suspension. (i) If the particles are sparsely grafted and the random-coil dimension R_g of the telomeric corona is large in comparison to the average particle diameter $\bar{d}$, the cores can be imagined to act as anchor/branch points for the corona. In this case, behavior consistent with star branched polymers is expected [24, 25].

(ii) If $\bar{d}$ is comparable to, or larger than, the thickness/brush height [26], H, of the corona, a model based on particles that each carry around a portion of the suspending medium is required. In this case, two limiting situations should exist: (a) The random-walk step length b_K of corona chains is much smaller than the telomer spacing $\xi \approx \sigma^{-1/2}$ and substantially smaller than

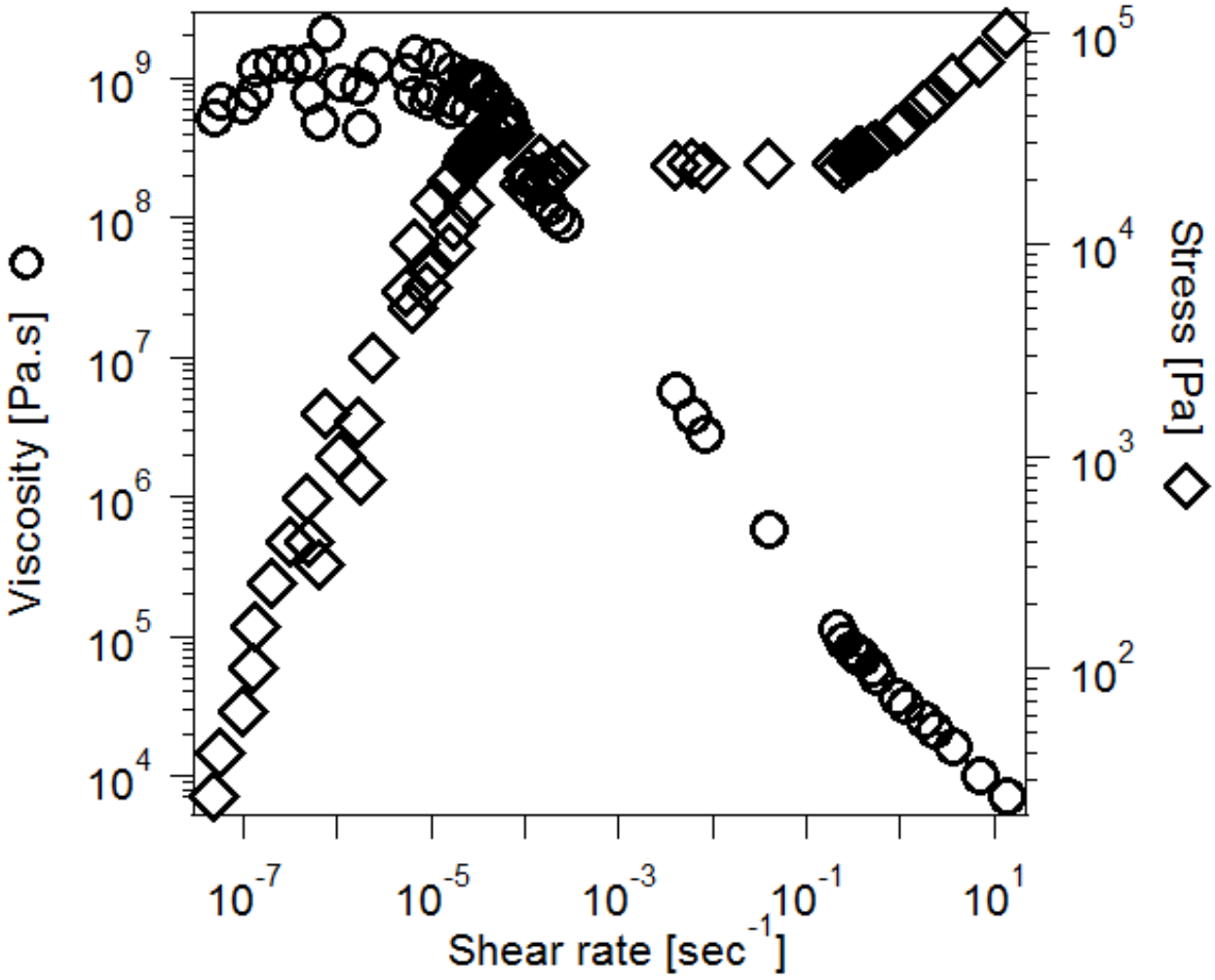

Figure 2.2 Shear rate dependence of the viscosity indicating the presence of a Newtonian regime at low shear rates for the system with φ = 12.2 %.

$$\widehat{M} = \varphi Mw$$

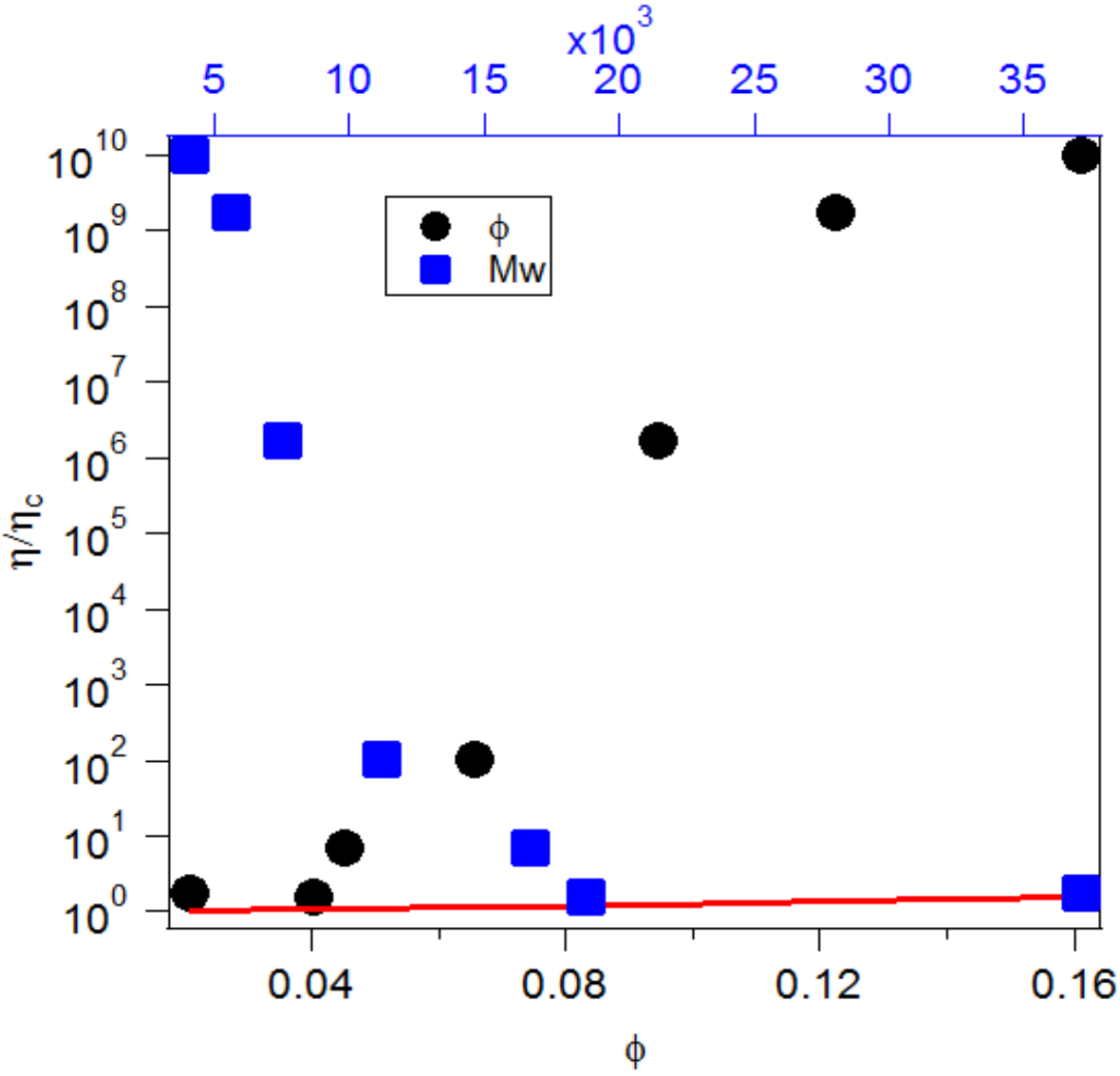

Figure 2.3 Relative viscosity of self-suspended suspensions: Relative viscosity, η_r, at 70 °C vs. volume fraction, φ, of the core particles (circles, bottom axis), and reduced molecular weight of the attached corona (squares, top axis). Line corresponds, to $\eta_r(\phi)$ predictions from Batchelor's theory.

the brush height (i.e. $b_K << H$). In this case, motion of the outermost sections of the corona is to a first approximation uncorrelated with those of the cores. The tethered corona therefore acts as a conventional solvent and the suspension viscosity should vary with the core particle volume fraction in a qualitatively similar manner to a conventional particle suspension.

(b) The spacing of corona chains is small (i.e. $\xi \leq b_K$). In this case, they will exhibit rod-like conformations and will stretch away from the particle surface to fill the intervening space between the nanocores. The suspending medium and particle motions are therefore coupled, and the suspension should exhibit properties analogous to soft glasses [27-30].

Comparing expectations from these models with the results in figure 2.3, it is evident that a suspension model provides a better representation of the viscous behavior of NIMs. Additionally, the random-walk step length for PEG is readily estimated as $b_K = 1.1\,\text{nm}$, which is larger than the average spacing, $\xi \approx$ 0.7-1 nm (Table 2.1) of corona chains near the SiO_2-PEG interface. Model (ii)-(b) therefore appears to provide the most plausible framework for understanding viscous properties, particularly the divergence of η_r at modest ϕ.

Figure 2.4 shows that these suspensions are in fact soft glasses. Specifically, the figure reports strain-dependent dynamic moduli of NIMs liquids measured in an oscillatory shear flow of fixed frequency (ω = 10 rad/s), but variable strain amplitude γ. The inset shows typical strain-dependent elastic/storage modulus $G'(\gamma)$, viscous/loss modulus $G''(\gamma)$, and shear stress $\tau(\gamma)$data. The decrease in $G'(\gamma)$ and the concomitant appearance of a maximum in $G''(\gamma)$ are both robust features of "soft glassy" materials [27-30]. Soft glassy materials have been modeled as mechanical elements trapped in tight cages (see Figure 2.4) formed by repulsive interactions with their nearest neighbors. In this model, glassy dynamics arise because the energy required to

escape the cage is comparable to the depth of the inter-particle potential well, which can be substantially larger than thermal energy.

The height of the loss maximum therefore reflects the amount of mechanical energy dissipated when cages break apart (right cartoon in Figure 2.4). The critical shear strain at which the maximum is observed coincides with a noticeable change of slope in $\tau(\gamma)$ and is therefore designated the yield strain γ_y, at the measurement conditions. It is evident from Figure 2.5 that whereas the loss maximum grows as temperature is increased, γ_y is essentially independent of temperature. Neither feature is captured in the soft glassy rheology (SGR) model [29, 30]. A more prominent loss peak is nonetheless consistent with greater levels of interpenetration (crowding) of corona chains at higher temperatures. This is confirmed by the appearance of secondary loss maxima at lower strains, presumably arising from higher order correlations in the cage constraint.

The main findings of this communication are summarized in Figure 2.6. This figure is a so-called master curve obtained by horizontally shifting the frequency-dependent storage and loss moduli data (Appendix), recorded at various discrete shear strains, above the yield strain, and over a finite range of oscillation frequencies (0.1 rad/s < ω < 5 rad/s). This shifting procedure evidently produces a continuous map of the materials dynamic response over a substantially extended range of time.

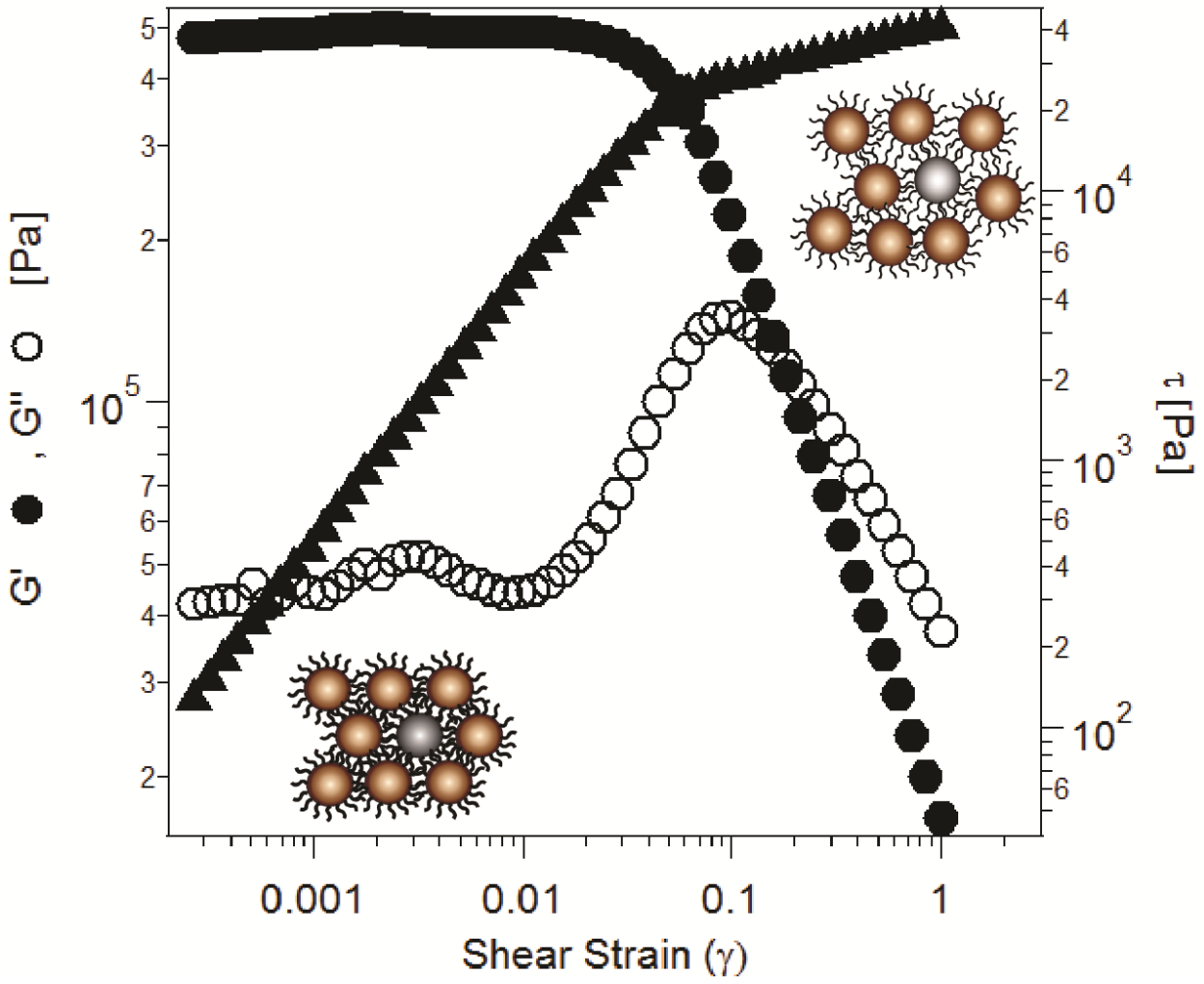

Figure 2.4 *G'(γ)* (filled circles), *G"(γ)* (open diamonds), and $\tau(\gamma)$ (filled triangles, right axis) at 90 °C. The cartoon graphics are representations of the cage-like environment before yield (lower left), and after yield (upper right).

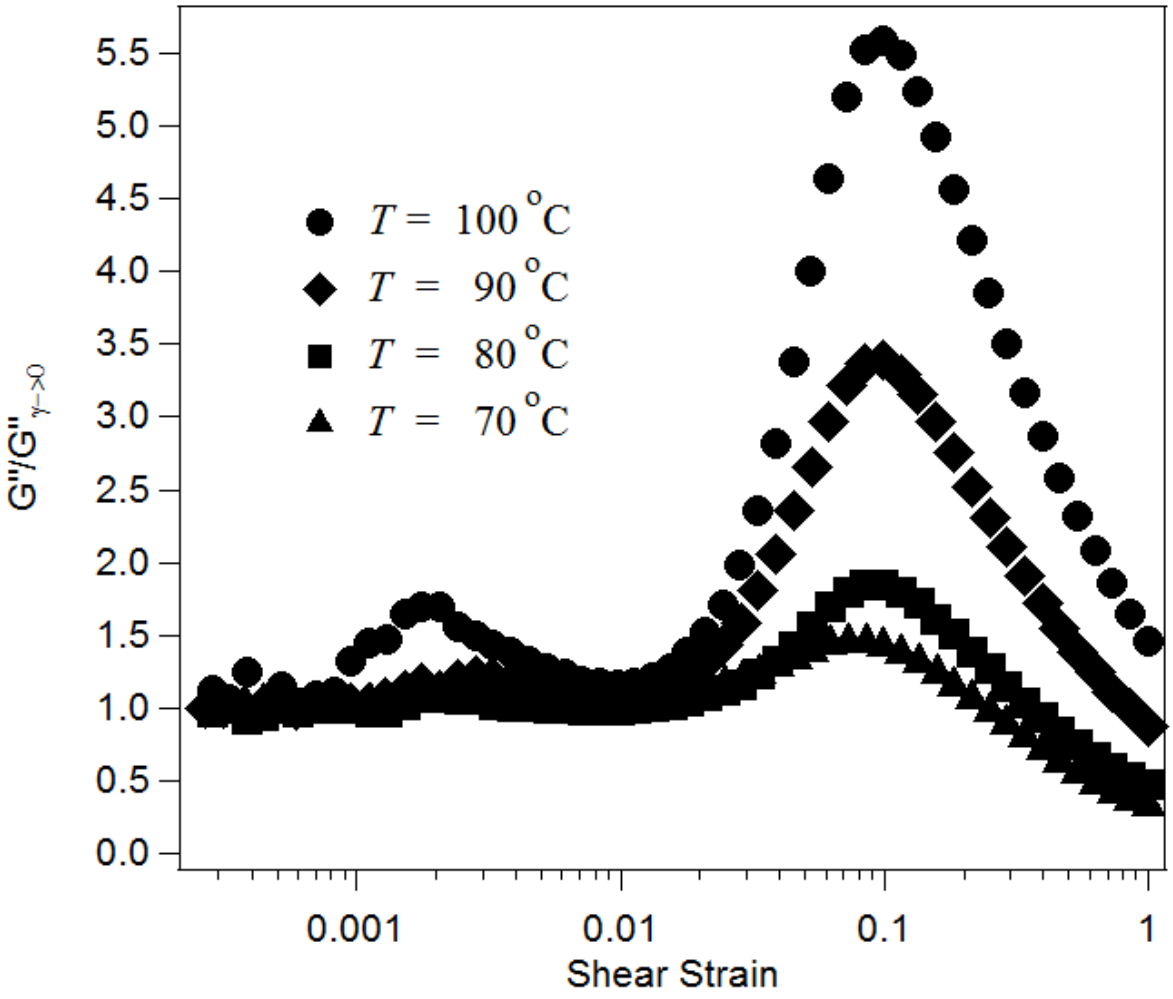

Figure 2.5 Loss modulus *G"* divided by its linear response value in the limit of zero shear strain, γ, for a NIMs material with ϕ = 12.2 %. The data are presented at various temperatures at frequency of 10 rad/sec.

Termed time-strain superposition (TSS), it is analogous to the more widely studied time-temperature superposition (TTS) methodology [31, 32] wherein the dynamic range over which a materials behavior is monitored is substantially increased by horizontal (and vertical) shifting of measurements performed at multiple temperatures.

Figure 2.6 and 2.7 show the master curve obtained by TSS for two typical NIMs materials. The reference data used in both cases are the dynamic moduli at the yield strain. It is apparent that the dynamic range over which the materials response can be characterized using this approach is well beyond that accessed by normal lab experiments. In particular, the longest time-scale probed at the low frequency end of Fig. 4 is 10^{18} seconds.

The shift factors a_γ required to create the TSS master curves are plotted in the inset. Surprisingly, for all NIMs systems studied, $a_\gamma(\gamma)$ manifests a single universal form:

$$\log a_\gamma(\gamma) = \frac{-A_1(\gamma - \gamma_{ref})}{A_2 + \gamma - \gamma_{ref}} \qquad (2.1)$$

which is strikingly similar to the empirical William-Landel-Ferry (WLF) equation (lines) widely used for calculating temperature-dependent shift factors,

$$\log a_T(T) = \frac{-C_1(T - T_{ref})}{C_2 + T - T_{ref}} \qquad (2.2)$$

for time temperature superposition in polymers above their glass transition [32]. Here γ_{ref} is the reference shear strain used for TSS; T_{ref} is the reference temperature for TTS, and the constants A_1, A_2, C_1 and C_2 are determined from fitting the respective expressions to the experimentally determined shift factors. Figure 2.8 shows that the experimental shift factors are in uniformly good agreement with the analog of the WLF model over more than eighteen decades.

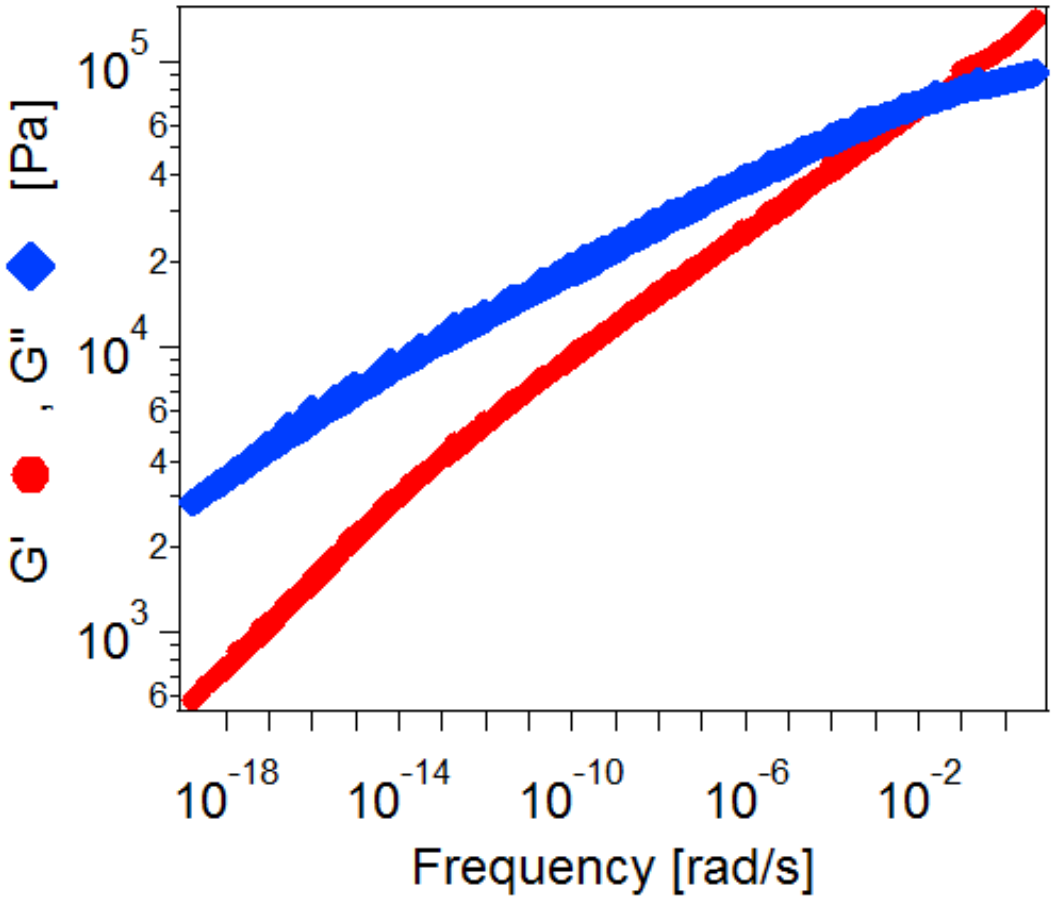

Figure 2.6 Master curve obtained at 70 °C using TSS for NIMs with φ = 12.2 % and corona M_w = 5000.

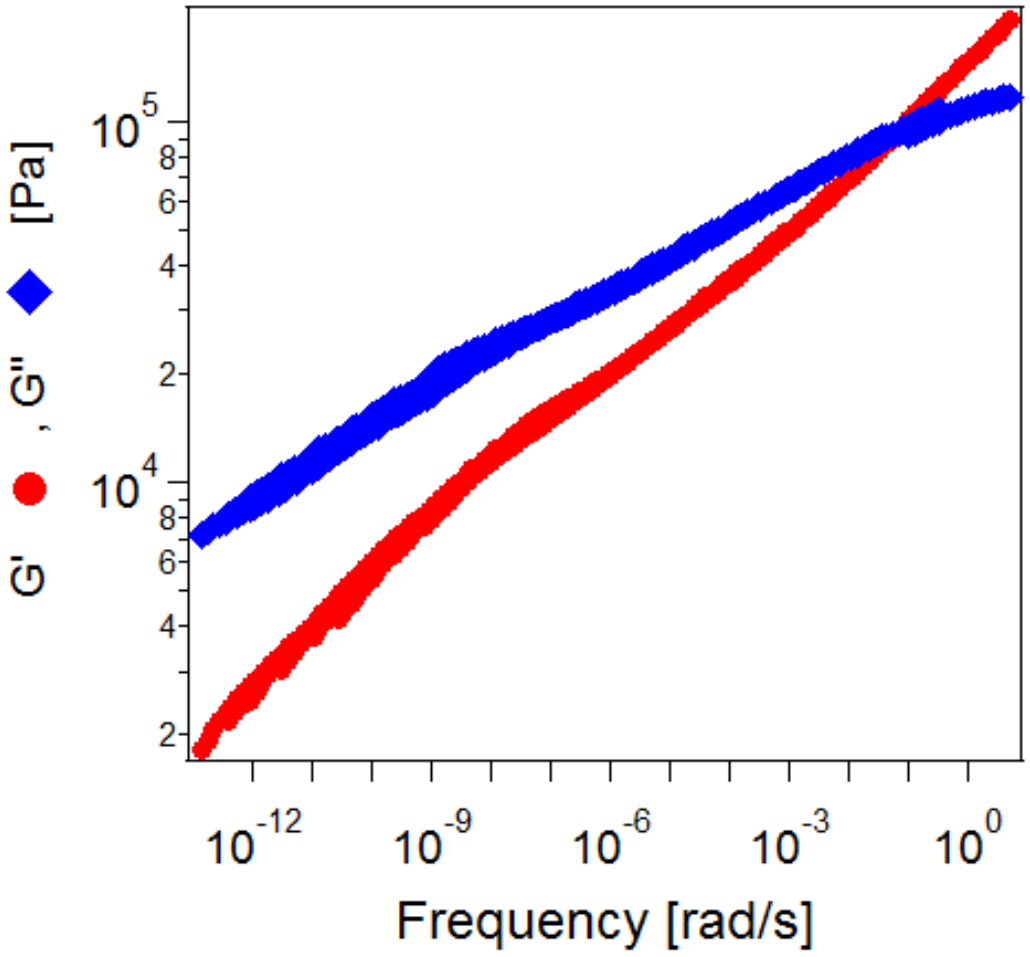

Figure 2.7 Master curve obtained at 70 °C using TSS for NIMs with φ = 16.1 % and corona M_w = 2000.

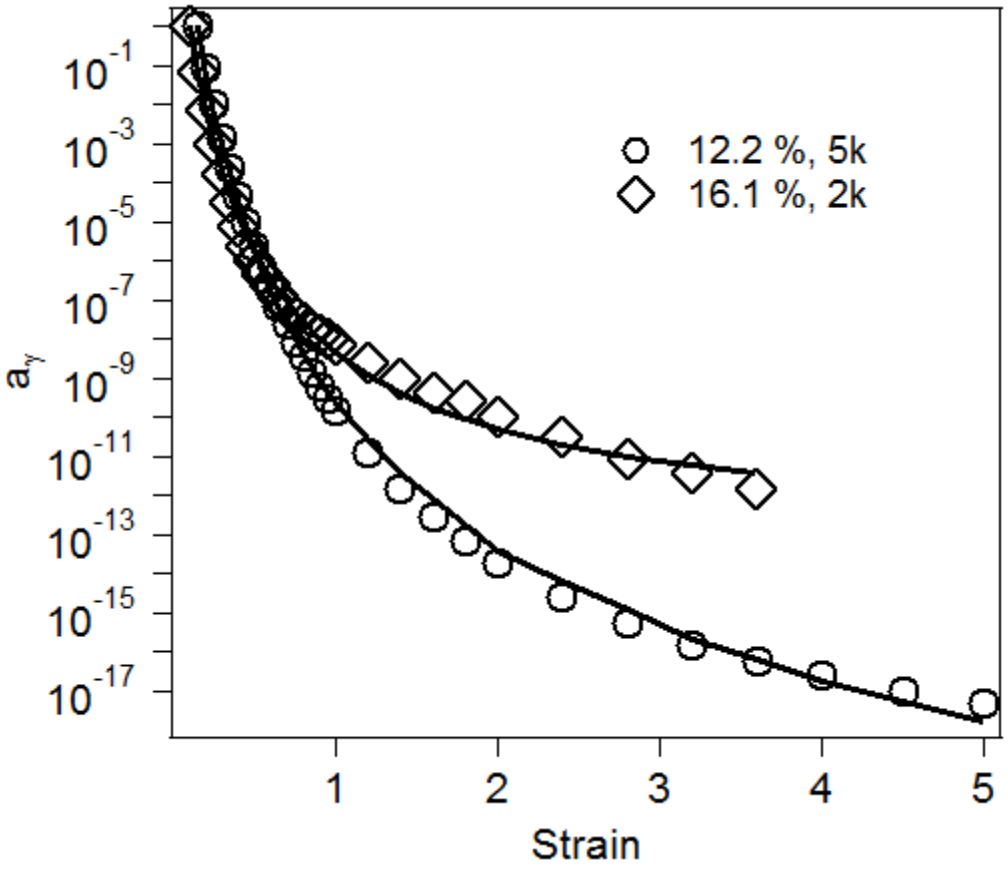

Figure 2.8 The corresponding strain-dependent shift factors, a_γ vs. shear strain (markers) required for TSS. The solid lines are the corresponding $a_\gamma(\gamma)$ obtained using the analog to the WLF formula discussed in the text. Parameters: A_1 = 13.1 and A_2 = 51.3 (φ = 12.2 %.; circles); A_1 = 20.6 and A_2 = 93.2 (φ = 16.1 %.; diamonds).

Although our focus in this study is on shear strains above the yield point, a similar TSS principle has been observed for strains below γ_y. In this latter regime, $a_\gamma(\gamma)$ also manifests a universal dependence,

$$a_\gamma \approx \exp[-A\gamma^2]$$

where *A* is a fit parameter, which can be determined from the slope of *G'(γ)* in the low strain (linear viscoelastic) shear regime. This finding is in essentially quantitative accord with the expectations based on Sollich's SGR model [29, 30], we have discussed these results in the appendix. Taken together, the simplicity of the $a_\gamma(\gamma)$ forms in both regimes, belie the extraordinary slow motions that are made accessible by the TSS procedure. They also raise obvious questions about the equivalence of strain and temperature in other jammed systems.

2.4 Conclusions

In closing, we point out that both the TSS principle and the spectacularly slow motions it unveils are not limited to the nanoscale ionic liquids in which the TSS transformation was first discovered. Experiments using self-suspended nanoparticle liquids created by: (a) covalent attachment of PEG telomers to various inorganic nanostructures; and (b) by suspending the densely tethered, hairy nanostructures used in (a) in PEG liquids, show similar behavior; with $a_\gamma(\gamma)$ taking the same universal forms at strains above and below the yield point of the materials. We anticipate that application of TSS to other jammed liquids [33, 34], (e.g. micellar suspensions, ionomer gels, pastes, waxes and living cell), will reveal similar behaviors as reported here for NIMs. Theoretical work is underway to understand the physics underpinning

TSS above the yield point and to uncover the fundamental processes that produce the slow motions reported here for self-suspended nanoparticle liquids.

ACKNOWLEDGEMENTS

We gratefully acknowledge KAUST-CU center for energy and sustainability and the Cornell Center for Materials Research (CCMR) for financial support.

REFERENCES

1. A. Einstein Annln. Phys. **19**, 289 (1906).
2. A. Einstein Annln. Phys. **17**, 549 (1905).
3. S. A. Rogers, D. Vlassopoulos, P. T. Callaghan Phys. Rev. Lett. **100**, 128304 (2008); R. Sigel, S. Pispas, D. Vlassopoulos et al. Phys. Rev. Lett. **1999**, 83, 4666.
4. M. Cloitre, R. Borrega, F. Monti, L. Liebler, Phys. Rev. Lett. **90,** 068303 (2003).
5. M. Cloitre, R. Borrega, L. Liebler, Phys. Rev. Lett. **85**, 4819 (2000).
6. W. van Megan, S. M. Underwood, Nature **362**, 616 (1993).
7. A. B. Bourlinos, et al. Adv. Mater. **17**, 234 (2005).
8. S. C. Warren et al. J. Am. Chem. Soc. **128**, 12074 (2006).
9. R. Rodriguez, R. A. Herrera, L. A. Archer, E. P. Giannelis, Adv. Mater. **20**, 4353 (2008).
10. T. V. Wenre, T. E. Patten, J. Am. Chem. Soc. **121**, 7409 (1999).
11. S. Nu et al., Angew. Chem. Int. Ed. **40**, 4016 (2001).
12. A. Tuteja, M. E. Macay, S. Narayanan, S. Ashokan, M. S. Wong, Nano Lett. **7**, 1276 (2007).
13. M. E. Macay et al., Science **311**, 1740 (2006).
14. N. Dutta, D. Green, Langmuir **24**, 5260 (2008).
15. H. Oh, P. F. Green, Nature Mater. **8**, 139 (2009).
16. A. Bansal et al., Nature Mater. **4**, 693 (2005).
17. M. J. Kropka, V. G. Sakai, P. F. Green, Nano Lett. **8**, 1061 (2008).
18. V. Goel et al., J. Polym. Sci. Part B: Polym Phys. **44**, 2014 (2006).
19. P. Akcora et al., Nature Mater. **8**, 354 (2009).
20. S. C. Warren et al., Science **320**, 1748 (2008).
21. G. K. Batchelor, J. Fluid Mech. **83**, 97 (1977).

22. R. G. Larson, The Structure and Rheology of Complex Fluids (Oxford Univ. Press, 1998).

23. C. Song, P. Wang, H. Maske, Nature **453**, 629 (2008).

24. H. Watanbe et al., Macromolecules **38**, 7404 (2005).

25. M. E. Hegelson, N. J. Wagner, D. Vlassopoulos, J. Rheology **51**, 273 (2007); D. Vlassopoulos, J. Polym. Sci. Part B: Polym. Phys. **42**, 2931 (2004).

26. S. T. Milner, Science **251**, 905 (1991).

27. T. G. Mason, D. A. Weitz, Phys. Rev. Lett. **75**, 2770 (1995).

28. H. M. Wyss. et al., Phys. Rev. Lett. **98**, 238303 (2007).

29. P. Sollich, F. Lequeux, P. Hebraud, M. E. Cates, Phys. Rev. Lett. **78**, 2020 (1997).

30. P. Sollich, Phys. Rev. E **58**, 738 (1998).

31. P. A. O'Connell, G. B. Mckenna, Mech. Time Dep. materials **6**, 207 (2002); G. B. McKenna and P. A. O'Connell, Poly. Engng. and Sci. **37**, 1485 (1997).

32. J. D. Ferry, Viscoelastic Properties of Polymers (Wiley, New York, 1980).

33. P. G. Debenedetti, F. H. Stillinger, Nature **410**, 259 (2001).

34. A. Trepat et al. Nature **447**, 592 (2007).

APPENDIX: Supplementary information for chapter 2

Synthesis: Ludox Silica (Sigma Aldrich) was functionalized with sulfonic acid using 3-(trihydroxysilyl)-1-propanesulfonic acid (Gelest). To ensure dense surface coverage, the silane was added drop wise, in a large excess at pH 2. These conditions favor the anchoring reaction. The excess (un-tethered) silane was removed after completion of the reaction using dialysis (Snake skin Dialysis tubings, Pierce Scientific) against deionized water [9]. The functionality of the resultant sulfonic acid-derivatized SiO_2 nanoparticles was determined by titrating against a standard solution of NaOH. Nearly monodisperse Amine terminated PEG (Polymer source, Canada) was added stoichiometrically according to the functionality calculated using titration, and the linking reaction was allowed to proceed to completion over several days. Water was removed by evaporation in a convection oven and the product was dried extensively under vacuum and stored in the dried form at room temperature. The efficiency of the sulfonic acid/amine linking reaction was evaluated by dissolving the dried samples in chloroform and dialyzing them against pure chloroform for extended periods of time. Thermal gravimetric analysis (TGA) results in Fig. S1 reveal no change in the polymer weight fraction even after two days of dialysis, confirming that the linking reaction goes to completion under the synthesis conditions.

Rheology: Rheological measurements were performed using controlled strain (Rheometric Scientific/TA, ARES) and stress controlled (Paar Physica, MCR 301) rheometers outfitted with cone and plate fixtures. Prior to each experiment, the history of sample loading was removed by continuously shearing the materials at large strains, i.e. well above the yield strain.

TEM images were obtained at 120 kV with TEI Technie T12 TEM/STEM by dissolving the sample in water, coating a few drops of the resultant suspension on a copper grid, and subsequently evaporating the solvent.

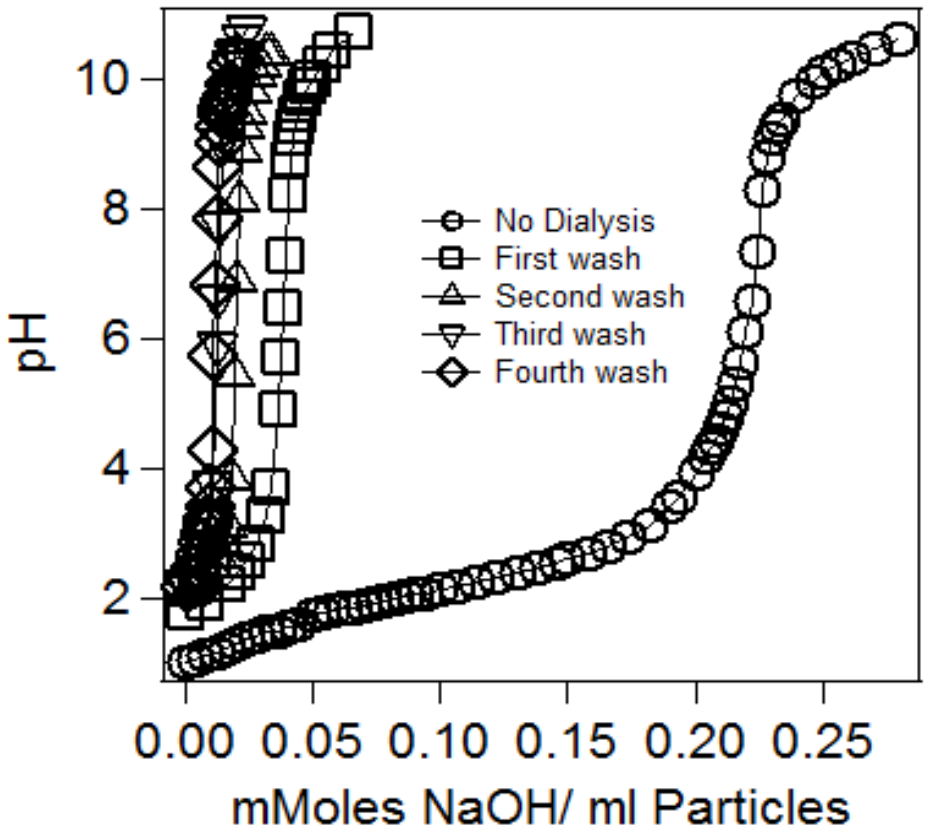

Supplementary figure 2.1 pH titration curves after different steps of the dialysis procedure employed to remove the free silane from the functionalized silica nanoparticles.

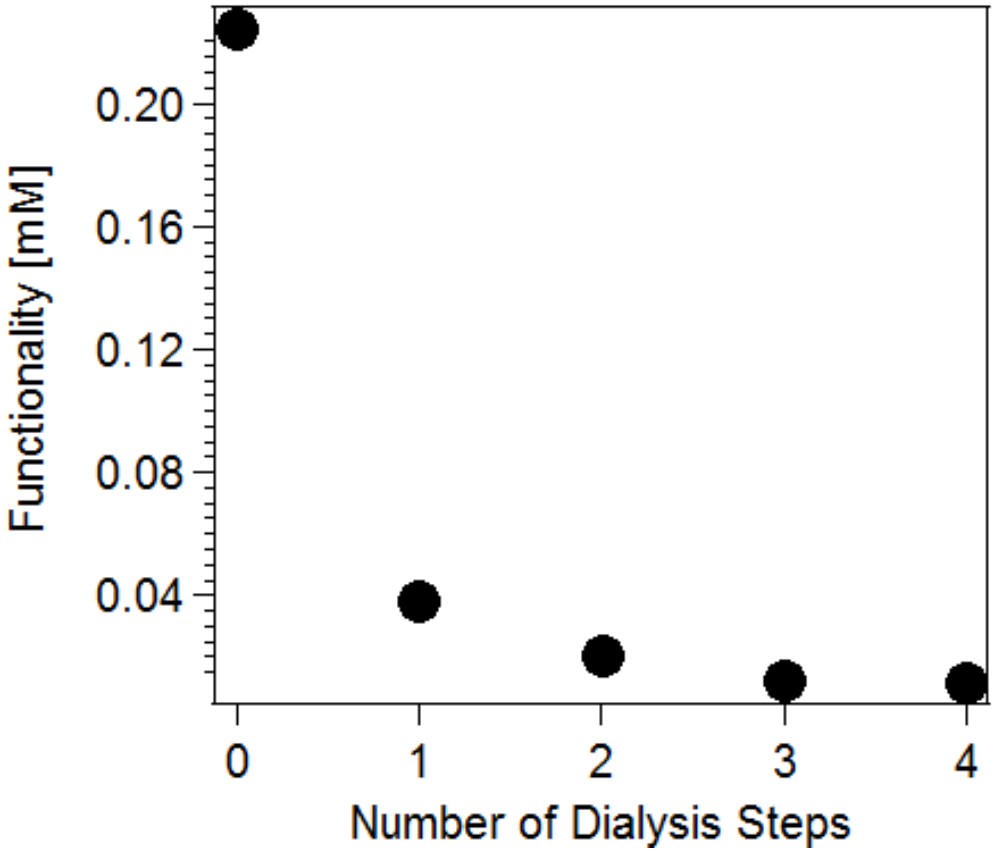

Supplementary figure 2.2 Functionality of sulfonic acid functionalized particles as a function of the number of dialysis cycles. The functionality reaches a plateau value after 3 washes, confirming the removal of all the excess silane.

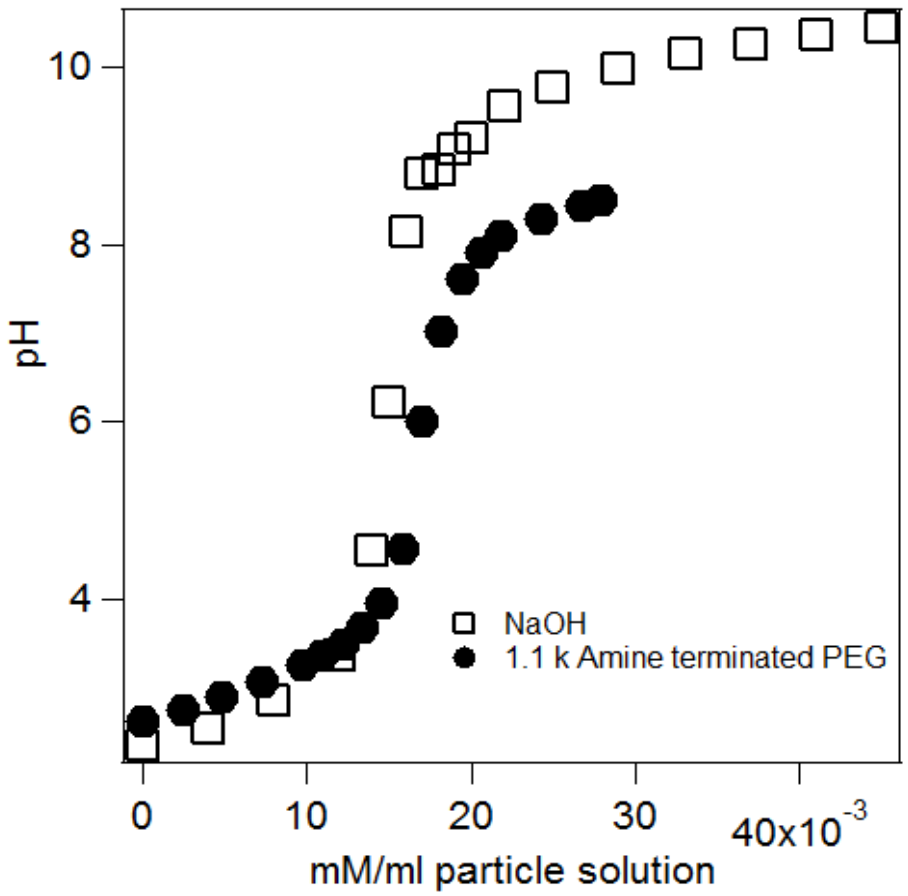

Supplementary figure 2.3 Functionality of the particles was confirmed by titration with multiple bases. Plot shows that similar values for the functionality were obtained by titration with NaOH and amine terminated polyethylene glycol (PEG).

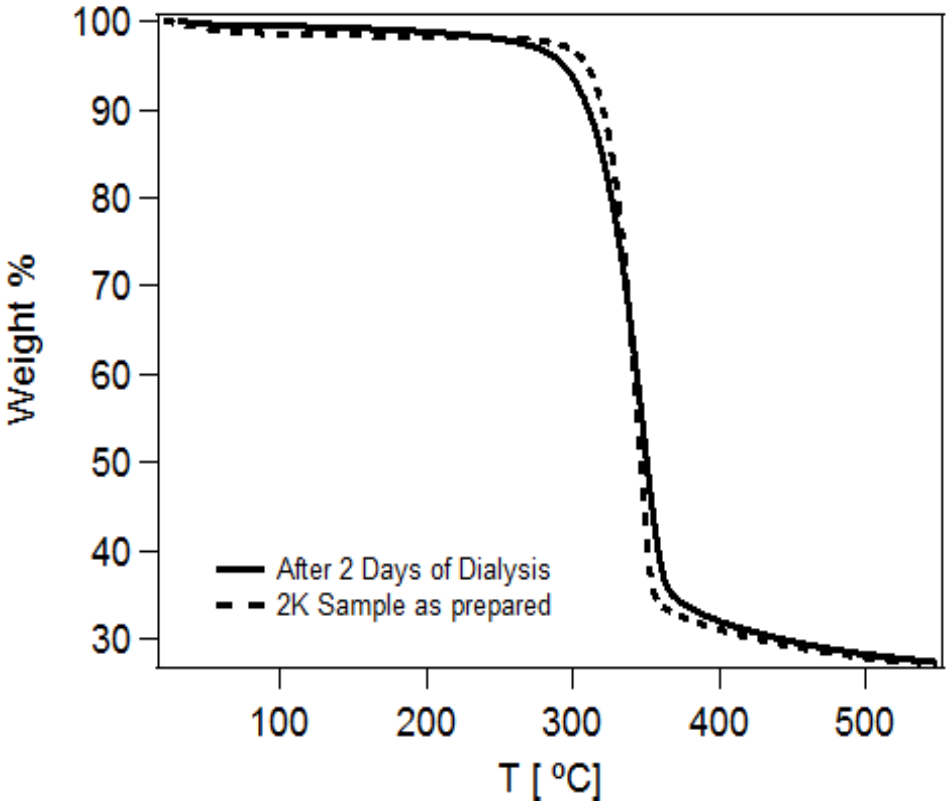

Supplementary figure 2.4 TGA characterization of PEG (2k)-SiO_2 NIMs material before and after dialysis in chloroform for 2 days. Dialysis was performed using a membrane with a 10,000 g/mol molecular weight cut-off. It can be seen that there is no significant loss of the polymer from the sample during dialysis.

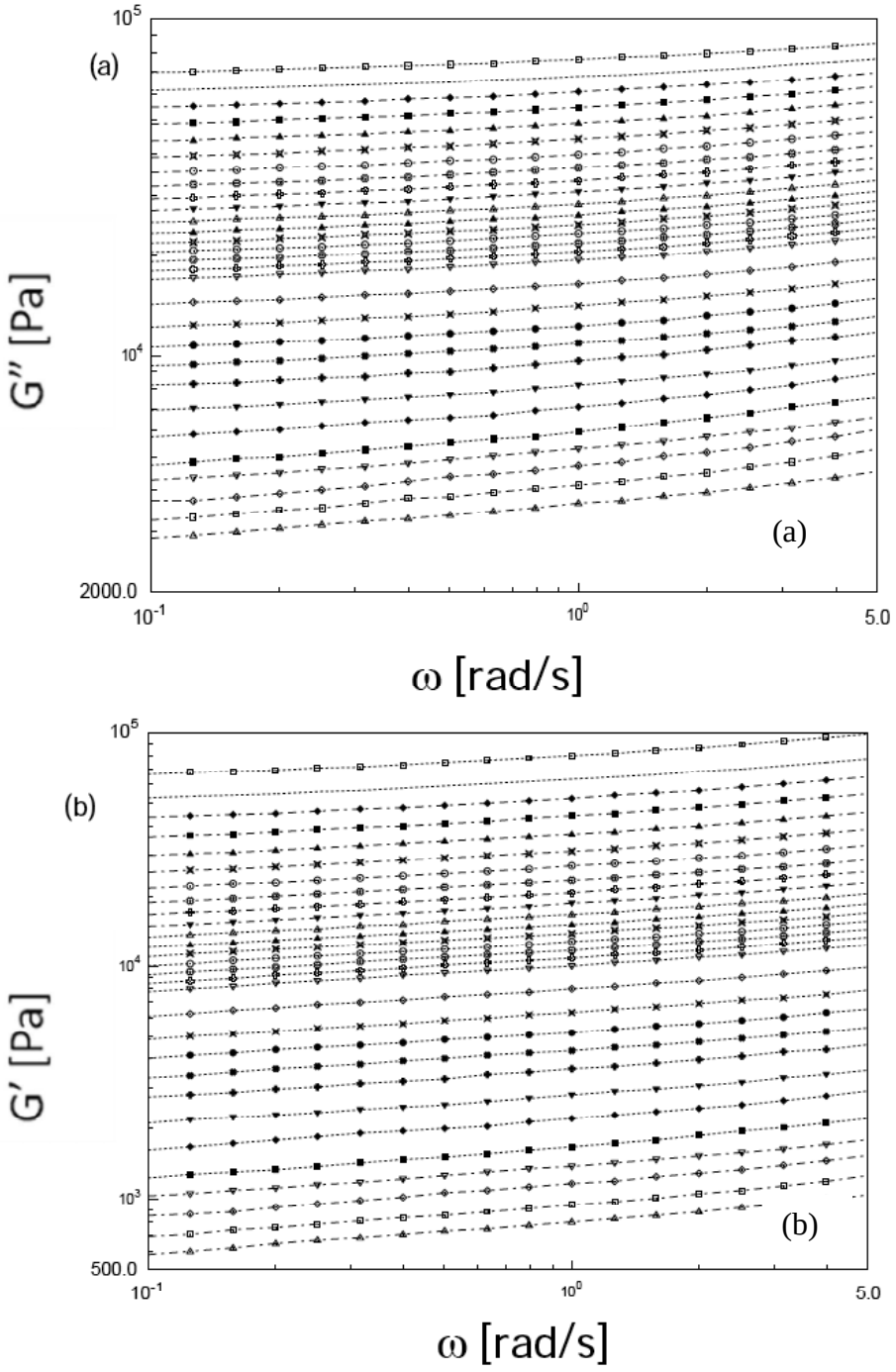

Supplementary figure 2.5 (a) Loss modulus *G''* and **(b)** storage modulus *G'* vs. frequency ($0.1\ s^{-1} < \omega < 5s^{-1}$) for NIMs with $\varphi = 12.2$ % at various discrete values of shear strain. Strain values are. from top to bottom: 0.15, .20, .25, .30, .35, .40, .45, .50, .55, .60, .65, .70, .75, .80, .85, .9, .95, 1, 1.2, 1.4, 1.6, 1.8, 2, 2.4, 2.8, 3.2, 3.6, 4, 4.5 and 5. All measurements were performed at a temperature of 70 °C.

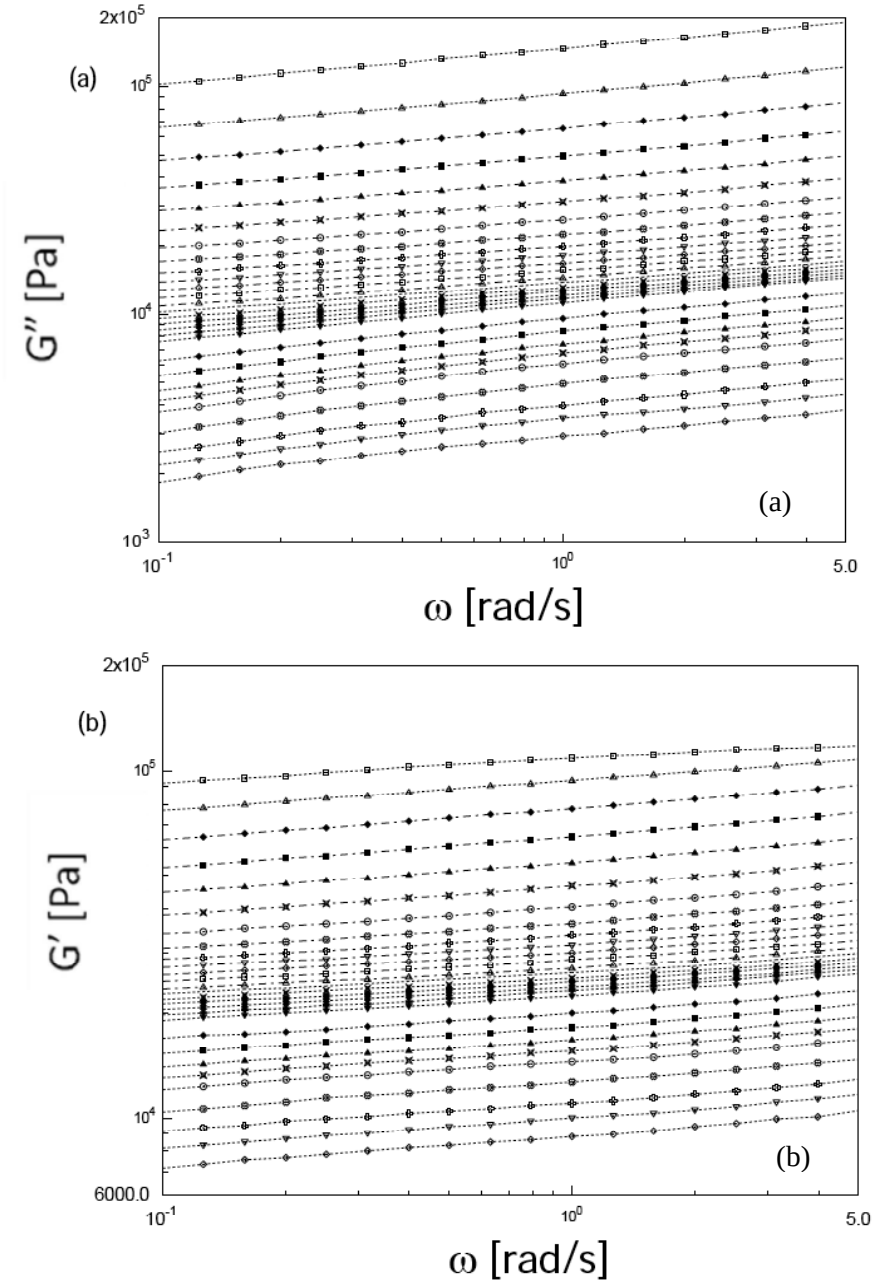

Supplementary figure 2.6 (a) Loss modulus *G''* and **(b)** storage modulus *G'* vs. frequency ($0.1\ s^{-1} < \omega < 5\ s^{-1}$) for NIMs with φ = 16.1 % at various discrete values of shear strain. Strain values are, from top to bottom: 0.10, .15, .20, .25, .30, .35, .40, .45, .50, .55, .60, .65, .70, .75, .80, .85, .9, .95, 1, 1.2, 1.4, 1.6, 1.8, 2, 2.4, 2.8, 3.2, 3.6 respectively from top to bottom. Measurements were taken at a temperature of 70 °C.

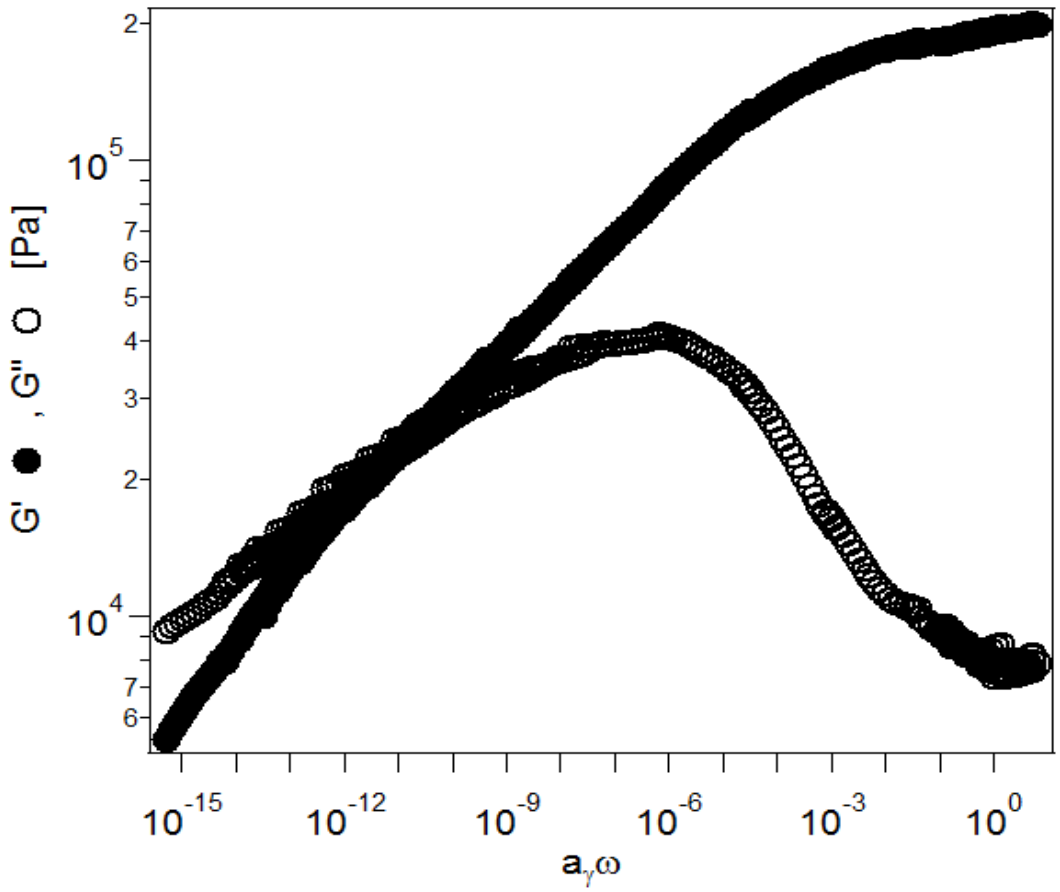

Supplementary figure 2.7 Master curve obtained from the TSS procedure by taking the dynamic moduli in the linear viscoelastic regime as the reference. Core volume fraction, φ = 12 % and corona molecular weight, M_w = 9000 for this sample.

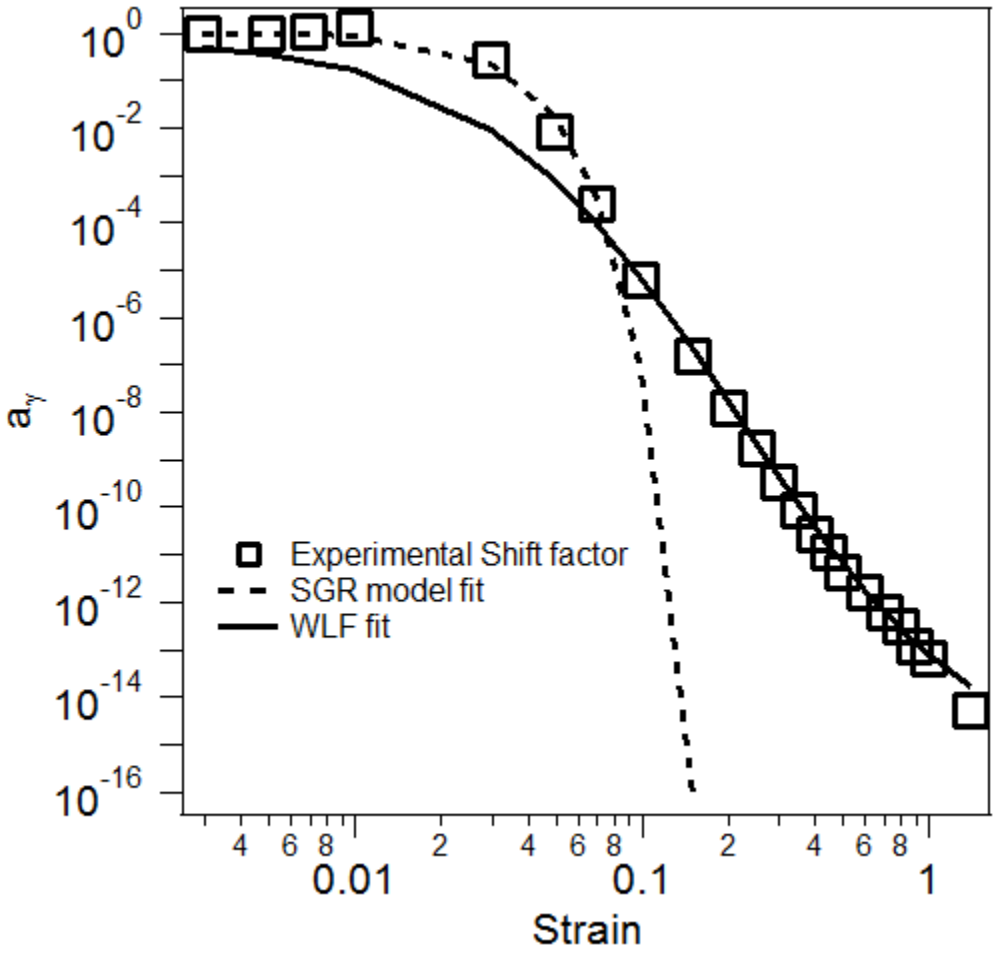

Supplementary figure 2.8 Shift factors used to obtain the master curve shown in supplementary figure 2.7. Data points show the experimental shift factors. Solid line is fit from the WLF equation described in the main text. Dashed line is fit from the SGR expression $a_\gamma = exp(-A\gamma^2)$.

In the studies following this one, we have followed a more rigorous procedure for purifying NIMs, wherein the sample is first dissolved in a good solvent and centrifuged with the help of a non-solvent. Good solvent used for PEG samples was chloroform and the non-solvent used was hexane. Centrifugation procedure was repeated multiple times and the effectiveness of the purification procedure was assessed by performing TGA after each centrifugation step. From the similar experiment performed on a physical blend of PEG and silica nanoparticles, it was observed that this procedure is effective in removing the untethered polymer chains from the tethered polymer chains.

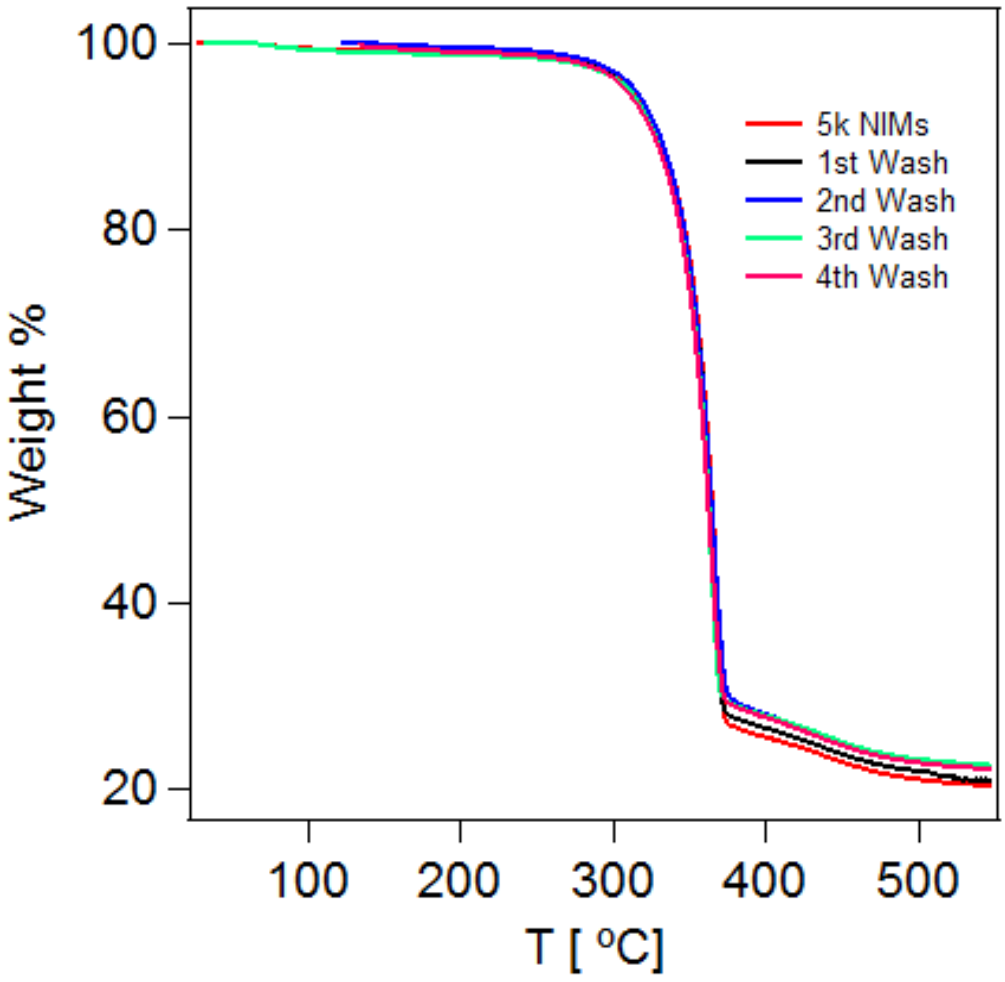

Supplementary figure 2.9 TGA traces showing the organic content of sample during multiple purification cycles. Purification procedure results in decrease of the organic content, indicating the removal of untethered polymer chains. After a few steps, the organic content is not decreasing any further, implying that most of the untethered polymer has been removed from the sample.

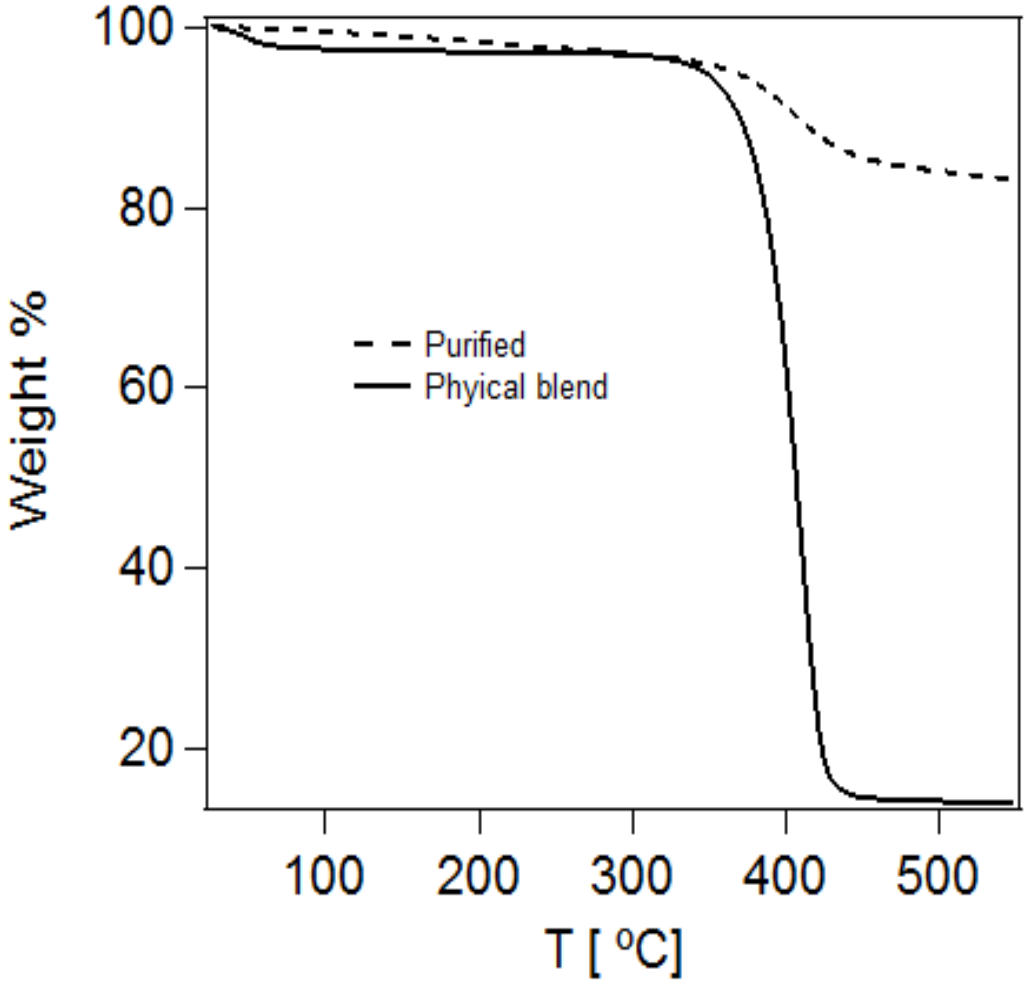

Supplementary figure 2.10 TGA trace showing the results of purification of a physical blend of PEG and silica nanoparticles with the same method employed for NIMs samples. Contrary to the results for NIMs shown in supplementary figure 2.9, purification procedure for the physical blend results in a significant weight loss of the sample, proving the effectiveness of this procedure.

CHAPTER 3

Entangled Polymer Dynamics in Nanoparticle Grafted Oligomers

3.1 Abstract

Entanglement effects give rise to very sluggish dynamics of a polymer chain, producing very high viscosity and relaxation time. Till now, entanglement effects have been realized only for very high molecular weight polymers. Herein we show that small molecular weight polymers tethered the nanoparticle surface exhibit dynamical features similar to highly entangled polymers. Our findings open up an alternative pathway to engender entanglement effects in short linear chains by topologically confining them through densely grafting to a surface.

3.2 Introduction

Physical properties of high molecular weight polymers differ significantly from their low molecular weight counterparts and this feature is commonly understood to arise from the entanglement effects in high molecular weight polymers [1]. Entanglements are topological constraints arising from the neighboring chain segments that affect the large scale motion in high molecular weight polymers [2-5]. de Gennes proposed the idea of reptation in entangled polymers, wherein the lateral motion a polymer chain is highly restricted, forcing the polymer chain to reptate in a snake-like manner along its contour inside a confining tube [6].

Evidence of entanglements has been primarily inferred from the rheology experiments performed on high molecular weight polymer melts, solutions and networks [1-6]. Recently there have been a few efforts to reproduce the entangled polymer properties through carbon nanotubes [7]. We have studied the global chain dynamics of polymers densely grafted to the nanoparticle surface and discovered that despite the low molecular weight of the polymers studied, dynamics of these polymers resembles that of highly entangled polymers. Our findings provide evidence that

entanglement effect can even be realized in low molecular weight polymers through surface crowding.

Model system we have studied is a solventless fluid termed as self-suspended fluid, created by densely grafting polymer chains to the nanoparticle surface [8, 9]. The system comprises of polymer grafted nanoparticles with no additional solvent present. Degree of surface crowding of a polymer chain can be facilely tuned in this system by changing the polymer grafting density and molecular weight. Furthermore, this materials framework allows the dynamics of confined polymers to be probed in a bulk experiments. Finally, absence of any external solvent excludes any enthalpic interactions between the suspending phase and the suspended phase, allowing the entropy driven polymer chain dynamics to be solely probed.

Cis 1-4 Polyisoprene (PI) is particularly instrumental in studying polymer dynamics considering it is a type-A dielectric [10], implying that the net dipole moment of an entire polymer chain is parallel to the end to end vector of the polymer chain. Dielectric relaxation of PI can be studied over a wide frequency range with the help of broadband dielectric spectroscopy (BDS). Type- A polymers show a peak in the dielectric loss, ε'', spectrum corresponding to the normal mode relaxation, originating from the relaxation of the entire polymer chain. This feature allows the global dynamics of the polymer chain to be studied over a broad range of frequency [11].

3.3 Results and Discussion

We have studied silica nanoparticles (10 ± 2 nm) densely grafted with PI chains. Dielectric relaxation measurements were performed on a Novocontrol broadband dielectric spectrometer by sandwiching the sample between two gold plated copper electrodes. Temperature control was exercised through a quarto cryosystem with a nitrogen gas stream . To the best of our knowledge,

Table 3.1: Physical properties of the samples investigated in the dielectric relaxation study.

M_w	φ (%)	R_g	n	ξ
5000	10	2.23	485	0.454
5000	8	2.23	553	0.425
5000	5.4	2.23	906	0.332
5000	4	2.23	1210	0.287
15000	7.4	3.86	225	0.666
3000	11.1	1.72	1132	0.297

M_w is the molecular weight of the polymer.

φ is the volume fraction of silica nanoparticles.

n is the number of polymer chains attached to each nanoparticle.

ξ is the lateral spacing between the polymer chains.

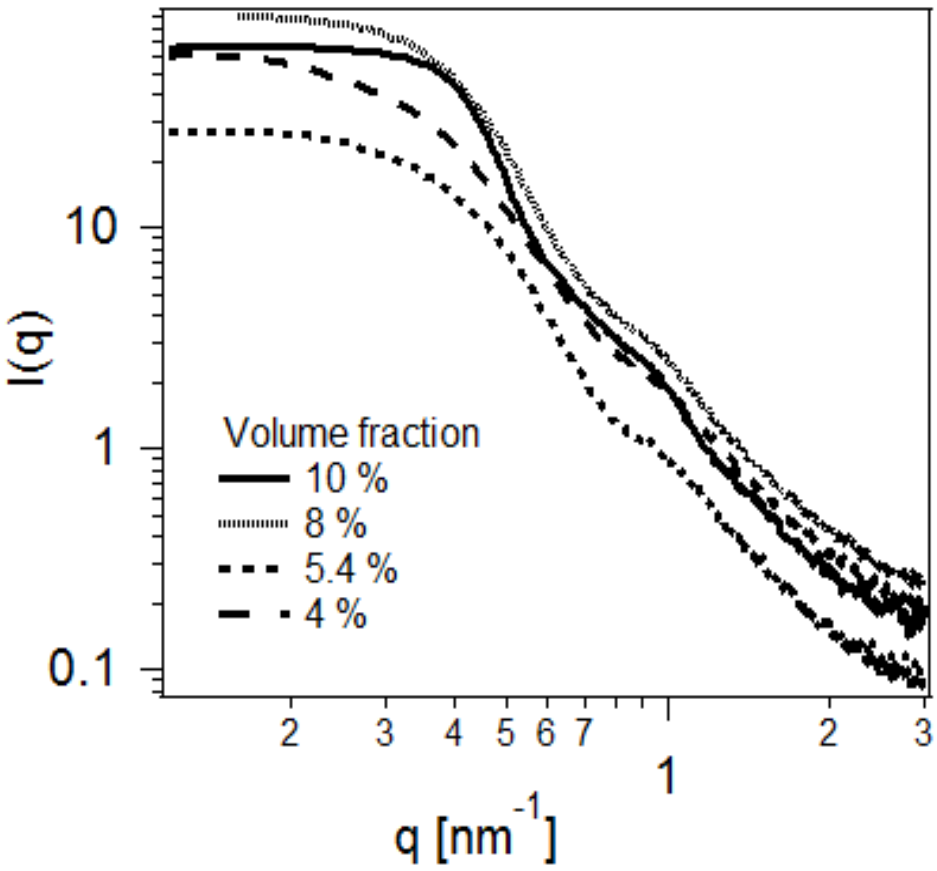

Figure 3.1 Small angle X-ray scattering data: Intensity, *I(q)* vs. wave vector, *q*.

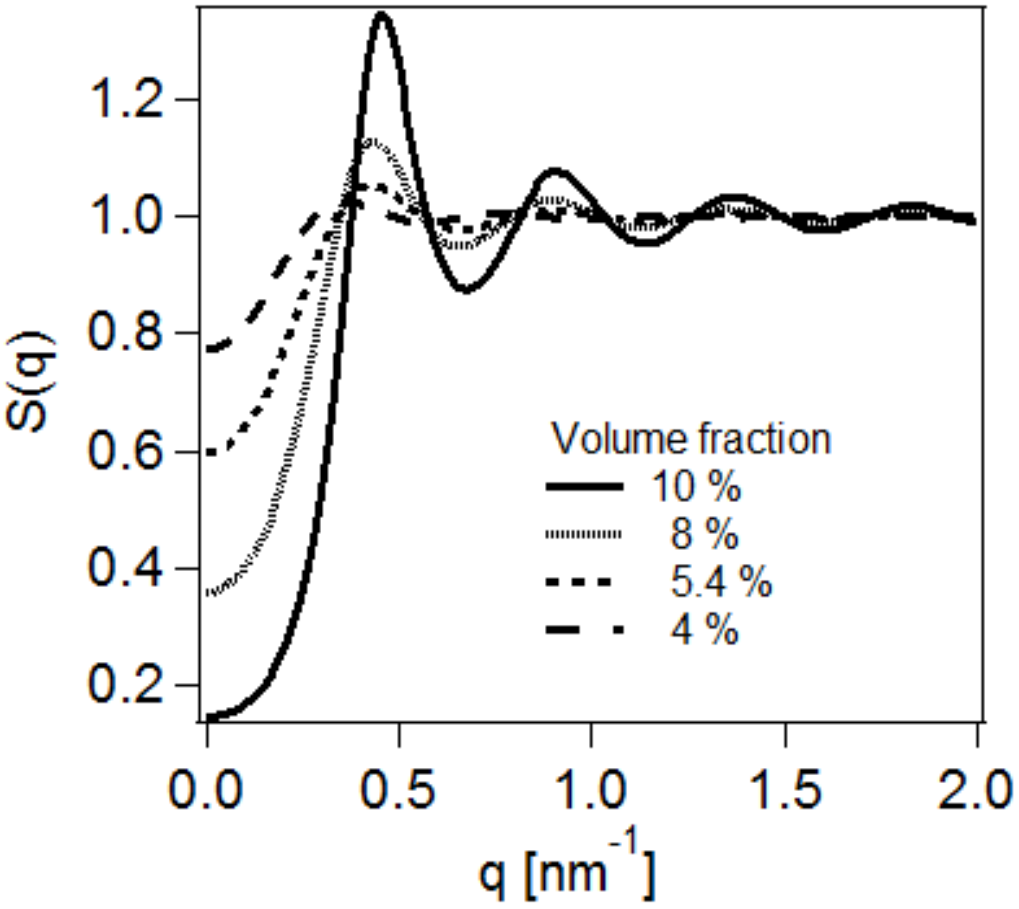

Figure 3.2 Small angle X-ray scattering data: Structure factor, *S(q)*, vs. wave vector, *q*. Inverse of the primary peak position in the *S(q)* is a measure of the interparticle spacing. It can be seen that the interparticle spacing decreases with increasing the nanoparticle volume fraction.

this is the first example where the global chain dynamics of nanoparticle tethered cis 1-4 polyisoprene has been studied. Further, we have also investigated the materials having polystyrene (PS) grafted to silica nanoparticles to study the glass transition temperature (T_g) of tethered polymers.

We have performed small angle X-ray scattering (SAXS) to characterize the nanoparticle dispersion these materials. Figure 3.1 shows the intensity, *I(q)*, vs. wave vector, *q*, at varying nanoparticle volume fraction. The intensity pattern has been fitted with a hard sphere model for the structure factor, implying that the nanoparticles are well dispersed in this system. Resulting factor, *S(q)*, is shown in figure 3.2 at different nanoparticle volume fractions. Spacing between the nanoparticle cores can be estimated as $d = 2\pi/q_{max}$, where q_{max} is the primary peak position of the structure factor. Nanoparticle spacing decreases with increasing the particle volume fraction and *d* is greater than the polymer radius of gyration for the range of volume fractions studied.

Figure 3.3 and 3.4 shows the ε'' vs. frequency, ω, at different temperatures for the untethered and tethered polymer respectively. Several important differences can be immediately noted from the figure: at a given temperature, the normal mode peak is shifted to lower frequency for the tethered polymer, implying a higher relaxation time for the tethered chain. Further, the peaks in the ε'' for the tethered polymer are much broader compared to the untethered polymer, signifying a broader relaxation spectrum for the tethered polymer.

Furthermore, the peak value of ε'' is much higher for the tethered chains in figure 3.4 compared to the untethered polymer in figure 3.3. $\Delta\varepsilon$ is related to the mean square end to end distance of the polymer chain by

$$\Delta\varepsilon = F\left(\frac{4\pi\mu}{3kT}\right)\nu R_e^2 \qquad (3.1)$$

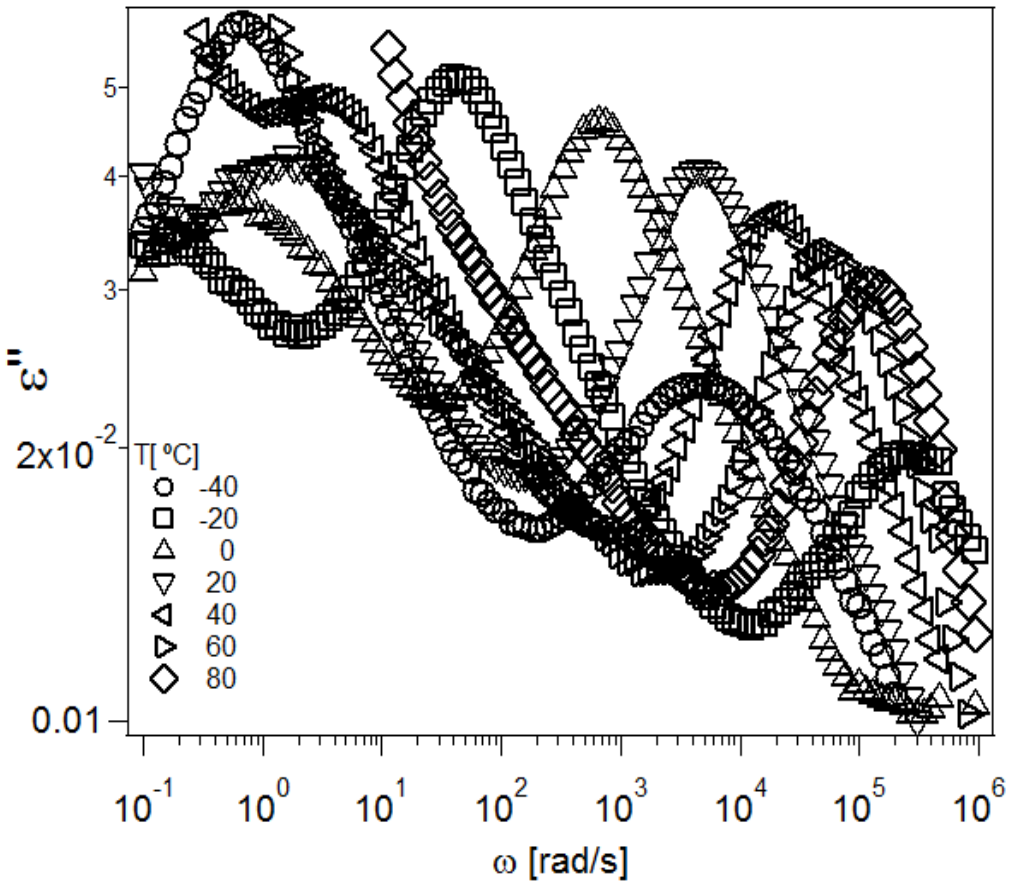

Figure 3.3 Broadband dielectric spectroscopy data showing dielectric loss *ε"* vs. frequency, *ω*, for the polyisoprene with a molecular weight of 5000. Low frequency peak in *ε"* corresponds to the normal mode relaxation of the polymer chain. Peak position shifts to higher frequency with increasing temperature, implying speeding up of the polymer relaxation at higher temperature.

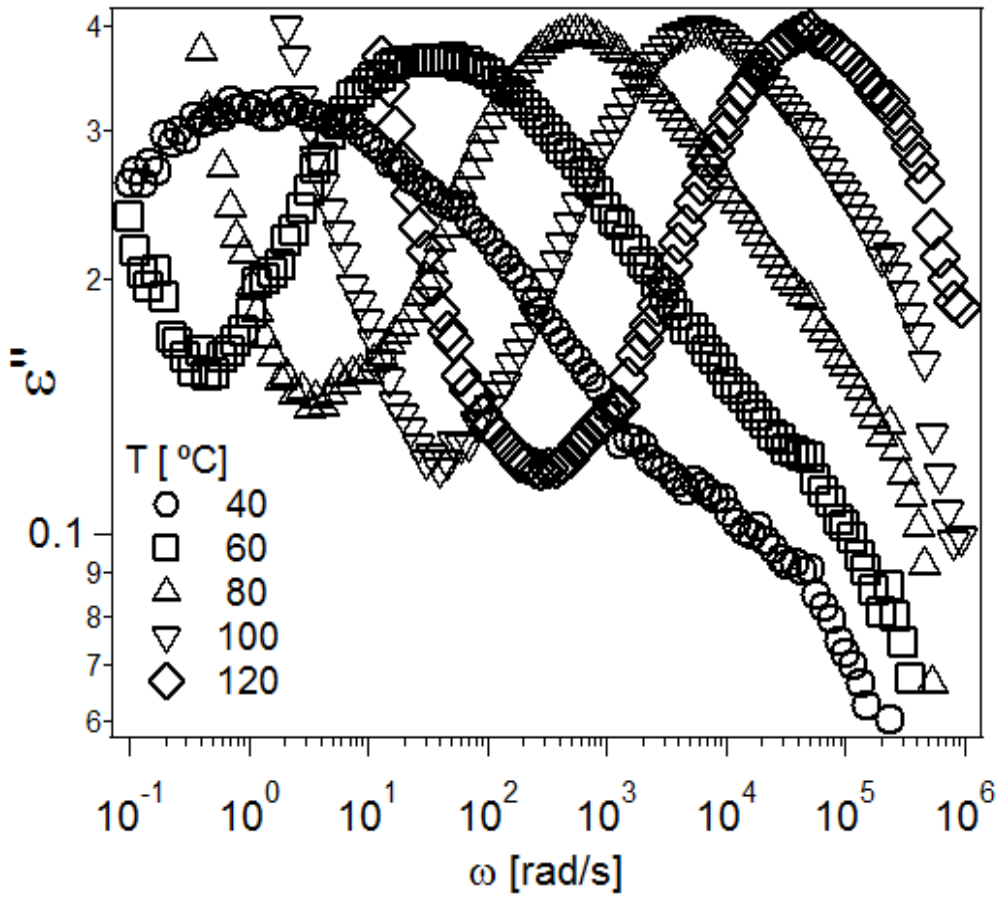

Figure 3.4 *ε''* vs. *ω* for the tethered polyisoprene with a molecular weight of 5000. Volume fraction of silica nanoparticles in the sample is 10 %.

where v is the number density of chains, R_e is the mean square end to end distance of the polymer chains, μ is dipole moment per chain segment, F is a correction factor, k is Boltzmann's constant and T is temperature [12]. From the $\Delta\varepsilon$ values of tethered and untethered chain, we calculate the brush height as ~ 10.5 nm for the tethered polymer chains, which is much larger than the R_g of 2.2 nm, implying that polymer chains are forming extended brushes on the nanoparticle surface.

Another important feature that can be noted from figure 3.3 and 3.4 is that peak value of ε'' is a decreasing function of temperature for the untethered polymer, which is in agreement with eq. (3.1), however for the tethered polymer, the peak value of ε'' actually increases with increase in temperature. This could imply that R_e is increasing with increasing the temperature for the tethered polymer. This is in agreement with the hypothesis we had proposed earlier, based on the observations from temperature dependent rheology of these materials [13].

Figure 3.5 shows the relaxation time for the tethered and untethered polymer as a function of temperature at varying nanoparticle volume fraction. Nanoparticle volume fraction has been varied by changing the polymer grafting density with keeping the tethered polymer molecular weight constant at 5000. Relaxation time has been calculated as $\tau = (2\pi f_{peak})^{-1}$ where f_{peak} is the frequency corresponding to the maximum in ε''. It can be seen from the figure that for a wide range of temperature, the relaxation time of tethered polymer is significantly larger than the untethered polymer, indicating that tethering results into a significant slowdown in the dynamics of the polymer chain. Further, the change in the relaxation time as a function of nanoparticle volume fraction is considerably insignificant.

Boese et al. studied the dielectric relaxation of low molecular weight star PI and found relaxation time to be independent of the number of arms [14]. Albeit this qualitative similarity, relaxation time of the tethered polymers in our system is several orders of magnitude larger than the untethered polymer. This is in contrast to the ratio of 4 widely reported for the star branched polyisoprene up to an arm molecular weight range of 20000 [15]. Ratio of 4 between the relaxation time of a tethered and untethered polymer chain can also be obtained theoretically by solving the Rouse model with appropriate boundary conditions [15].

We have further investigated the effect of changing the tethered polymer molecular weight. Figure 3.6 shows the relaxation time of the untethered and tethered polymer at different tethered polymer molecular weights. As expected, relaxation time of the untethered polymer increases with increasing the molecular weight [1], however the relaxation time of tethered polymer chains does not show a strong dependence on the polymer molecular weight. Increase in the relaxation time produced by tethering is largest for the polymer having the smallest molecular weight, implying that the shortest polymer chain pays the highest entropic penalty for being tethered to the nanoparticle surface.

Aforementioned results clearly demonstrate that although the molecular weight of the polymer chains investigated is not in the highly entangled regime ($M_{e,\ PI} \sim 5000$), relaxation dynamics observed is quite unlike Rouse chains. Besides, relaxation time of the highly entangled star polymers has been observed to be exponentially large compared to the liner polymer relaxation time in the rheology [16] and dielectric relaxation experiments [17]. This suggests that irrespective of their low molecular weight, behavior of the tethered polymers in our system is more similar to the highly entangled star polymers. Further, even for highly entangled star

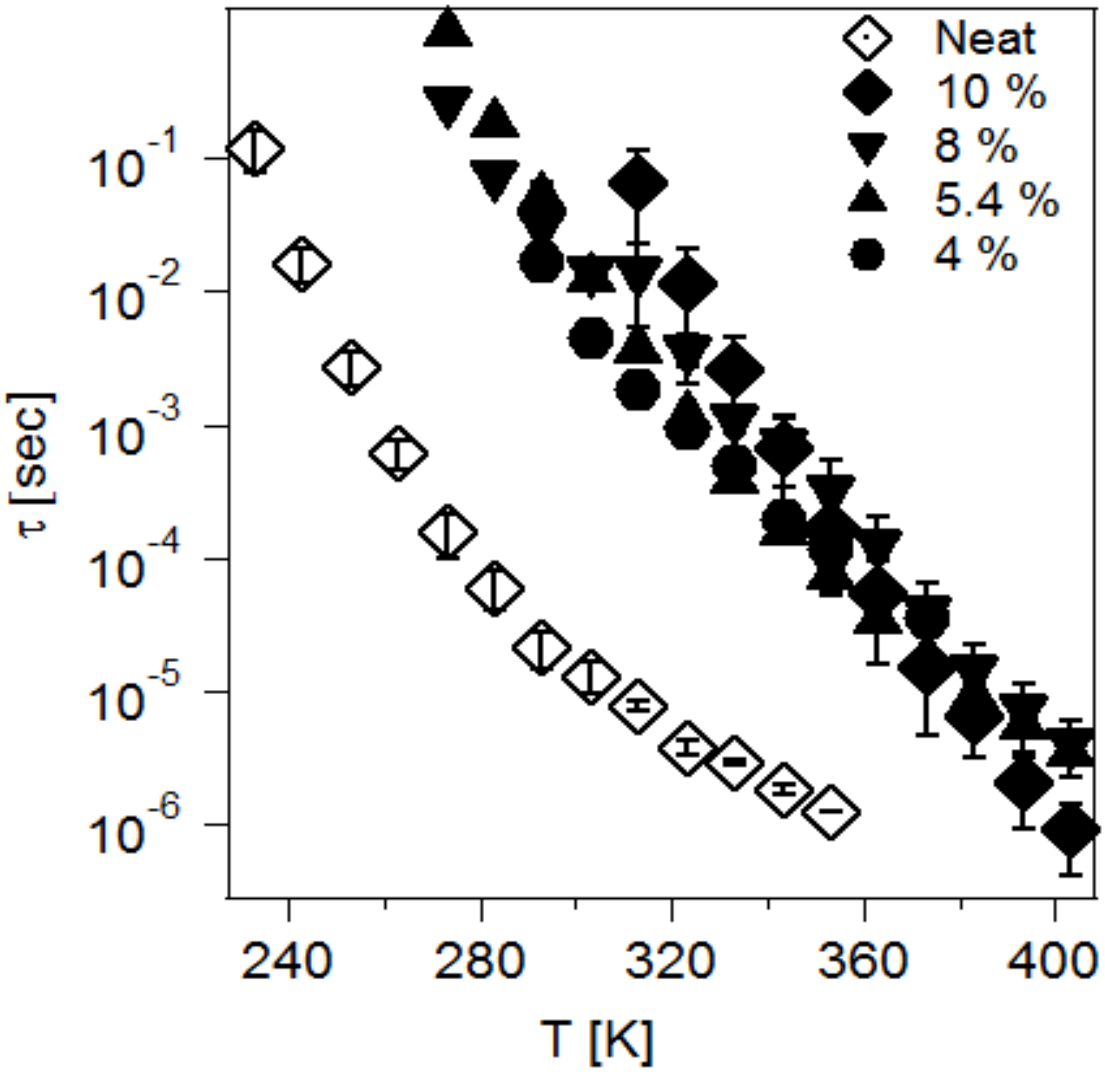

Figure 3.5 Normal mode relaxation time as a function of temperature for the untethered (open symbols) and tethered polyisoprene with a molecular weight of 5000, at different nanoparticle volume fraction. Nanoparticle volume fraction has been varied by changing the polymer grafting density. Tethering results in an unusually large increase in the polymer relaxation time. Relaxation of the tethered polymer does not show a strong dependence on the polymer grafting density or the nanoparticle volume fraction.

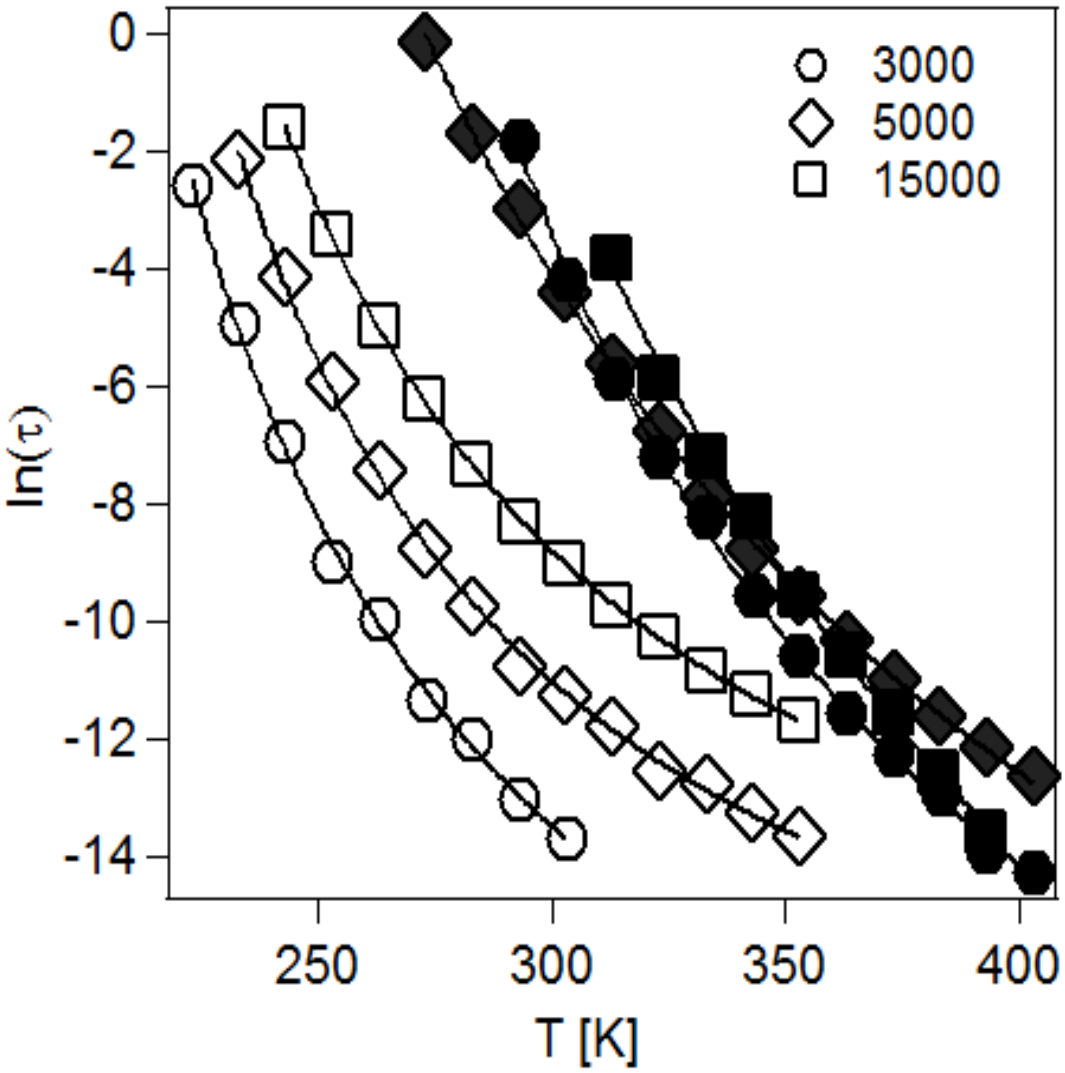

Figure 3.6 Comparison of the relaxation time of the tethered (filled symbols) and untethered polymer (open symbols) for different tethered chain molecular weight. Relaxation time of the untethered polymer increases with increasing the polymer molecular weight. Tethering results in an increase of the normal mode relaxation time for the whole range of molecular weight studied, increase in the relaxation time due to tethering is the highest for the polymer with the lowest molecular weight. Solid lines are fits with the VFT equation described in the text.

Data for the Molecular weight of 3000 was provided by S. A. Kim.

polymers, the relaxation time was found to be independent of the number of arms and a broader relaxation spectrum was observed [17].

Entangled polymers exhibit longer relaxation times compared to the Rouse chains due to the fact that the diffusion length for a relaxation event is equal to the length of the primitive path of the chain, $<L>$, as opposed to R_g for a Rouse chain [1-6]. Considering their low molecular weight, polymers studied here are not highly entangled, however the end to end distance of the tethered polymer chain is much larger compared to the R_g of the polymer, as mentioned previously. In this scenario, the diffusion length, an arm needs to travel for the longest relaxation time should be the brush height, h. Contrary to the entangled polymer, where $<L> \sim N$, where N is the degree of polymerization; here h is determined by both the molecular weight and the grafting density of polymer chains.

Spacing between the grafted polymers, ξ, for the various systems investigated in this study is listed in table 3.1. It can be seen that for all the samples, ξ is much smaller than the Kuhn length of the polymer (.82 nm), which forces the polymer chains to extend out and form brushes on the particle surface. Analogous to a chain in a tube, this restricts the lateral movement of these polymer brushes due to the presence of their neighbors. Reptation is not possible in this situation, since the polymer chain is anchored at one end. Hence, the mode of relaxation is the arm retraction, wherein the polymer chain relaxes by the exponentially unlikely fluctuations in the tube length [16].

Relaxation time for highly entangled star polymers is given by [16]

$$\tau \sim N^{\frac{5}{2}} \exp\left(\frac{\gamma' <L>^2}{2R_g^2}\right) \qquad (3.2)$$

Where N is the number of entanglements per arm, $<L>$ is the contour length of the primitive of the entangled arm, R_g is the radius of gyration, γ' is the effective spring constant. Estimation of N is not straightforward for the present case, hence we have assumes that the primitive path length of the effective entangled arm is h, which gives $N \sim h^2/R_g^2$. Eq. (3.2) results in

$$\tau \sim \left(\frac{h}{R_g}\right)^5 \exp\left(\frac{\gamma' h^2}{2R_g^2}\right) \qquad (3.3)$$

Assuming that the relaxation time of the untethered rouse chains, $\tau_u \sim N_a^2$ and relating the end to end distance to $\Delta\varepsilon$ by eq. 3.1, ratio of the tethered and untethered polymer can be obtained as

$$\frac{\tau_t}{\tau_u} \sim \left(\frac{\Delta\varepsilon_t}{\Delta\varepsilon_u(1-\varphi)}\right)^{\frac{5}{2}} \left[\exp\left(\frac{\gamma' \Delta\varepsilon_t}{2\Delta\varepsilon_u(1-\varphi)}\right)\right] / N_a^2 \qquad (3.4)$$

Where τ_u is the relaxation time for the untethered polymer and τ_t is the relaxation time for the tethered polymer, φ is the volume fraction of silica nanoparticles, N_a is the number of Kuhn segments in the arm and γ is the spring constant for the quadratic potential, assumed to be .61.

In the range of grating densities investigated, h is not changing significantly; therefore we do not see a significant change in the polymer relaxation time at different polymer grafting density in Figure 3.5. From the Δε values for samples shown in figure 3.8, h/R_g values for the chains with molecular weight 3000, 5000 and 15000 are 5.97, 4.68, and 4.49 respectively. Thus, the ratio of h/R_g increases with decreasing molecular weight, therefore the ratio of the relaxation time of tethered and untethered polymer is the largest for the polymer with the smallest molecular weight. At a given temperature, the ratio calculated from eq. (3.4) turns out to be $8\text{x}10^5$, $1.1\text{x}10^3$ and 61 respectively for the molecular weight of 3000, 5000 and 15000, which are close to the corresponding experimentally obtained values of $1.4\text{x}\ 10^5$, 133 and 38.

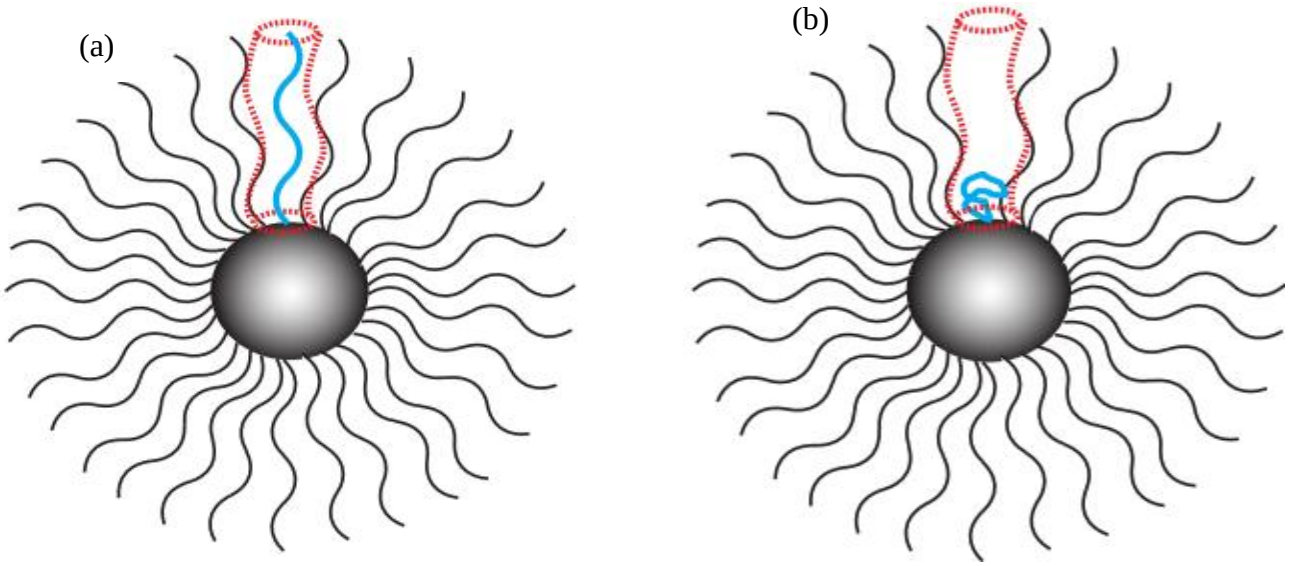

Figure 3.7 (a) Schematic representation of a polymer chain confined in a tube like region by the neighboring polymer chains. (b) Arm retraction mechanism for the relaxation of the polymer chain confined in the tube.

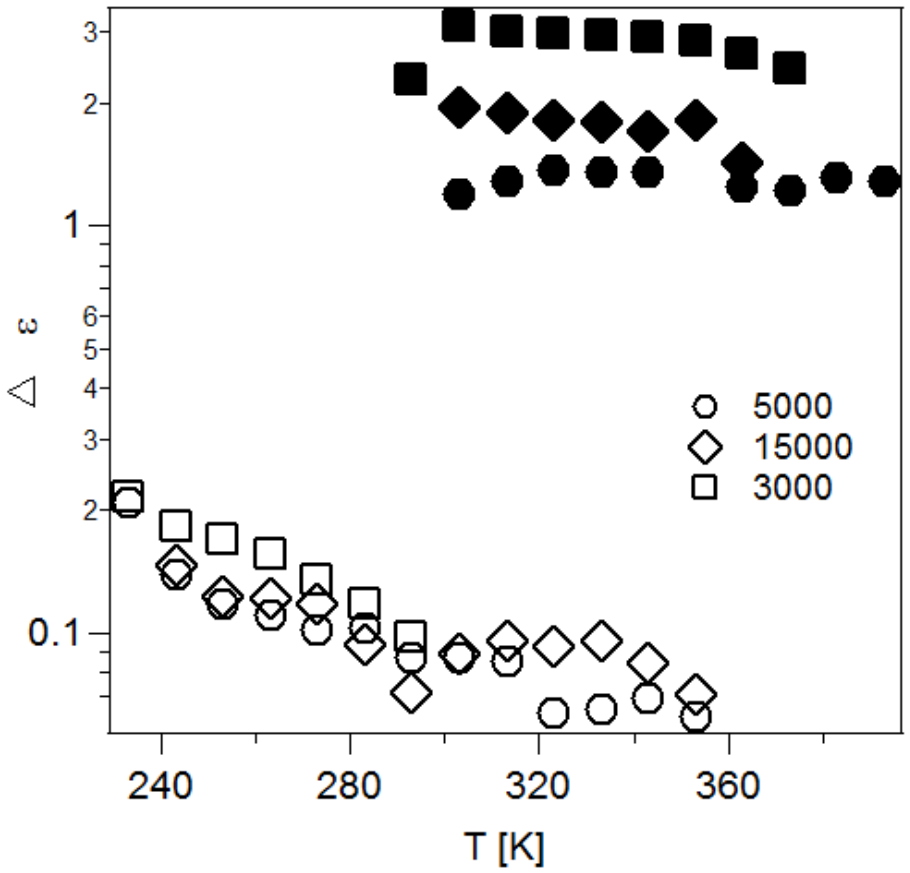

Figure 3.8 $\Delta\varepsilon$ as a function of temperature for the tethered (filled symbols) and untethered (open symbols) polymer. $\Delta\varepsilon$ value for the tethered polymer is much larger than untethered polymer, indicating larger end to end distance for the tethered polymer.

A direct confirmation of the entangled polymer dynamics is seen in the rheology of these materials. At moderate nanoparticle volume fraction, the self-suspended fluids display viscoelastic behavior dominated by the storage modulus, *G'*, whereas the untethered polymer is a Newtonian liquid at same conditions and only displays a non-zero loss modulus, *G"*, as shown in figure 3.9. Furthermore, the elastic modulus at high nanoparticle volume fraction is surprisingly close to the plateau modulus of highly entangled PI (~ .3 MPa) [2]. Decrease in the elastic modulus with decreasing nanoparticle volume fraction can be explained by the fact that the nanoparticle motion becomes faster with decreasing the volume fraction. Some of the stress can therefore be relaxed by the nanoparticle motion, giving rise to lower viscoelastic moduli at low nanoparticle volume fraction. This observation is similar to the findings for branched polymers, wherein faster dynamics of the branch point produces faster relaxation [18].

Solid lines in figure 3.6 show a fit with the Vogel Fulcher Tamman (VFT) equation [19] given by

$$ln(\tau) = A + \left(\frac{B}{T - C}\right) \qquad (3.5)$$

Where *exp(A)* is the high temperature limit of the relaxation time, *B* is the activation energy, *T* is temperature and *C* is the Vogel temperature. Values of the fitting parameters for the untethered and tethered polymers are listed in table 3.2 and 3.3 respectively. Temperature dependence of the relaxation time is different for the tethered and untethered polymers in figure 3.5 and 3.6, whereas it was found to be the same for the star polymers. This implies that the temperature dependence of the monomer friction coefficient is fundamentally different for the tethered polymers in our system. This feature also restricts the exact quantitative comparison between the ratio of relaxation time of the tethered and untethered polymer with the proposed model.

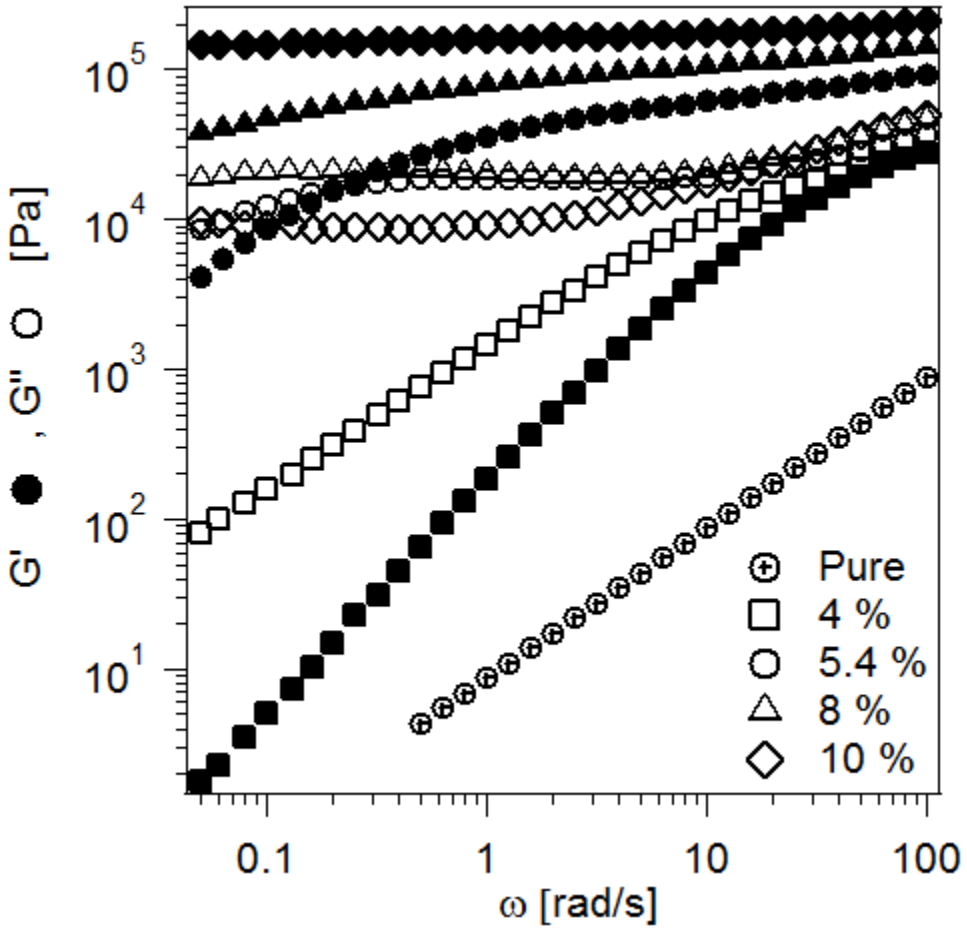

Figure 3.9 Storage modulus, *G'* (close symbols), and loss modulus, *G*"(open symbols), at multiple nanoparticle volume fractions at a temperature of 20 ˚C. Untethered polymer only shows a viscous component in the viscoelastic spectrum. Elastic modulus of the self-suspended fluids increases with increasing the nanoparticle volume fraction to approach the plateau modulus of highly entangled polyisoprene.

Table 3.2: VFT fit parameters for the untethered polymers in figure 3.6

M_w	A	B	C
3000	-24.072	1602	148.9
5000	-20.595	1323.2	161.94
15000	-19.45	1506	158.8

Table 3.3 VFT fit parameters for the tethered polymers in figure 3.6

M_w	A	B	C
3000	-27.17	3013.5	175.18
5000	-28.3	4537	113.18
15000	-36.5	6360.9	117.4

Furthermore, the activation energy, B for the tethered polymer is much higher than the untethered polymer. Higher activation energy can potentially arise due to the fact the chains are frustrated from their native gauche conformation, hence higher energy is needed to achieve the relaxation. Higher activation energy for confined polymers was also reported previously in the study of PI confined in porous glass [20]

Our findings are considerably different from the previous finding on the normal mode relaxation of the polyisoprene in nanocomposites. Ding et al. [21] studied the normal mode and segmental mode relaxation of polyisoprene C_{60} nanocomposites and found very insignificant change in normal mode timescales due to addition of C_{60} fillers to the PI matrix. Mays et al. [22] studied polyisoprene clay composites and found that normal mode and segmental mode relaxation times remain unaffected by the addition of fillers for small molecular weight polyisoprene and for large molecular weight polyisoprene, normal mode relaxation time was found to increase with increasing clay content.

We have further investigated the segmental dynamics of the polymer chains by studying the T_g. Effect of changing the polymer molecular weight and grafting density on T_g is strikingly similar to the effects seen in the global chain dynamics investigated through BDS. We find that the T_g increases due to tethering of the polymer chain and this increase in T_g is independent of the polymer grafting density as shown in figure 3.10. We have further studied the effect of tethering on polymer T_g by synthesizing materials having polystyrene (PS) as tethered polymer chain.

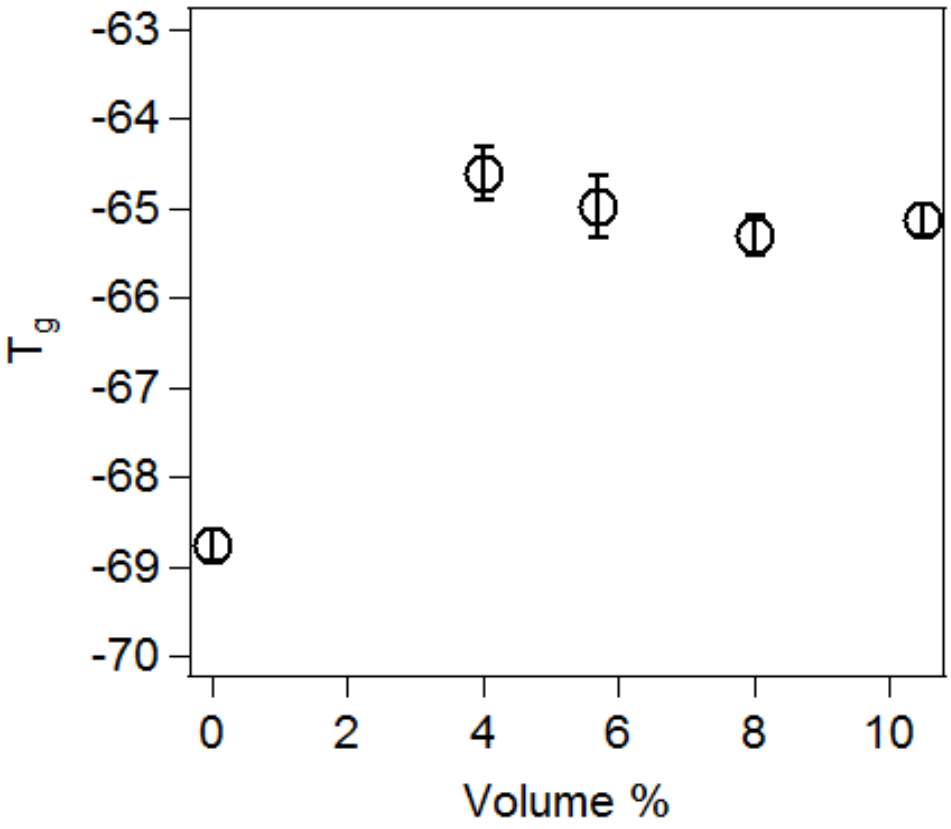

Figure 3.10 T_g of the tethered polymer vs. the nanoparticle volume fraction. T_g of the polymer increases due to tethering and is almost independent of the nanoparticle volume fraction.

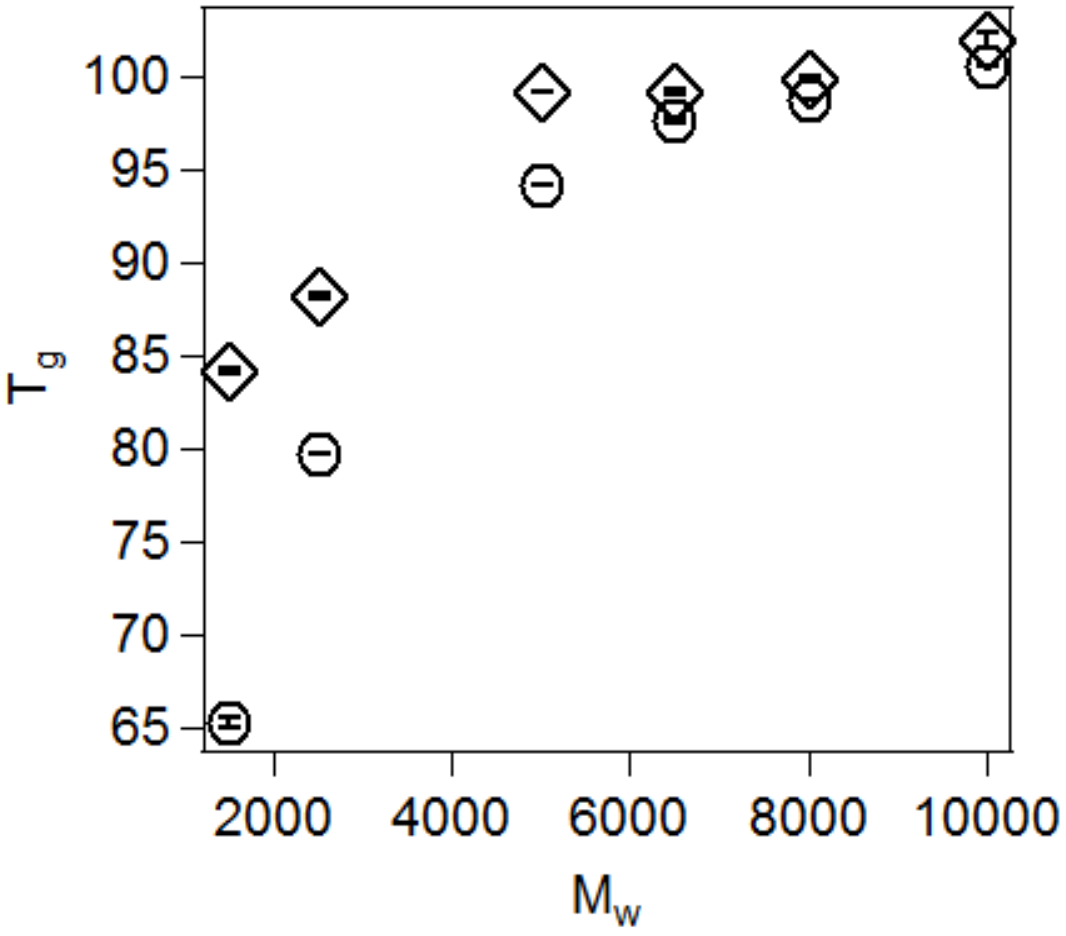

Figure 3.11 T_g of the tethered an untethered polystyrene at different polymer molecular weight. T_g of the polymer increases due to tethering with the increase becoming progressively smaller for larger molecular weight polymers.

We find that also for the materials having PS as the tethered chain, T_g increases due to tethering. Increment in polymer T_g tends to reduce with increasing the molecular weight of tethered polymer chain, as shown in figure 3.11. These findings are again in agreement with the global chain relaxation data shown in figure 3.6 showing that the increase in the relaxation time due to tethering is the highest for the polymer with the lowest molecular weight. Our findings on the effect of molecular weight on polymer T_g are also in agreement with the previous work by Savin et al. [23] wherein the T_g was found to increase with tethering and the smallest molecular weight polymer exhibited the largest increase in the T_g with tethering.

3.4 Conclusions

We have studied the dielectric relaxation of densely grafted polymers using broadband dielectric spectroscopy. We find that the tethered polymers exhibit unusually slow dynamics. Behavior of tethered polymers in this scenario is more akin to the highly entangled polymers, irrespective their low molecular weight. Our finding could further have technological importance for the wide variety of applications utilizing high molecular weight polymers, wherein similar properties could be achieved by using low molecular weight tethered polymers. This work also entails for the development of a detailed theoretical framework for describing the dynamics of polymers in highly constrained environments.

ACKNOWLEDGEMENTS

This work was supported by the National Science Foundation, Award No. DMR-1006323 and by Award No. KUS-C1-018-02, made by King Abdullah University of Science and Technology (KAUST). Facilities available through the Cornell Center for Materials Research (CCMR) were used for this study.

REFERENCES

1. G. C. Berry, T. G. Fox, Adv. Polym. Sci. **5**, 161 (1968).
2. W. W Graessley, Adv. Polym. Sci. **16** (1974).
3. M. Doi, S. F. Edwards, Theory of polymer dynamics (Oxford Univ. Press, 1988).
4. J. H. Lee, L. A. Archer, J. Polym. Sci: part B: Polym. Phys. **39**, 2501 (2001).
5. T. C. B. Mcleish, Adv. Polym. Sci. **51**, 1379 (2002).
6. P. G. de Gennes, J. Chem. Phys. **55**, 572 (1971).
7. M. Xu, D. N. Futaba, T. Yamada, M. Yumura, K. Hata, Science **3**, 1365 (2010).
8. P. Agarwal, H. Qi, and L.A. Archer, Nano Lett. **10**, 111 (2010); P. Agarwal, L. A. Archer, Phys. Rev. E **83**, 041402, 2011.
9. H. Y. Yu, D. L. Koch, Langmuir **26**, 16801 (2010).
10. M. E. Baur, W. H. Stockmayer, J. Chem. Phys. **43**, 4319 (1965).
11. K. Adachi, T. Kotaka, Prog. Polym. Sci. **18**, 585 (1993).
12. H. Watanabe, Macromol. Rapid. Comm. **22**, 127 (2001).
13. P. Agarwal, S. Srivastava, L. A. Archer, Phys. Rev. Lett. **107**, 268302 (2011).
14. D. Boese, F. Kremer, L. J. Fetters, Macromolecules **20**, 1826 (1990).
15. W. W. Graessley, Adv. Polym Sci **47**, 67 (1982).
16. L. J. Fetters, A. D. Kiss, D. S. Pearson, G. F. Quack, F. J. Vitus, Macromolecules **26**, 647 (1993).
17. Y. Matsumiya, H. Watanabe, Macromolecules **34**, 5702 (2001).
18. A. L. Frischknecht, S. T. Milner, A. Pryke, R. N. Young, R. Hawkins, T. C. B. Mcleish, Macromolecules **35**, 4801 (2002).

19. C. A. Angell, K. L Ngai. G. B. Mckenna, P. F. Mcmillan, S. W. Martin, J. Appl. Phys. **88**, 3113 (2000).

20. Q. Zhang, L. A. Archer, Langmuir **19**, 8094 (2003).

21. Y. Ding, S. Pawlus, A. P. Sokolov, J. F. Douglas, A. Karim, C. L. Soles, Macromolecules **42**, 3201 (2009).

22. J. Mijovic, H. Lee, J. Kenny, J. Mays, Macromolecules **39**, 2172 (2006).

23. D. A. Savin, J. Pyun, G. D. Patterson, T. Kowalewski, K. Matyjaszewski, J. Polym. Sci: part B: Polym. Phys. **40**, 2667, 2002.

CHAPTER 4

Nanoparticle Structure, Dynamics and Rheology of Self-Suspended Nanoparticle Fluids

4.1 Abstract

We have investigated the effect of changing nanoparticle volume fraction and temperature on the structure, rheology and nanoparticle dynamics on the class of a self suspended fluid created by densely grafting polymer chains to the nanoparticle surface. We find that the viscosity and nanoparticle relaxation times increase with increasing the nanoparticle volume fraction. Effect of temperature change shows intriguing features wherein at moderate nanoparticle volume fractions, rheology and nanoparticle correlation times show very weak temperature dependence. At low nanoparticle volume fraction, viscosity and nanoparticle correlation times are a decreasing function of temperature. For the whole range of temperature and nanoparticle volume fraction, the nanoparticles motion was found to be hyperdiffusive in nature.

4.2 Introduction

Rheology of nanoparticle suspensions has been an area of intense scientific activity for the past century. Particularly for the case of macromolecular suspending medium, interesting physical phenomena have been uncovered, that originate from the comparable nanoscale dimensions of the fillers and the characteristic length scale of the suspending polymer medium [1-4]. Common problem encountered with the nanoscale fillers is the aggregation of fillers due to strong Van der Walls attractive forces, which has been typically overcome by sterically stabilizing the nanoparticles with polymeric ligands. There have been significant advances in terms of synthetic schemes for grafting polymers onto nanoparticle surfaces and following that many studies have been reported on the structure and dynamics of suspensions of hairy nanoparticles dispersed in a host suspending medium [5-7].

Recent advances in the experimental techniques have allowed the direct measurement of particle dynamics and have proven to be instrumental in understanding the flow behavior of nanoparticle suspension. X-ray photon correlation spectroscopy (XPCS) has emerged as a powerful tool for studying the particle dynamics at a small length scale and a sufficiently long time scale. XPCS is similar to dynamic light scattering, with the low wavelength of the X-ray providing access to smaller length scales. These features have made XPCS a particularly suitable technique for studying the slow dynamics in colloidal glasses [8-14].

Here we have studied the rheology and nanoparticle dynamics in a special class of self-suspended fluids over a range of temperature and nanoparticle volume fraction. Model system we study is created by densely grafting polymers to the nanoparticle surface [15-19]. Nanoparticle volume fraction and polymer molecular weight can be facilely tuned in this system, allowing the structure and dynamics of these materials to be studied over a wide range. Absence of any external solvent in these systems precludes the temperature dependent enthalpic interaction between the suspended and the suspending phase. Rheology of these systems can be tuned form Newtonian behavior to soft glassy rheology, allowing the nanoparticle dynamics to be studied over a wide range of rheological characteristics.

Effect of temperature change on the suspension rheology still remains poorly understood and there is negligible amount of experimental data available on the effect of temperature on the dense suspension rheology. The system considered here is particularly interesting since the nanoparticle structure and dynamics is mediated by the polymer chains tethered to the nanoparticles, which have to fill the interparticle space uniformly [18]. Entropic freedom of the polymer chains and hence the severity of the space filling constraint can be tuned by changing

the temperature and we have found unusual effects in the rheology and nanoparticle dynamics of the system studied here.

4.3 Materials and Methods

Materials we have studied comprise of polyisoprene (PI) chains tethered to silica nanoparticles. Amine terminated PI was synthesized by anionic polymerization in cyclohexane using sec-butyl-lithium as the initiator. Method reported previously in the literature was followed to introduce amine functional group at the polymer chain end [20]. Commercially available silica (LUDOX-SM30) was functionalized with sulfonic acid by reacting with a silane [21] and further reacted with amine terminated PI. Unreacted polymer was removed by doing multiple purification cycles described in the appendix of chapter 2. Molecular weight of PI is 5000 (polydispersity index = 1.05) and size of the silica nanoparticle is 10 nm for this study. Nanoparticle volume fraction has been varied by changing the polymer grafting density and keeping the molecular weight of the tethered polymer constant.

Nanoparticle structure was probed by Small Angle X-ray Scattering experiments at different temperatures. SAXS measurements were performed at Anton Paar SAXSess instrument using Cu-Kα radiation with a wavelength of .1542 nm. The instrument produces a line collimated X-ray beam with a block camera setup. Generalized indirect Fourier transform (GIFT) method was employed to de-smear the intensity profile, and further obtain the form factor and structure factor. Monodispersed hard sphere structure factor model with Percus Yevick closure was employed in the GIFT method to obtain the structure factor [22].

Rheology measurements were performed at Anton Paar MCR 501 rheometer equipped with cone and plate geometry. Flow curves were constructed by applying a steady shear rate and data was

recorded when the shear stress attains a steady state value at a given shear rate. Same procedure was followed at different temperatures to construct flow curves at multiple temperatures. Sufficient waiting time was allowed between the application of different shear rate, with the waiting time kept long compared to the measurement time to ensure that the results are not affected by aging [23].

XPCS measurements were performed at the beamline 8-ID-I at Advanced Photon Source. Details regarding the beamline optics can be found elsewhere [24]. Scattering of a partially coherent X-ray beam from the particles results in a speckle pattern and the temporal evolution of this speckle pattern is dependent on the particle dynamics in the medium. Speckle patterns are analyzed to obtain the intensity-intensity time autocorrelation function $g_2(t)$ at multiple wave vectors. Intensity correlation functions $g_2(q,t)$ were fitted to a stretched exponential functional form given by

$$g_2(q,t) = 1 + bexp\left[-\left(\frac{t}{\tau}\right)^{\beta}\right] \qquad (4.1)$$

to obtain the nanoparticle correlation time. Here τ is the nanoparticle correlation time, β is the stretching exponent and b is the contrast factor dependent on the X-ray optics of the beamline [25].

4.4 Results and Discussion

Figure 4.1 shows the intensity, $I(q)$, vs. wave vector, q, for the samples reported here. It can be seen that the scattering pattern does not show a significant change with change in temperature for these materials. This is an important finding that underscores the single component nature and spatial homogeneity of these systems. This also confirms that the

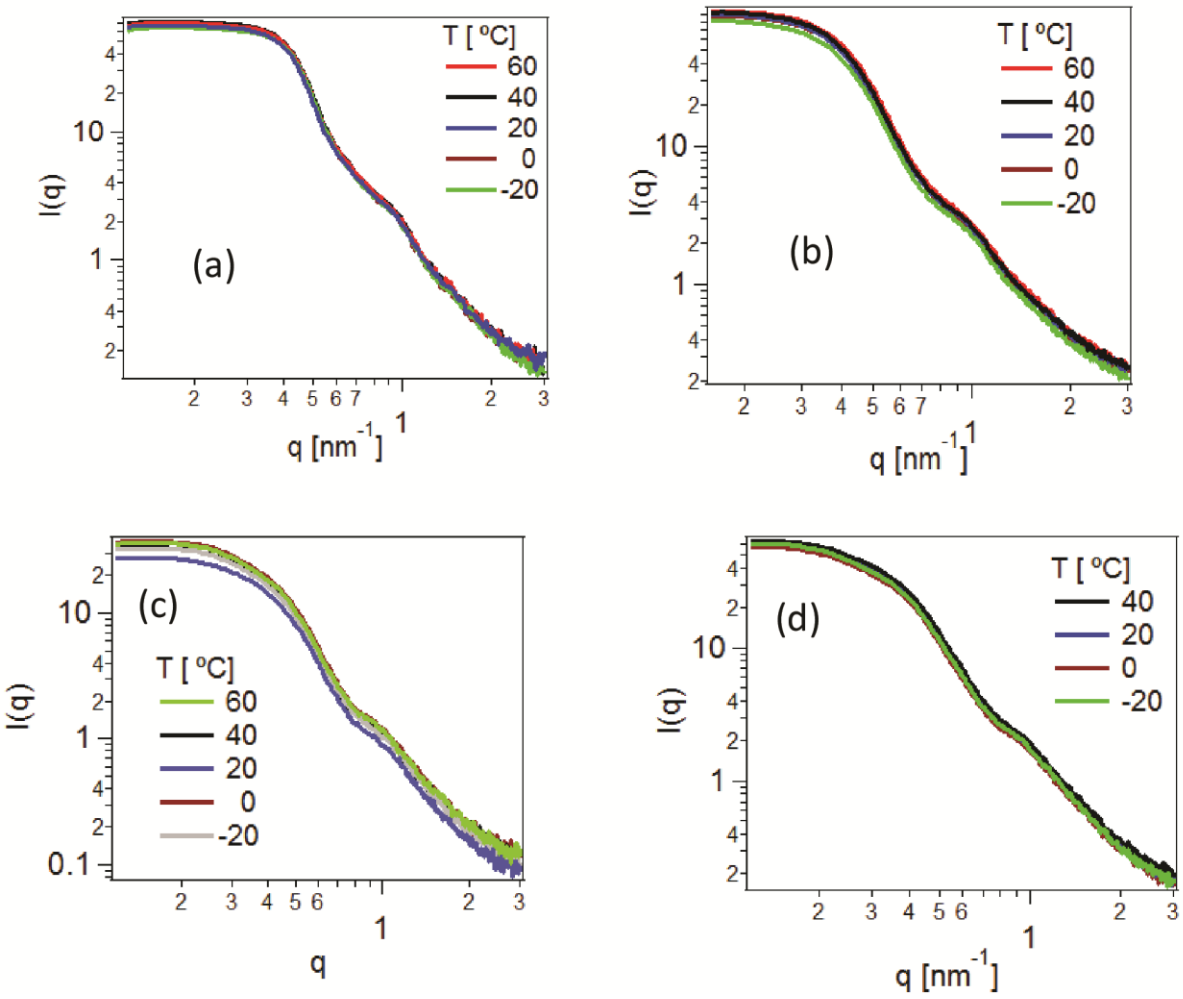

Figure 4.1 Intensity, *I(q)*, vs. wave vector, *q*, at multiple temperatures for samples containing different volume fraction of silica nanoparticles (a) 10 % , (b) 8%, (c) 5.4 %, (d) 4 % . Intensity pattern shows no significant change with temperature for all of the samples.

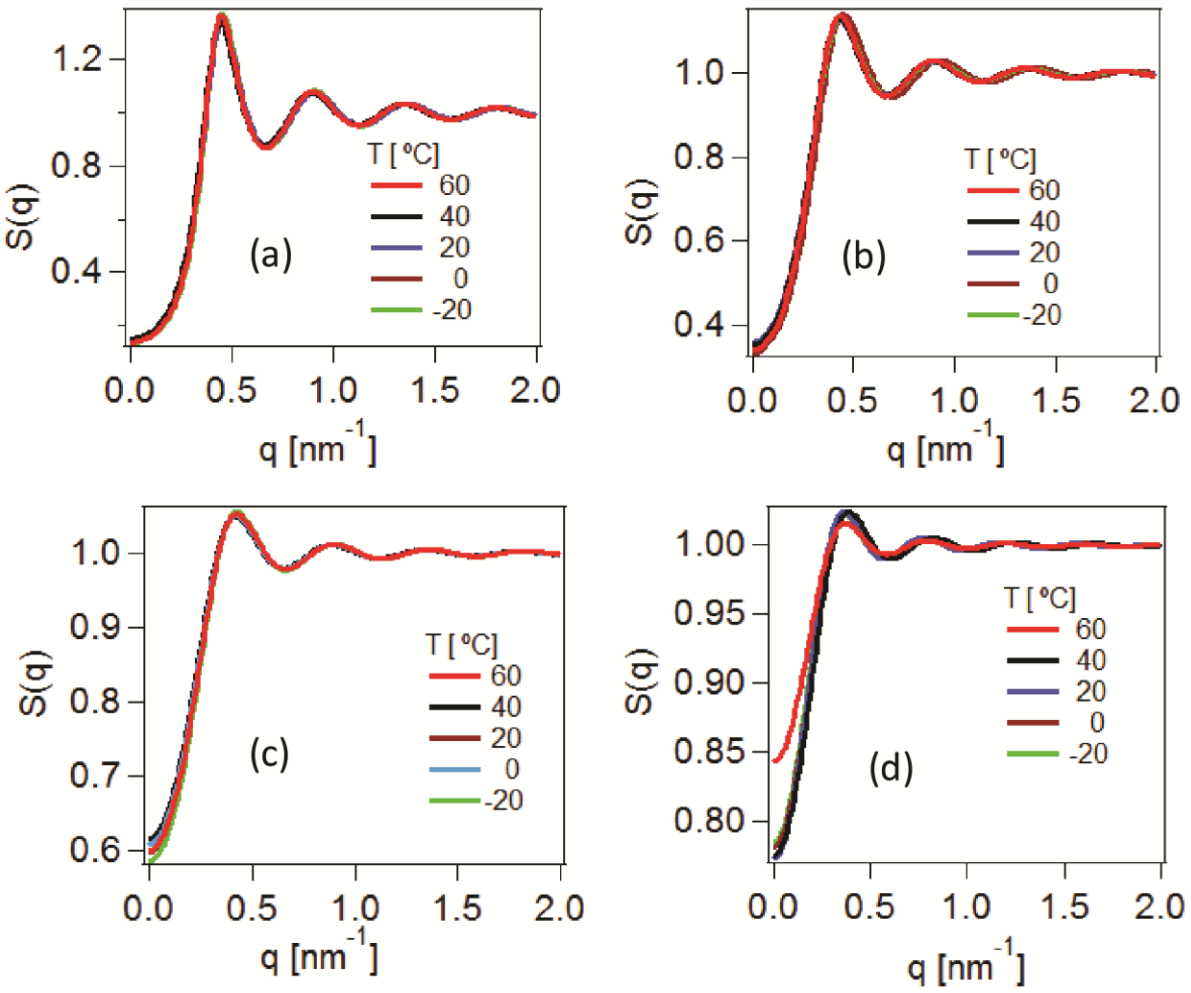

Figure 4.2 Structure factor, *S(q)*, vs. wave vector, *q*, obtained from the intensity patterns show in figure 4.1. (a) 10 % , (b) 8%, (c) 5.4 %, (d) 4 % . It can be seen that the structure factor also does not show any significant variation with temperature.

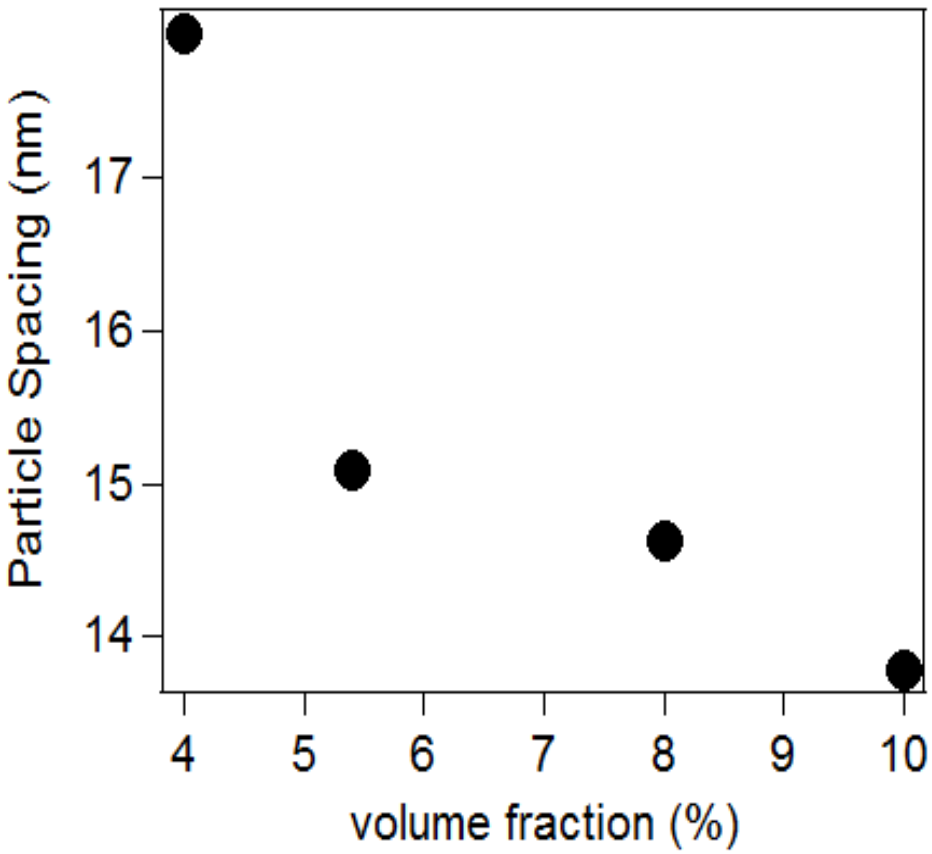

Figure 4.3 Nanoparticle spacing obtained from the primary peak position of the structure factor in figure 4.2. Nanoparticle spacing decreases with increasing nanoparticle volume fraction.

nanoparticle arrangement is not changing during the temperature dependent XPCS measurement that we present later in this article.

Intensity profiles shown in figure 4.1 can be fitted with a hard sphere model to obtain the structure factor, *S(q)*. Resulting structure factor also does not show a significant temperature dependence, as shown in figure 4.2. Interparticle spacing, *d*, can be obtained from the primary peak position, q_{max}, of the *S(q)* by $d = 2\pi/q_{max}$. Figure 4.3 shows the nanoparticle spacing as a function of nanoparticle volume fraction, showing that increase in nanoparticle volume fraction results in decreased nanoparticle spacing, implying a more crowded environment for the nanoparticles at a higher volume fraction.

Figures 4.4-4.7 show the viscosity vs. shear rate at multiple temperatures for the samples with varying nanoparticle volume fractions. For 10% and 8% volume fraction samples in figure 4.4 and 4.5, the viscosity is almost independent of temperature. The untethered polymer viscosity decreases significantly in this range of temperature as shown in figure 4.8, which is typically the case for polymer melts. Behavior shown in figure 4.4 and 4.5 is in agreement with the "thermal jamming" behavior discussed later in chapter 5, wherein increase in temperature enhances the degree of jamming in the system [17].

On the contrary, for samples with volume fraction of 5.4 % and 4 %, viscosity decreases strongly with increasing the temperature (figures 4.6 and 4.7),. Remarkably, there is Newtonian regime in the viscosity for these samples, where the viscosity is independent of the applied shear rate; nevertheless the value of the Newtonian viscosity is several orders of magnitude higher than the viscosity of untethered polymer at the corresponding temperature (figure 4.8). Increase in the suspension viscosity predicted by Einstein's or Batchelor's equation is quite insignificant

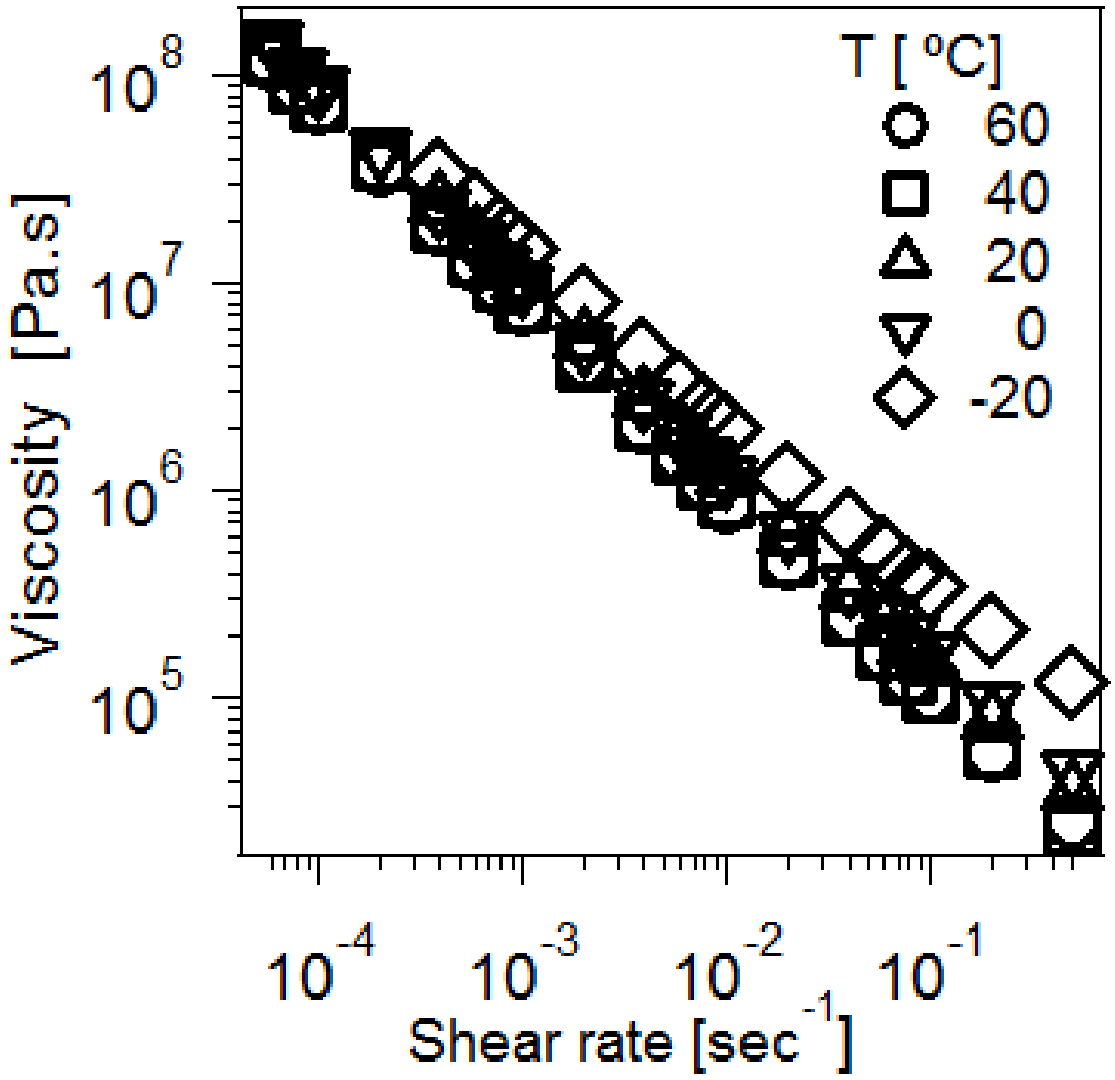

Figure 4.4 Viscosity vs. shear rate at different temperatures for sample with nanoparticle volume fraction of 10 %.

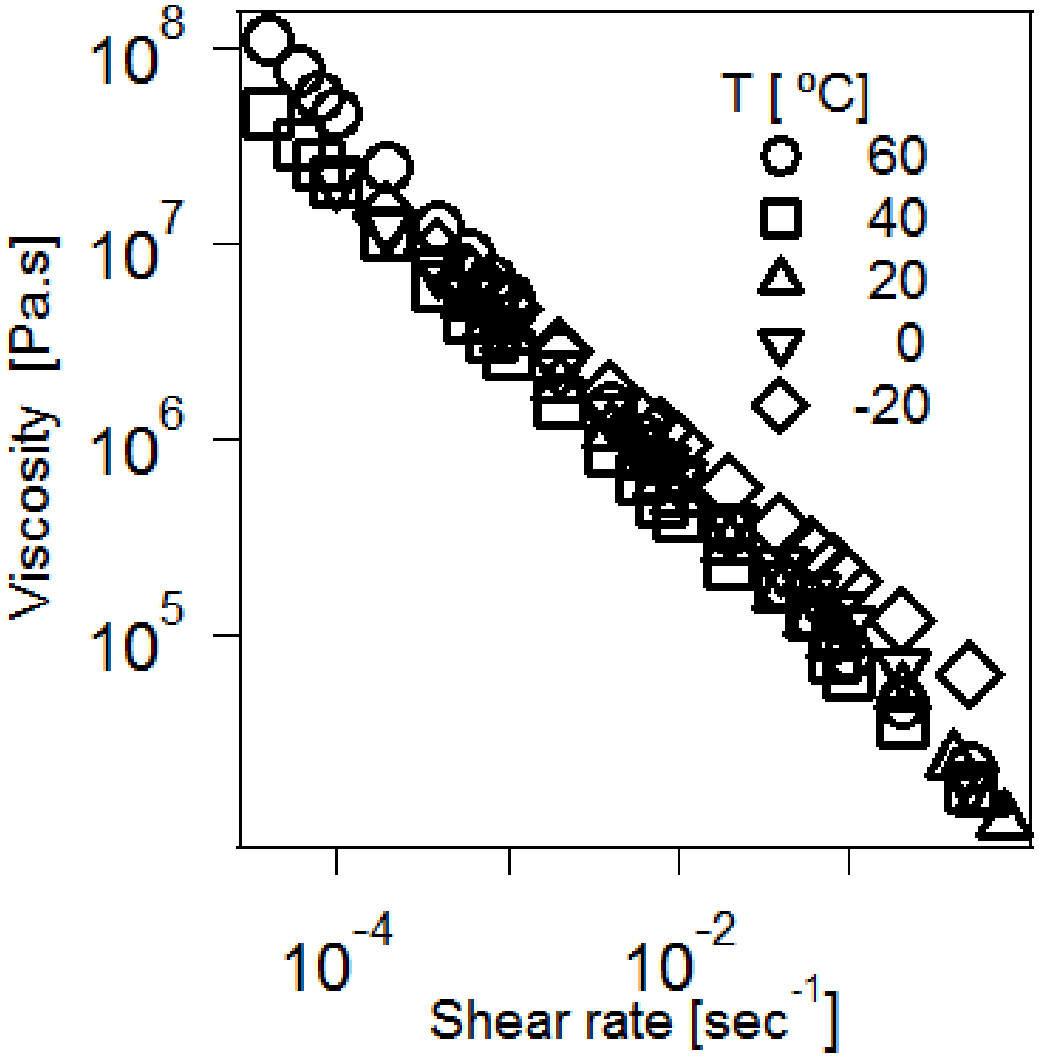

Figure 4.5 Viscosity vs. shear rate at different temperatures for sample with nanoparticle volume fraction of 8 %.

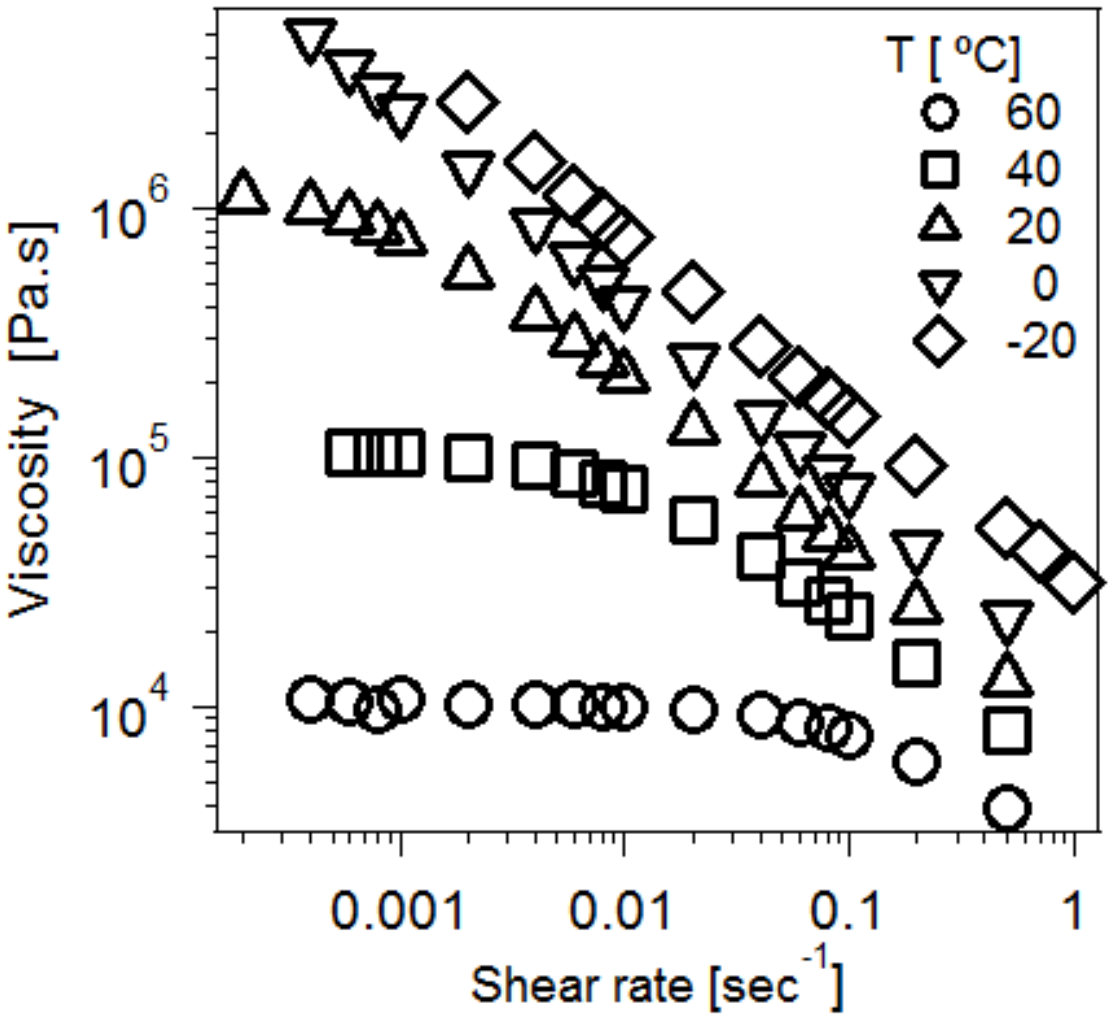

Figure 4.6 Viscosity vs. shear rate at different temperatures for sample with nanoparticle volume fraction of 5.4 %.

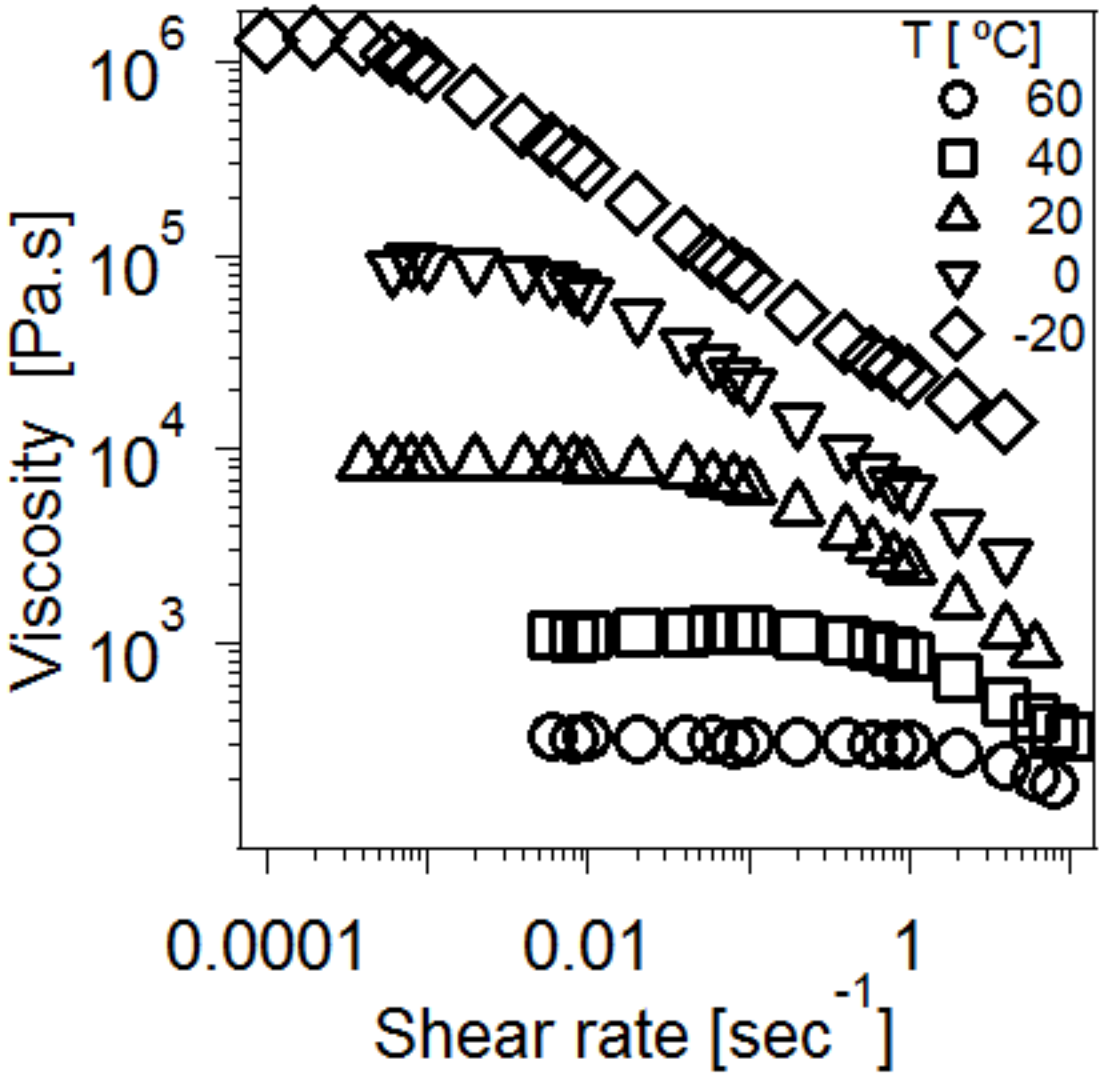

Figure 4.7 Viscosity vs. shear rate at different temperatures for sample with nanoparticle volume fraction of 4 %.

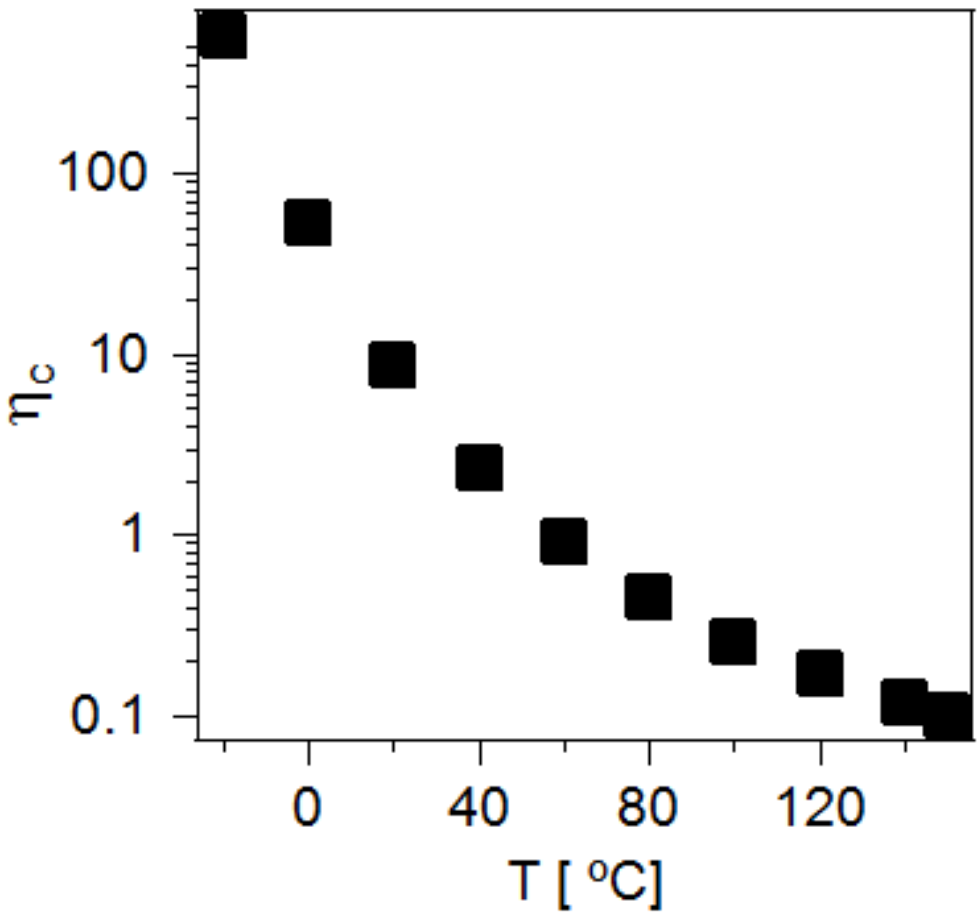

Figure 4.8 Viscosity of the untethered polymer as function of temperature.

compared to what we observe even for significantly low nanoparticle volume fractions studied here [26].

Figure 4.9 shows a typical dataset for the decay of the intensity correlation function g_2 with time, t, at multiple scattering wave vectors, q. Solid lines in the figure are fits with the stretched exponential form described by equation 4.1. XPCS measurements were carried out at multiple temperatures for all the samples mentioned above and intensity autocorrelations obtained at multiple temperatures and wave vectors were fitted to the stretched exponential forms for all data sets. Figures 4.10-4.13 show τ vs. q at different temperature for the samples with different nanoparticle volume fraction. It can be seen from the figures that the nanoparticle correlation time has very weak temperature dependence for 10 % and 8 % volume fraction samples, which is strikingly similar to the temperature dependence of the rheology of these samples. For 5.4 % and 4 % volume fraction samples, the correlation time decreases strongly with an increase in temperature. Notably, the correlation times obtained here are much larger than the predictions form the Stokes Einstein equation.

Figure 4.14 shows the comparison of the nanoparticle correlation times for all the samples at the corresponding q_{max} from figure 4.2. Figure 4.14 summarizes the data in figures 4.10-4.13, showing that τ is almost independent of temperature for 10 % and 8 % volume fraction samples, and shows a strong temperature dependence for 5.4 % and 4 % volume fraction samples at the length scales comparable to the interparticle spacing. These trends are very similar to the trends seen in the viscosity of the samples. Range of timescales probes in the rheology is comparable with the range of timescales that can be probed in a XPCS measurement. This similarity between

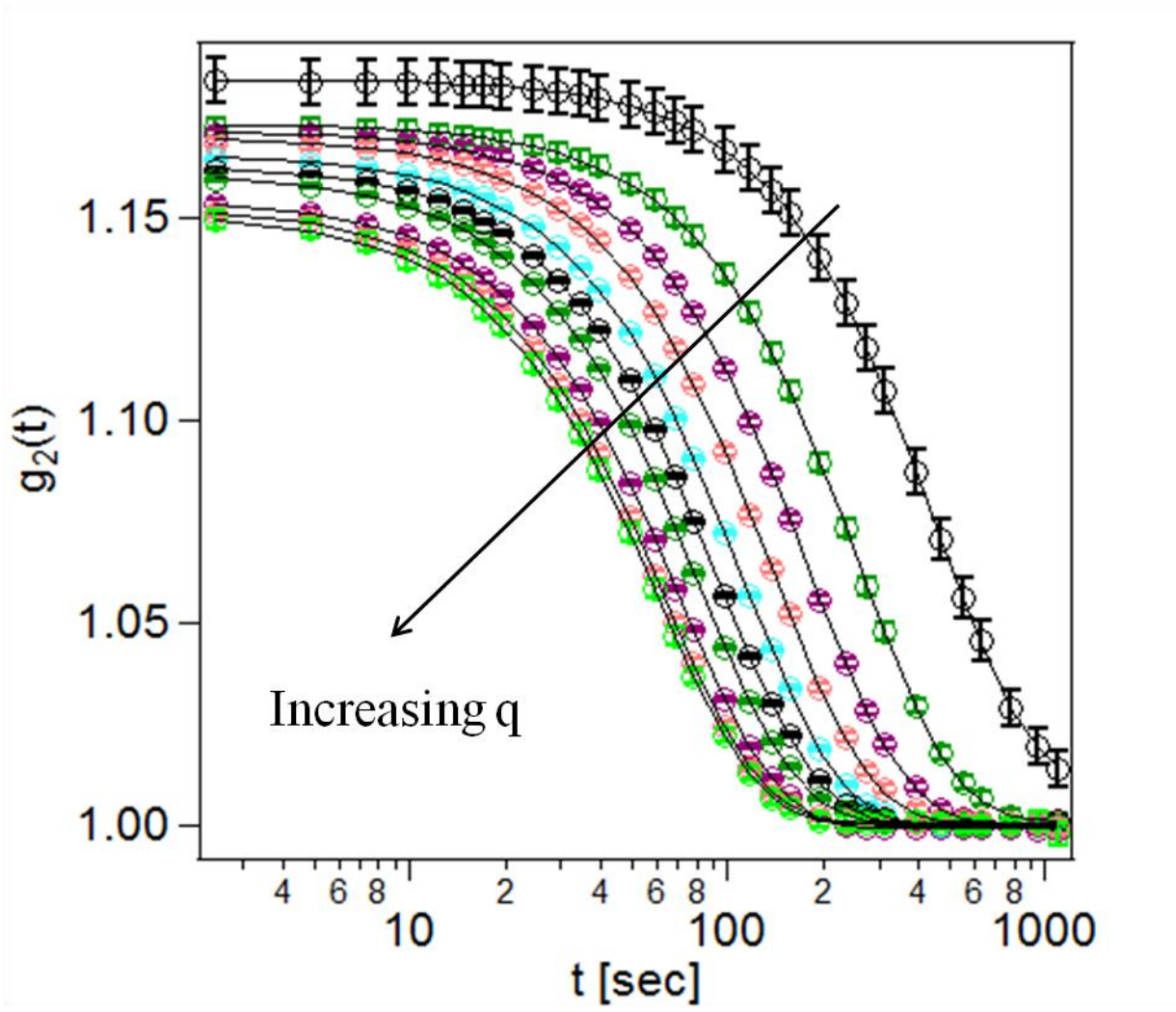

Figure 4.9 Typical decay of intensity autocorrelation function g_2 as function of time for multiple wave vectors, q. Nanoparticle volume fraction in the sample is 10 % and the temperature is 20 ˚C. Solid lines in the plot are fits from stretched exponential function described in the text.

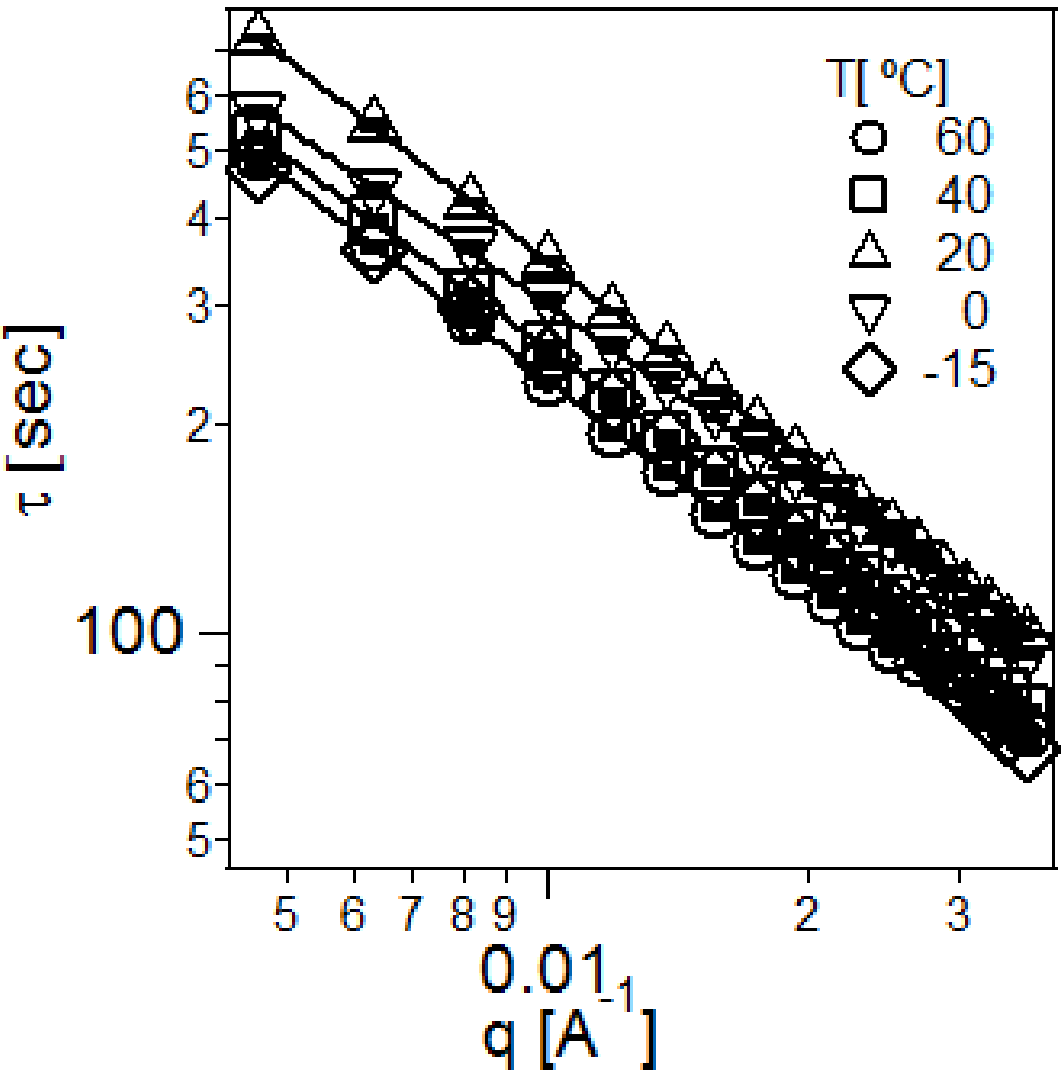

Figure 4.10 Correlation time, τ, vs. wave vector, q, obtained from the stretched exponential fits of the correlation function. Nanoparticle volume fraction for the sample is 10 %. Solid lines are fits with a power law.

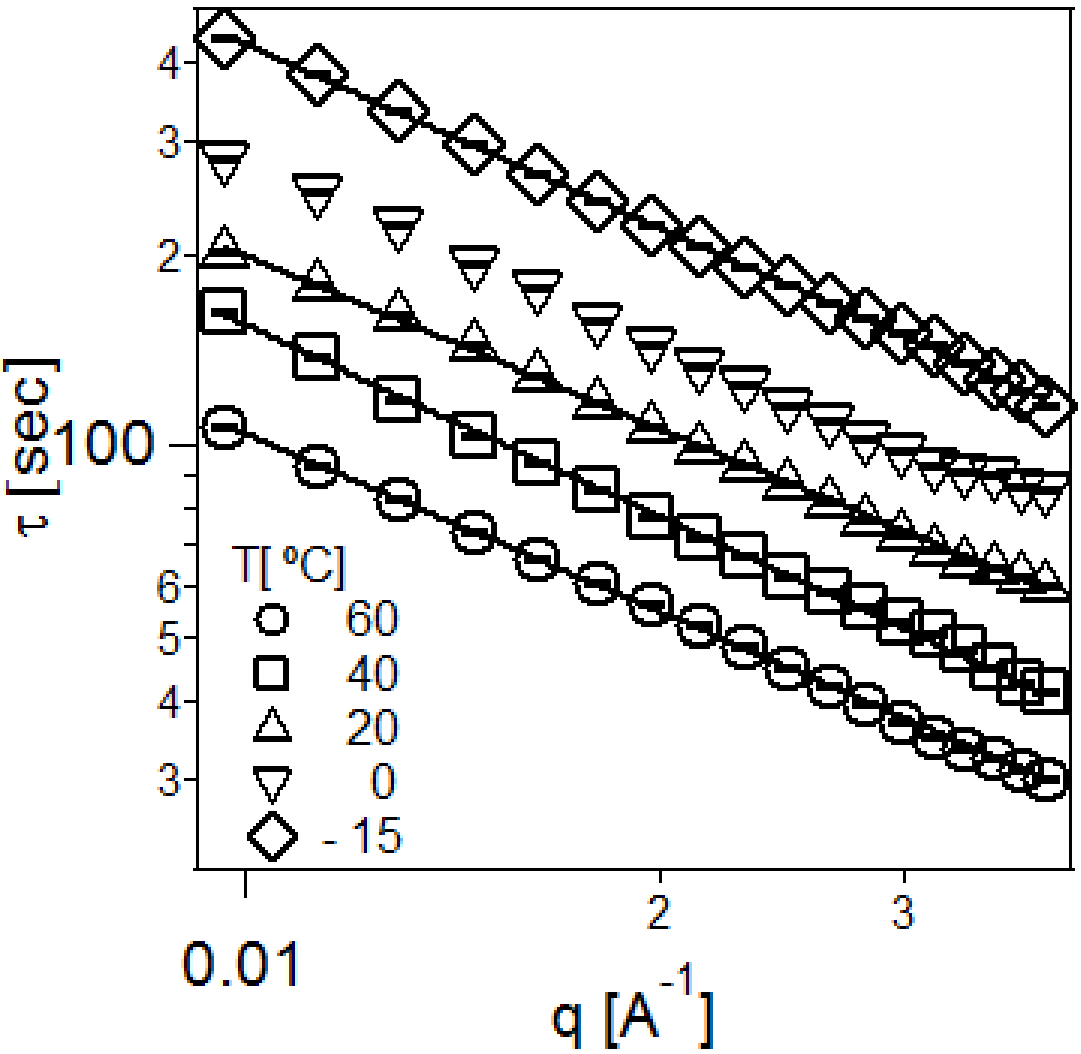

Figure 4.11 Correlation time, τ, vs. wave vector, q, obtained from the stretched exponential fits of the correlation function. Nanoparticle volume fraction for the sample is 8 %. Solid lines are fits with a power law.

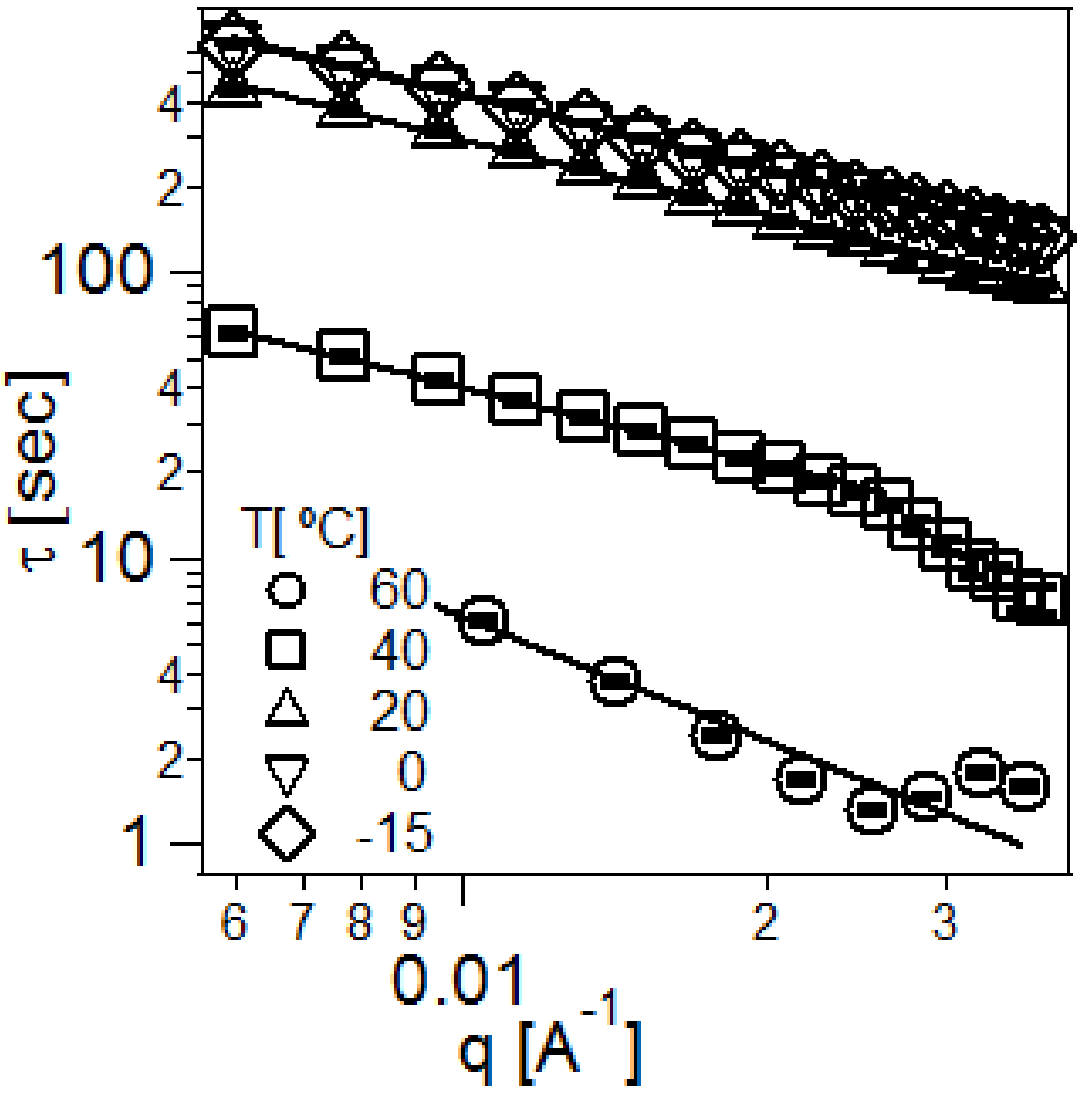

Figure 4.12 Correlation time, τ, vs. wave vector, q obtained from the stretched exponential fits of the correlation function. Nanoparticle volume fraction for the sample is 5.4 %. Solid lines are fits with a power law.

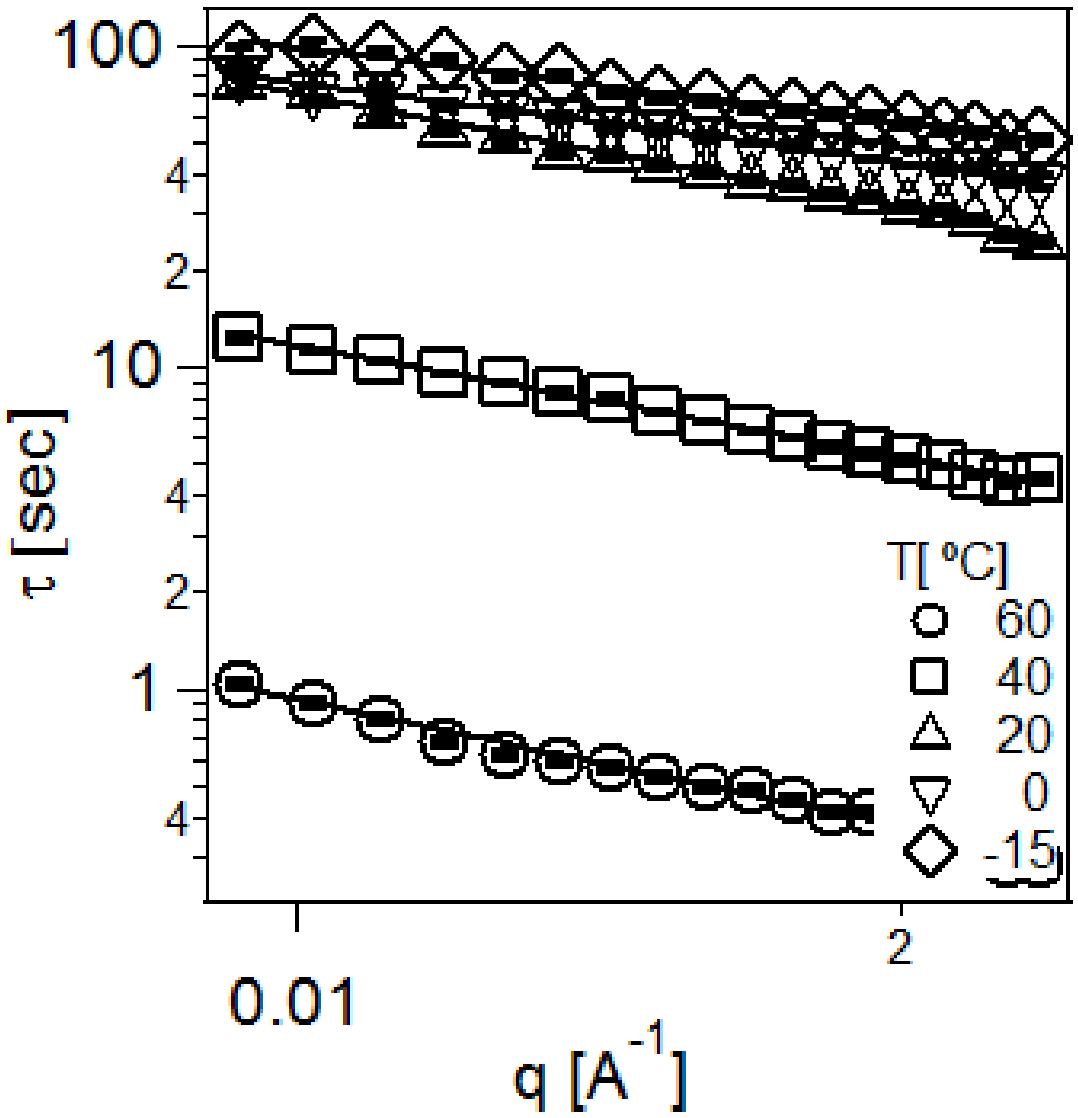

Figure 4.13 Correlation time, τ, vs. wave vector, q, obtained from the stretched exponential fits of the correlation function. Nanoparticle volume fraction for the sample is 4 %. Solid lines are fits with a power law.

the XPCS data and rheology indicates that the nanoparticle dynamics governs the rheology of these systems.

Figure 4.15 shows the β values obtained from the stretched exponential fits, showing that β is greater than 1 for all the samples. Wave vector dependence of τ can be fitted to a power law ($\tau \sim q^{-n}$) for all the cases as shown by the solid line in figures 4.10-4.13. Figure 4.16 shows the power law exponent, n, vs. temperature at multiple nanoparticle volume fractions. n is close to 1 for all the cases and shows very small variation with temperature or the nanoparticle volume fraction. Power law exponent of -1 combined with $\beta > 1$ has been typically observed for soft glassy materials and has been attributed to the hyperdiffusive particle dynamics present over very large length scales [27-33]. Such dependence has also been observed in the dynamic light scattering and diffusive wave spectroscopy measurements for a wide range of jammed systems [27-33].

Figure 4.16 indicates that irrespective of the variations in the particle correlation times with temperature and nanoparticle volume fraction, the nature of particle dynamics remains hyperdiffusive for all the cases. This observation is surprising, particularly for the samples where we even see a Newtonian plateau in the viscosity, implying that the system can relax to equilibrium over some range of time scales. We would like point out here that this is the first example to the best of our knowledge where hyperdiffusive dynamics has been observed for a Newtonian liquid. Typically most of the reports on hyperdiffusive dynamics involve jammed nonergodic systems [27-33]. Caronna et al. [31] reported the crossover from diffusive to hyperdiffusive dynamics in a dilute suspension of nanoparticles when the solvent was cooled

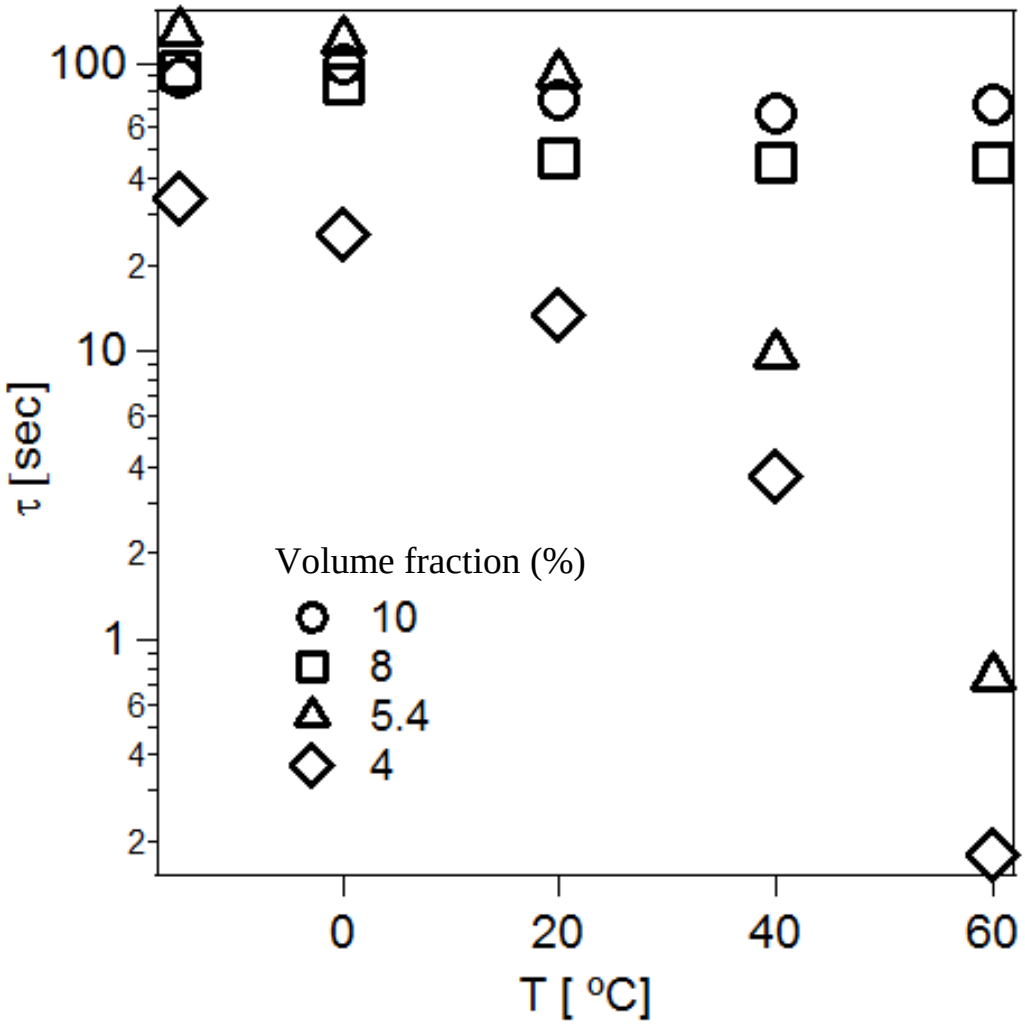

Figure 4.14 Correlation time vs. temperature for different samples at primary peak position of the structure factor q_{max}. 10 % and 8 % volume fraction samples show negligible change in the correlation time with temperature. 5.4 % and 4 % samples show decrease in the correlation time with increase in temperature.

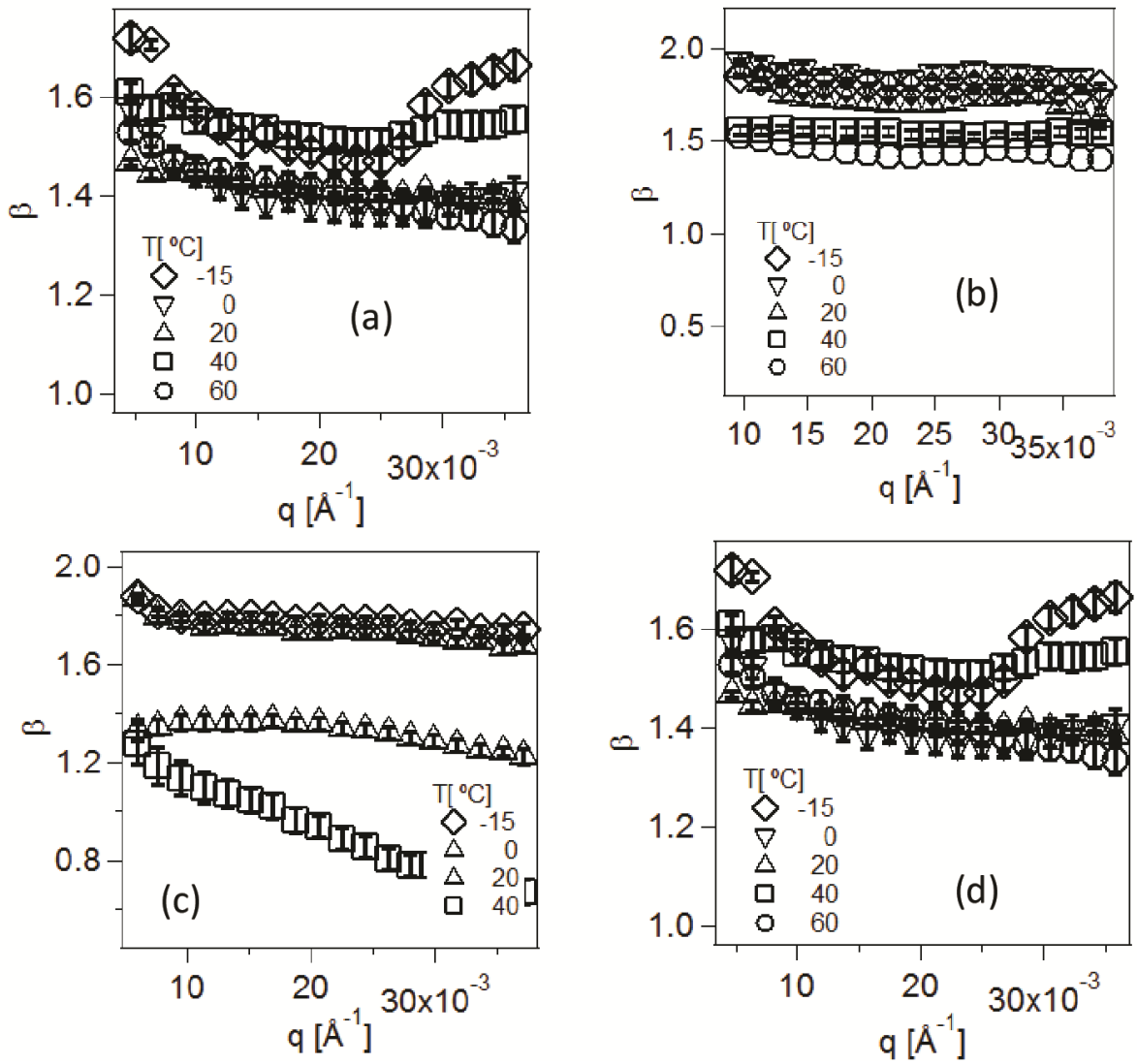

Figure 4.15 Stretching exponent, β, vs. wave vector, q, obtained from the stretched exponential fits of the correlation function. For nanoparticle volume fractions: (a) 10 %, (b) 8 %, (c) 5.4 %, (d) 4 %. β is greater than 1 for most of the data sets.

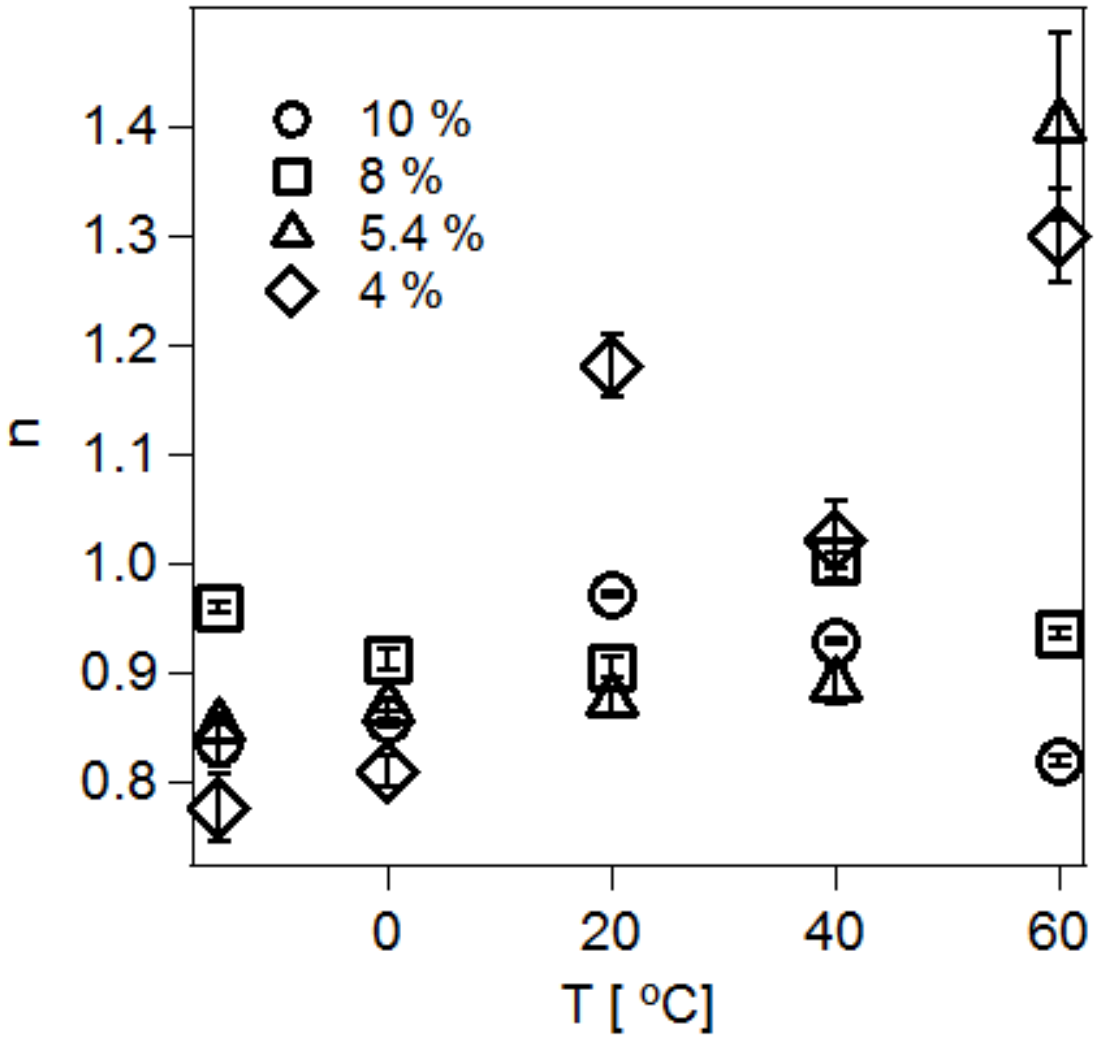

Figure 4.16 Power law exponent, *n*, obtained from the fits of τ vs. *q* data at multiple temperatures. *n* is close to 1 for all the cases, indicating the hyperdiffusive dynamics.

below the glass transition temperature, T_g. Contrastingly in our case hyperdiffusive dynamics is observed even when the tethered polymer is above its T_g.

The origin of hyperdiffusive dynamics is a source of speculation in the literature and many different hypotheses have been proposed till now. Cipeletti et al. [29] proposed that motion of a particle in a viscoelastic medium creates a force dipole, thus the displacement field from a particle decays faster than r^{-1}. They proposed a simple scaling argument that predicts the -1 scaling. Bouchaud and Pitard further improved this notion by incorporating a micro collapse time [27], and theoretically predicted the -1 scaling of τ vs. q. Later Cipeletti et al. [32] proposed that the hyperdiffusive dynamics results from the relaxation of the internal stress built into the material at the jamming transition. In another continuous time random walk approach, it was proposed that the particle motion is a highly discontinuous and happens due to sudden coordinated rearrangements [28].

Although hyperdiffusive dynamics has been observed widely for glassy systems, observation of hyperdiffusive dynamics for the samples that exhibit Newtonian viscosity is surprising for our case. This might be the case due to the fact that polymer relaxation cannot be complete in these systems without the nanoparticle rotation. Unlike a star polymer, where the new conformation of a polymer chain can be chosen randomly after a relaxation event, the new conformation of the polymer tethered to a nanoparticle surface is chosen from a restricted space in the absence of nanoparticle rotation. Particle rotation will he highly restricted in these systems due to the interpenetration of the polymer chains, hence particle rotation can place only by coordinated rearrangement events occurring over large length scales. These coordinated rearrangement events facilitate the particle rotation and give rise to hyperdiffusive dynamics even at low nanoparticle volume fraction.

Now we turn to the origin of the change in trends in the temperature dependent rheology and nanoparticle correlation time with changing the nanoparticle volume fraction. Temperature dependence of the polymer viscosity is typically understood by free volume theory. We have proposed a simple free volume argument to explain the observed temperature dependence of the viscosity. Doolittle's equation describes the free volume dependence of the viscosity as:

$$\eta \sim \exp\left(\frac{E}{f}\right) \qquad (4.2)$$

Where E is a constant and f is free volume. For the present system, total free volume will be the summation of contribution from nanoparticles and the tethered polymers

$$f = f_{polymer} + f_{particle} \qquad (4.3)$$

Free volume contribution from the polymer can be assumed to be linear with temperature, as typically is assumed for polymer melts

$$f_{polymer} = A(1-\varphi)(T - T_0) \qquad (4.4)$$

Free volume contribution from nanoparticles will decrease with increasing the temperature, as polymer chains have more entropic freedom to fill the interparticle space more uniformly at a higher temperature, hence

$$f_{particle} = \frac{B\varphi}{T - T_0} \qquad (4.5)$$

$$f = A(1-\varphi)(T - T_0) + \frac{B\varphi}{T - T_0} \qquad (4.6)$$

Here A and B are constants and T_0 is the glass transition temperature of the polymer. From this expression, first term will dominate at low nanoparticle volume fraction, giving a decreasing viscosity with increasing temperature, whereas at high nanoparticle volume fraction, second term will dominate, giving the observed temperature independent viscosity.

4.5 Conclusions

We have investigated the effect of changing nanoparticle volume fraction and temperature on the structure and dynamics of self-suspended fluids. We find that changing the temperature has no effect on the nanoparticle arrangement in the system. Effect of temperature change on the nanoparticle dynamics exhibits several interesting features where the nanoparticle dynamics becomes faster with increase in temperature at low nanoparticle volume fraction, whereas at moderately high nanoparticle volume fraction, nanoparticle dynamics is independent of temperature. Rheology measurements show strikingly similar results to the XPCS data, indicating that the rheology of these systems is primarily governed by the slow nanoparticle motion. Further, decreasing the nanoparticle volume fraction results in a faster nanoparticle dynamics and decrease in the viscosity of the system. For all of the materials studied here, the scaling exponent between τ and q was found to be close to -1 indicating slow and hyperdiffusive nanoparticle motion in these systems.

ACKNOWLEDGEMENTS

This work was supported by the National Science Foundation, Award No. DMR-1006323 and by Award No. KUS-C1-018-02, made by King Abdullah University of Science and Technology (KAUST). Facilities available though the Cornell Center for Materials Research (CCMR) were used for this study. We would like to acknowledge Suresh Narayanan at Argonne national

laboratory for his expert assistance with the XPCS measurements. We would also like to thank Wesly Burghardt at Northwestern University for providing his inputs. We would like to acknowledge Hsiu-Yu and Donald Koch at Cornell University for helpful discussions.

REFERENCES

1. M. E. Mackay et al., Science **311**, 1740 (2006).
2. A. Tuteja et al., Nano Lett. **5**, 1276 (2007).
3. M. E. Mackay, Nature Mater. **2**, 762 (2003).
4. P. Akcora et al., Nature Mater. **8**, 354 (2009).
5. M. McEwan, D. Green, Soft Matter **5**, 1705 (2009).
6. N. Dutta, D. Green, Langmuir **24,** 5260 (2008).
7. S. Srivastava, J. H. Shin, L. A. Archer, Soft Matter, DOI: 10.1039/C2SM06889C.
8. R. L. Lehney, Curr Opin Colloids Interface Sci, DOI: 10.1016/j.cocis.2011.11.002.
9. H. Guo, S. Ramakrishnan, J. L. Harden, R. L. Lehney, J. Chem. Phys **135**, 154903 (2011).
10. H. Guo, S. Ramakrishnan, J. L. Harden, R. L. Lehney, Phys. Rev. E **81**, 050401 (2011).
11. R. Bandopadhyay et al., Phys. Rev. Lett. **93**, 228302 (2004).
12. S. Chandran et al., J. Chem. Phys. **135**, 134901 (2011).
13. S. Srivastava et al., J. Chem. Phys. **133**, 151105 (2010).
14. B. Chung et al., Phys. Rev. Lett. **96**, 228301 (2006).
15. P. Agarwal, H. Qi, L. A. Archer, Nano Lett. **10**, 111 (2010).
16. P. Agarwal, L. A. Archer, Phys. Rev. E **83**, 041402, 2011.
17. P. Agarwal, S. Srivastava, L. A. Archer, Phys. Rev. Lett. **107**, 268302 (2011).
18. H. Y. Yu, D. L. Koch, Langmuir **26**, 16801 (2010).
19. S. K. Goyal, F. A. Escobedo, J. Chem. Phys. **135**, 184902 (2011).
20. R. P. Quirk, T. H. Cheong, T. Yoo, Macromol. Chem. Phys. **203**, 1178 (2002).
21. R. Rodriguez, R. A. Herrera, L. A. Archer, E. P. Giannelis, Adv. Mater. **20**, 4353 (2008).

22. A. Bergmann, G. Fritz, O. Glatter, J. Appl. Crystallogr. **33**, 1212 (2000).

23. G. B. Mckenna, T. Narita, F. Lequeux, J. Rheol. **53,** 489 (2009).

24. D. Lumma et al., Phys. Rev. E **62**, 8258 (2000).

25. A. Madsen et al., New J. Phys. **12**, 055001 (2010).

26. G. K. Batchelor, J. Fluid Mech. **83**, 97 (1977).

27. J. P. Bouchaud, E. Pitard, Eur. Phys. J. E **6**, 231 (2011).

28. A. Duri, L. Cipelletti, Europhys. Lett. **76**, 972 (2006).

29. L. Cipelletti, S. Manley, R. C. Ball, D. A. Weitz, Phys. Rev. Lett. **84**, 2275 (2000).

30. D. Orsi et al., Phys. Rev. E **85**, 011401 (2012).

31. C. Caronna, Y. Chushkin, A. Madsen, A. Cupane, Phys. Rev. Lett. **100**, 055702 (2008).

32. L. Cipelletti et al., Faraday Discuss. **123**, 237 (2003).

33. H. Guo et al., Phys. Rev. Lett. **102**, 075702 (2009).

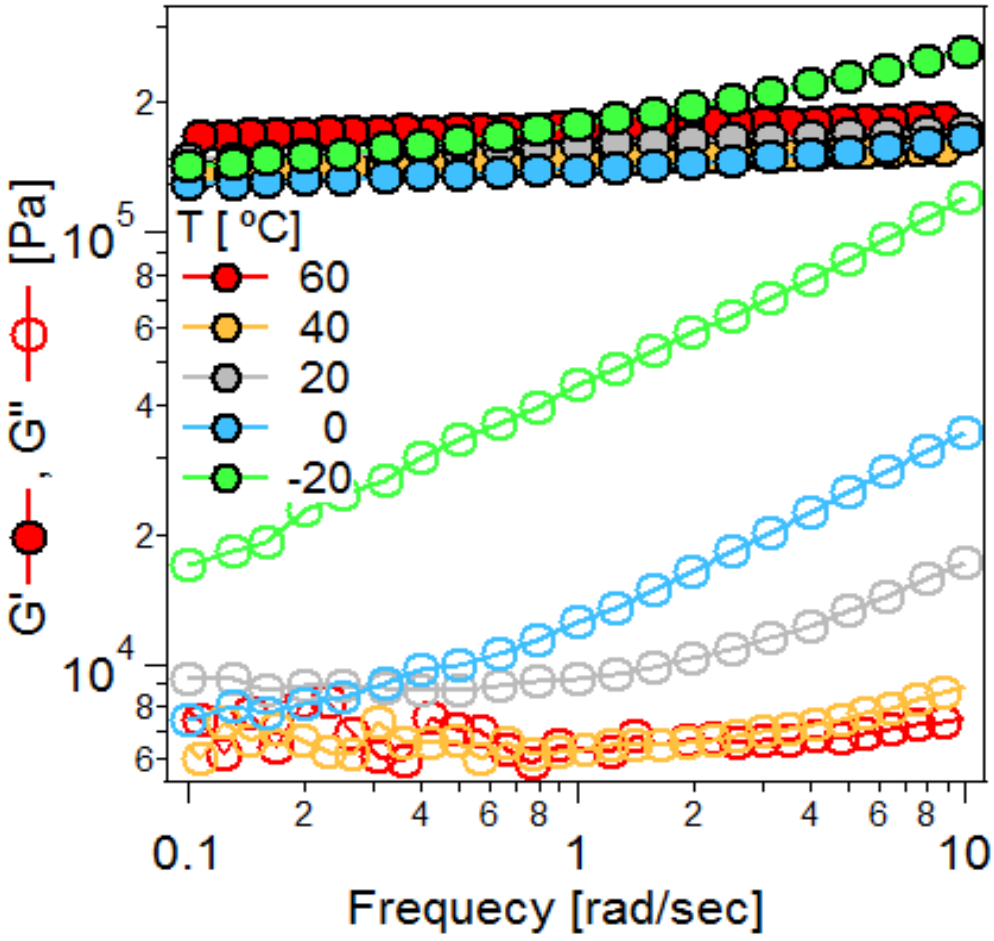

Supplementary figure 4.1 Storage modulus, *G'*, and loss modulus, *G"*, vs. frequency, ω, at different temperature for the sample with nanoparticle volume fraction φ = 10 %

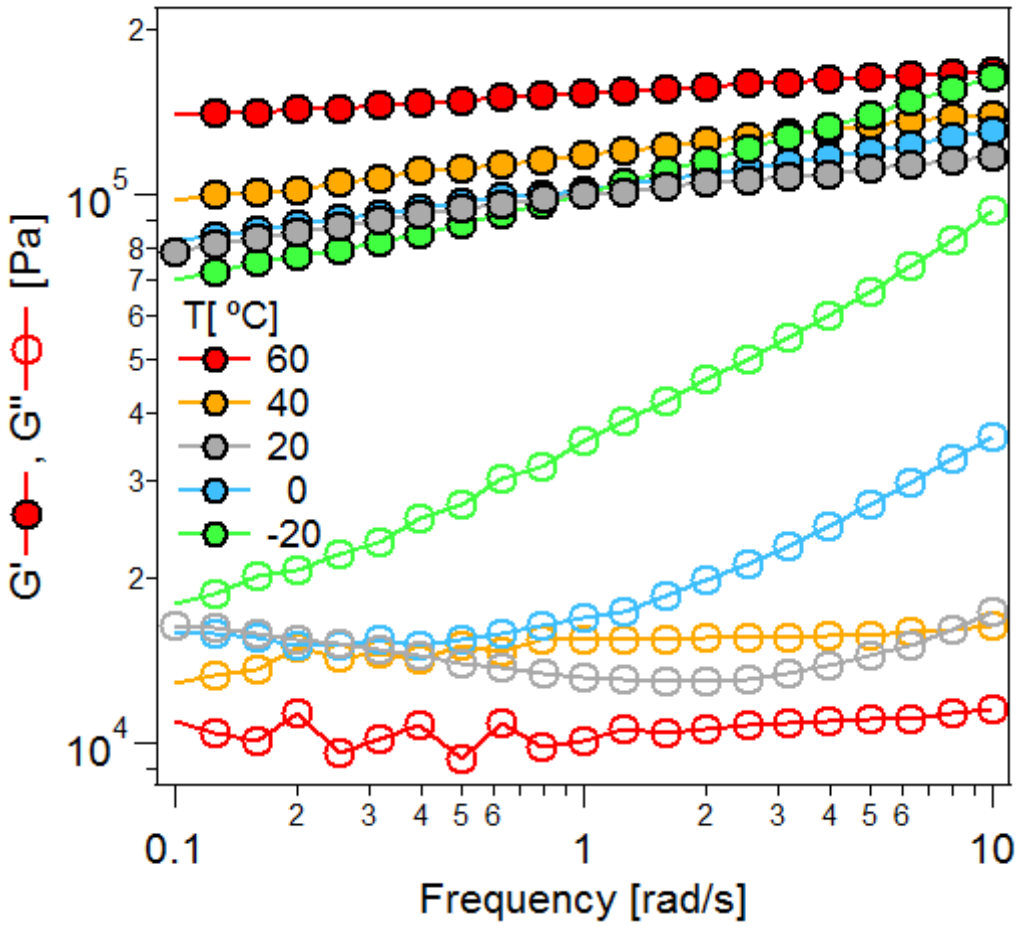

Supplementary figure 4.2 Storage modulus, *G'*, and loss modulus, *G"*, vs. frequency, ω, at different temperature for the sample with nanoparticle volume fraction φ = 8 %

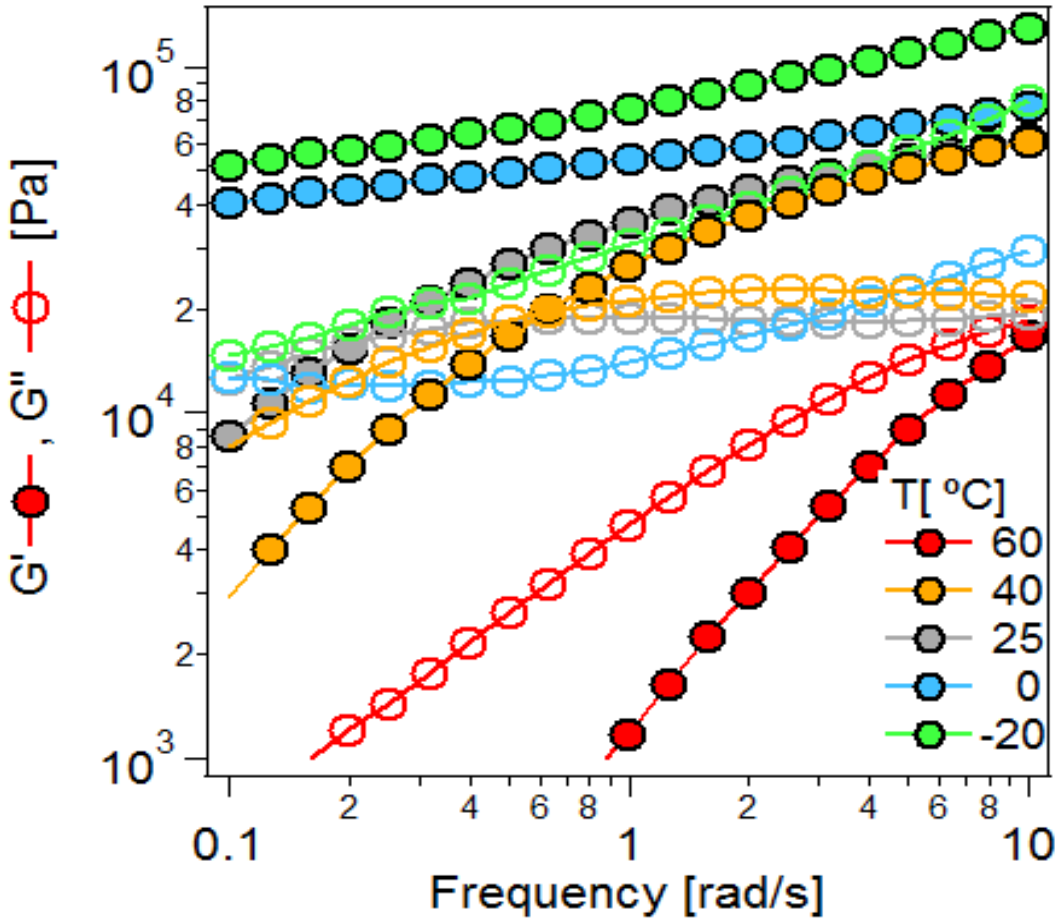

Supplementary figure 4.3 Storage modulus, *G'*, and loss modulus, *G"*, vs. frequency, ω, at different temperature for the sample with nanoparticle volume fraction φ = 5.4 %

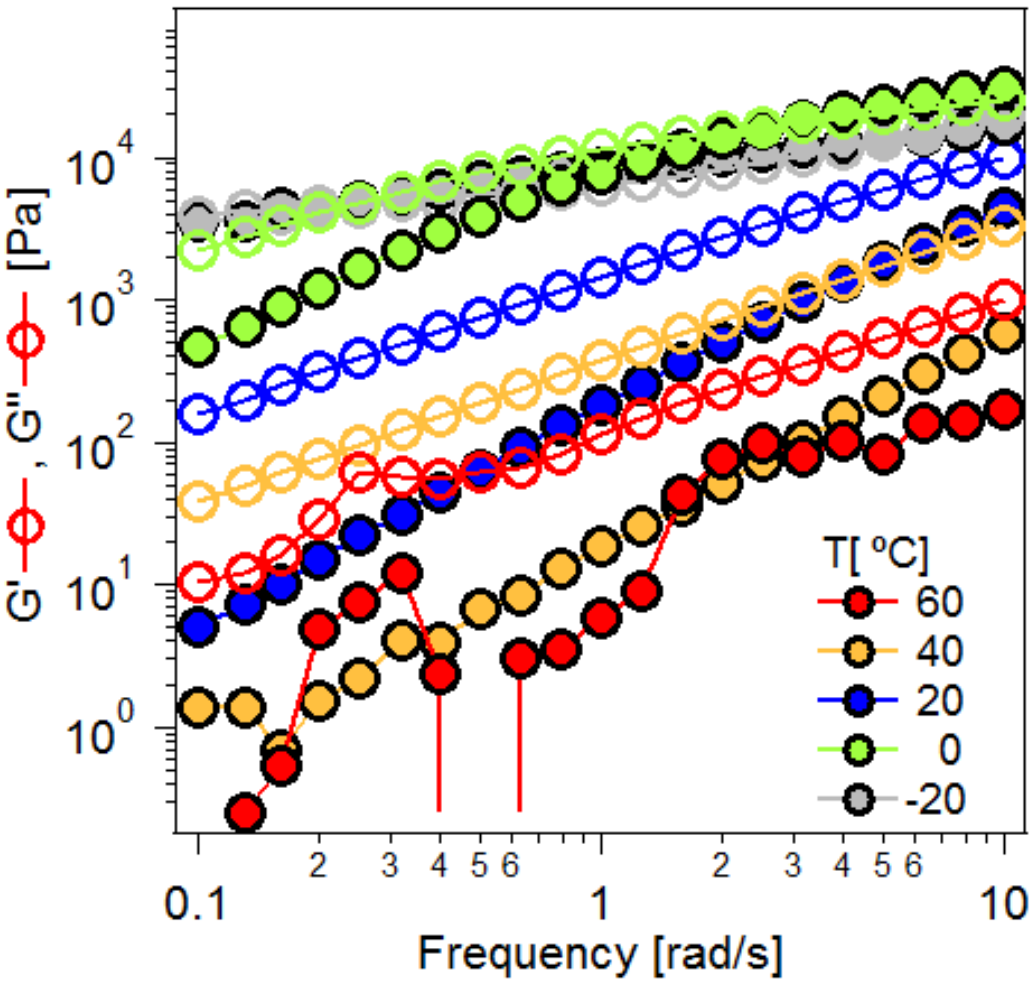

Supplementary figure 4.4 Storage modulus, *G'*, and loss modulus, *G''*, vs. frequency, ω, at different temperature for the sample with nanoparticle volume fraction φ = 4 %

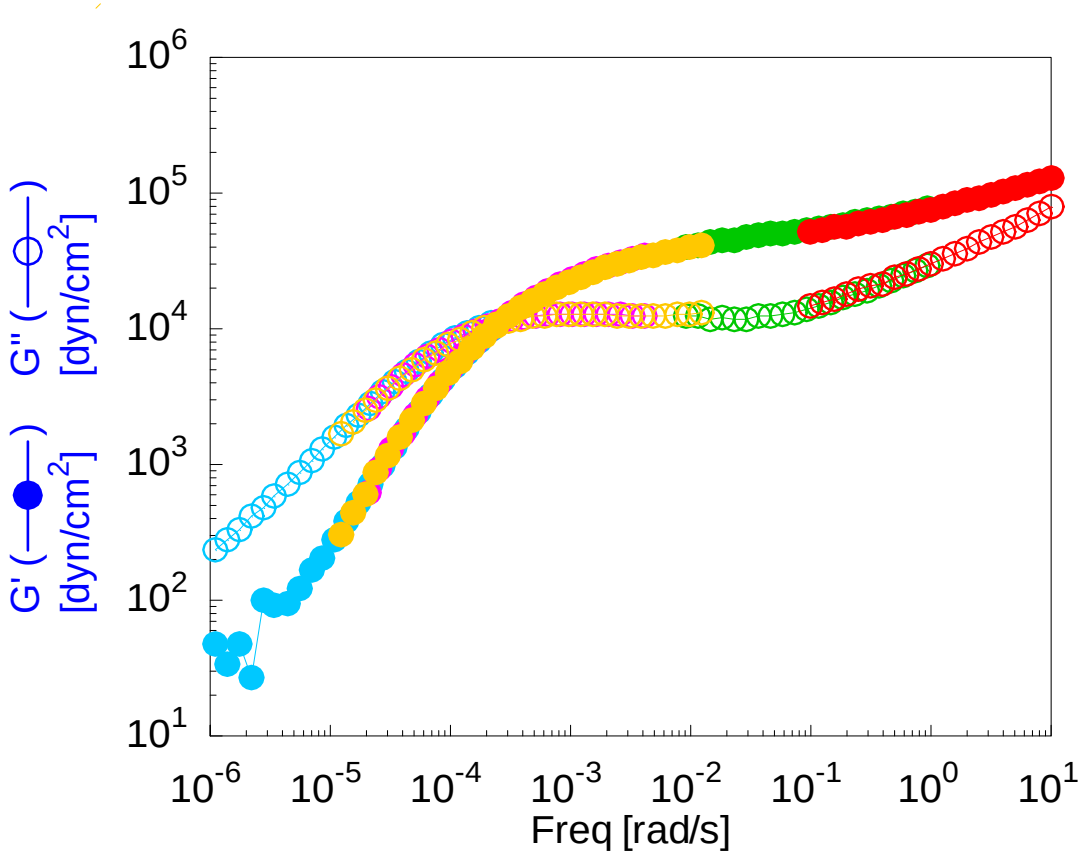

Supplementary figure 4.5 Time temperature superposition master curve for the sample with φ = 5.4 %.

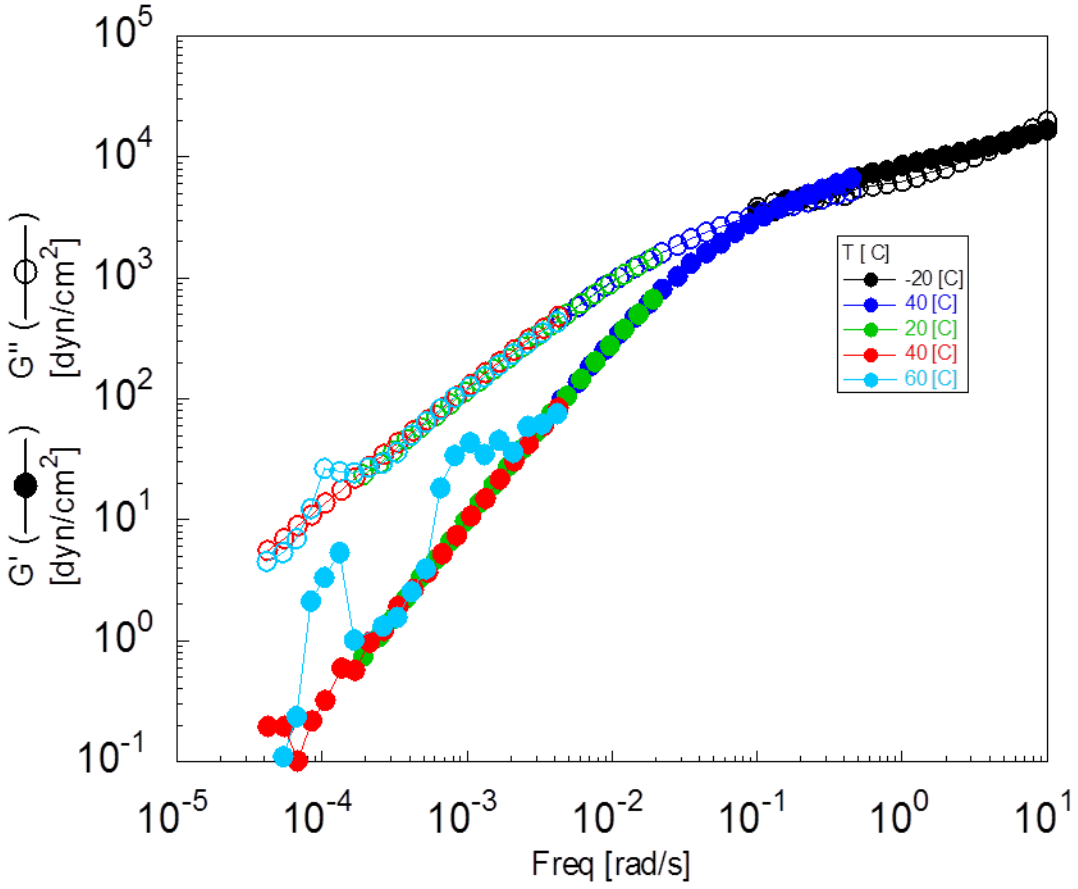

Supplementary figure 4.6 Time temperature superposition master curve for the sample with φ = 4 %.

CHAPTER 5

Thermal Jamming of a Colloidal Glass

Reproduced with permission from

Phys. Rev. Lett. 107, 268302 (2011)

P. Agarwal, S. Srivastava, L. A. Archer

5.1 Abstract

We investigate the effect of temperature on structure and dynamics of a colloidal glass created by tethering polymers to the surface of inorganic nanoparticles. Contrary to the conventional presumption, an increase in temperature slows down the glassy dynamics of the material, still causing no change in its static structure factor. We show that these findings can be explained within the soft glassy rheology (SGR) framework if the noise temperature, X, of the glass phase is correlated with thermodynamic temperature.

5. 2 Introduction

Jamming or glass transition has been observed in a wide range of soft materials including foams, emulsions, pastes, and suspensions when the fraction of the dispersed phase exceeds a critical value. Such ubiquity has led to attempts to develop a universal description of jamming, which has culminated in several phase diagrams for jammed matter [1, 2]. These phase diagrams identify density, load, and temperature as the key variables that control the thermodynamics of the jamming transition, and even the physical properties of the resultant soft glassy materials. The effect of density and load on the state of jammed matter has been studied experimentally by several groups, and the findings are in qualitative agreement with the proposed phase diagram; typically concluding that unjamming of a glass phase occurs with decreasing density [3, 4] or increasing load [5, 6].

In contrast, temperature, which plays a critical role in the equilibrium properties and dynamics of molecular systems, has received little systematic attention for colloidal glasses. This situation partially stems from the athermal nature of most granular systems. The common hypothesis hitherto has been that an increase in temperature will give rise to more fluidity and hence unjam

the system, as proposed in previous jamming phase diagrams [1, 2]. Here we perform such a systematic study using self-suspended nanoparticles densely grafted with polymer chains as a model soft glassy material [7, 8]. The absence of a solvent in the self-suspended nanoparticles studied here is attractive because it precludes any temperature dependent enthalpic interactions between the solvent and the suspended phase. Our studies show that contrary to expectations, increasing temperature enhances jamming, and that subsequent lowering of the temperature unjams the system. We further show that the effect is captured on the continuum level through coupling of the so-called noise temperature X [9] emanating from co-operativity of elements in a soft glass with the thermodynamic temperature T originating from interactions of the system with its surroundings. The fundamental origin of the coupling between X and T appears to be that higher temperatures lead to greater interpenetration of polymer brushes tethered to neighboring particles.

The limited utility of hard sphere colloids for exploring the physics of the glass transition and the phase space of jammed systems has been noted to result from their fragile behavior [10]. This has led to the growing interest in soft colloids as models for exploring soft glasses, which are typically polymer grafted nanoparticles or crosslinked microgels, [10-13]. A plethora of interesting physics has been unraveled though the study of such soft colloids, ranging from asymmetric caging [11], molecular glass-like fragility [10], reversible thermal gelation [12], and polymer mediated melting [13].

5.3 Results and Discussion

Experiments reported in this letter were carried out using a self-suspended suspension comprised of 10 ± 2 nm silica nanoparticles densely grafted (grafting density ≈ 1.5 chains/nm^2) with a

polyisoprene corona of molecular weight 5000 and polydispersity index M_w/M_n of 1.05. The volume fraction of the silica nanoparticles is 10 %. Mechanical rheometry in oscillatory- and transient shear flow, using an Anton Paar MCR 501 rheometer equipped with cone and plate fixture, was used to characterize the flow behavior of the material. All measurements were performed at temperatures above the glass transition temperature of polyisoprene and samples were presheared to erase any shear history, with the waiting time after the preshearing kept long compared to the measurement time to ensure that the measurements are not affected by aging [14].

The characteristic response of a soft glass subjected to oscillatory shear flow with varying strain amplitude, γ, is illustrated in the inset of figure 5.1 [4, 7, 9, 15]. At least three distinct flow regimes are observed: (i) a strain independent linear viscoelastic regime at low shear strains, wherein the storage modulus (G') dominates the loss modulus (G''); (ii) a nonlinear viscoelastic regime at intermediate shear strains, in which G'' increases due to breaking of cages; and (iii) a strain softening liquid regime at high strains, wherein $G'' > G'$ and both moduli are decreasing functions of the shear strain. The telltale maximum observed in $G''(\gamma)$ is a unique feature of jammed materials, such as soft glasses, and is not observed for polymers and other viscoelastic materials. The size of the loss maximum relative to its linear response value is therefore an indicative of the degree of jamming in the system.

Effect of temperature on $G''(\gamma)$ is shown in Figure 5.1. The figure shows an increase in the relative size of the loss maximum as temperature is increased; implying that a higher temperature leads to enhanced jamming in the system. Figure 5.2 shows the corresponding loss tangent, $\tan\delta(\gamma) \equiv G''(\gamma)/G'(\gamma)$ at different temperatures. It is apparent that in the linear regime, the

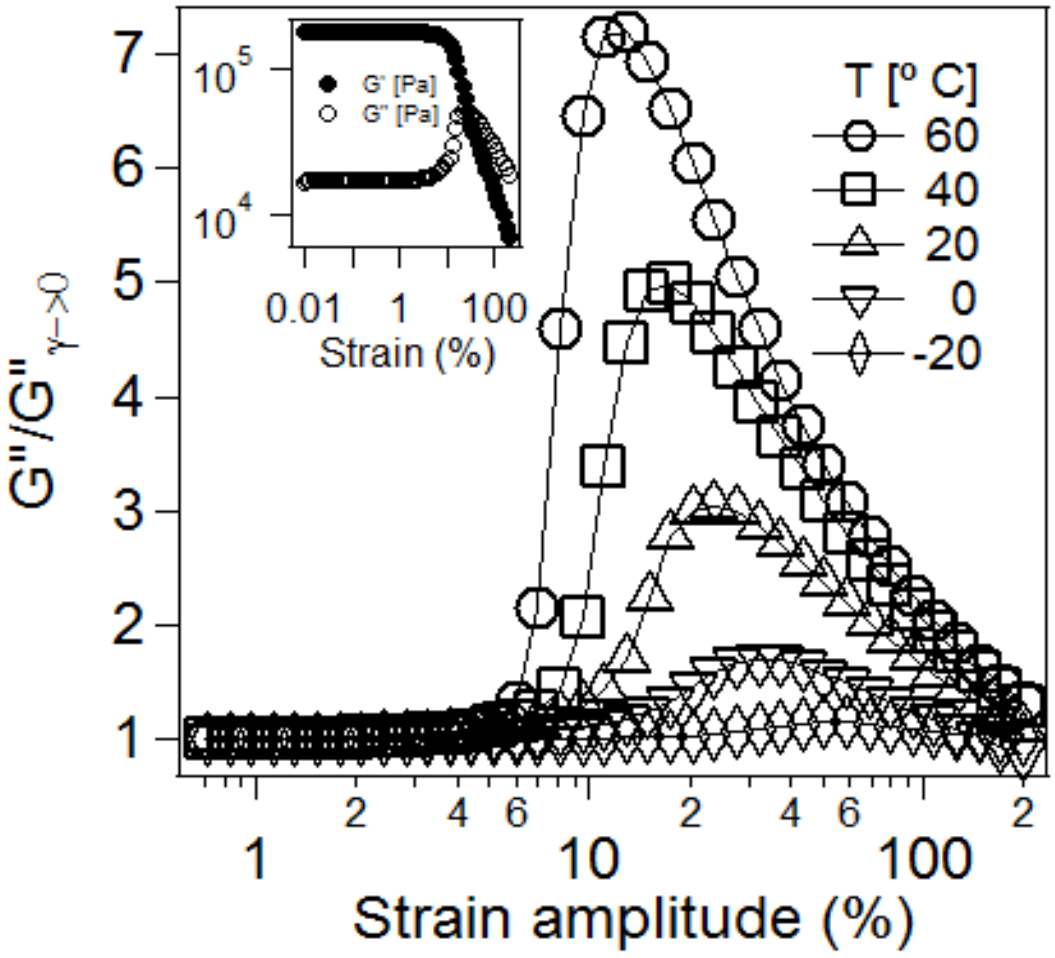

Figure 5.1 Oscillatory amplitude sweep results at different temperatures at an angular frequency of ω = 10 rad/s: symbols represent *G"* normalized by its linear response value and lines are guide to the eye. Relative height of the maxima in *G"* increases with an increase in the temperature, implying more jamming at a higher temperature. Inset shows typical behavior of *G'* and *G"* vs. strain amplitude, where an increase in *G"* is observed, followed by a crossover between *G'* and *G"*.

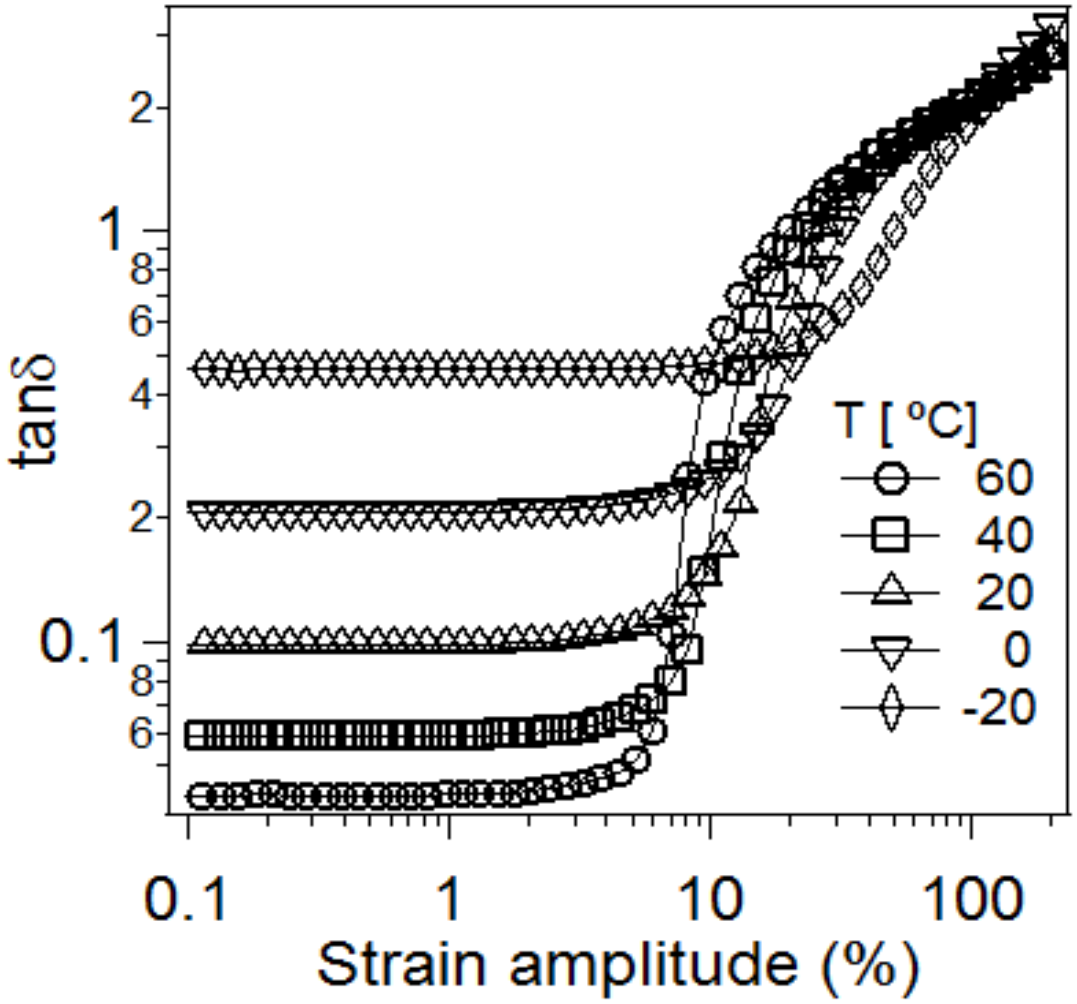

Figure 5.2 *tanδ* vs. stain amplitude for the data in figure 5.1: linear value of *tanδ* decreases with an increase in temperature implying a more solid like response at a higher temperature. Waiting time of 5000 s was allowed after the preshearing for the measurements at every temperature.

material becomes more solid-like (lower $tan\delta$) or more jammed as its temperature is increased. As illustrated in supplementary figures 5.1-5.4, these effects are observed over a wide range of shear frequencies and waiting times, ruling out temperature-dependent aging as the governing mechanism [16, 17]. Additionally, as illustrated in supplementary figure 5.5, the effect of temperature change is completely reversible. To investigate the effect of temperature on the interparticle structure, we have performed small angle X-ray scattering (SAXS) measurements on the materials over the same range of temperatures investigated in the rheological studies. These experiments were carried out using an Anton Paar SAXSess instrument with a line collimation setting using Cu K-α radiation with a wavelength of .1542 nm. As shown in figure 5.3, neither the *q*-dependent scattered intensity, nor the interparticle structure factor (figure 5.4) extracted from the intensity curves change in a systematic way with temperature. These results exclude the possibility that the temperature dependent rheology is originating from the change in interparticle spacing occurring due to change in temperature, hence implying that the thermal jamming is originating from the polymers.

Invariability of the interparticle structure with temperature points towards thermally induced changes in the conformation of tethered polymer chains as a possible mechanism for our observations. While such changes do not alter the interparticle separation, they might lead to enhanced corona penetration (figure 5.5) and hence increased jamming. Interestingly, this explanation does not comport with Flory's famous argument [18], which states that untethered polymer chains in a melt should behave like ideal chains, wherein all the interactions and hence the chain conformations are independent of temperature. However, the reversibility of the observed thermal jamming phenomena, the absence of a dependence on deformation rate or waiting time, and the lack of commensurate changes in the interparticle structure factor suggest

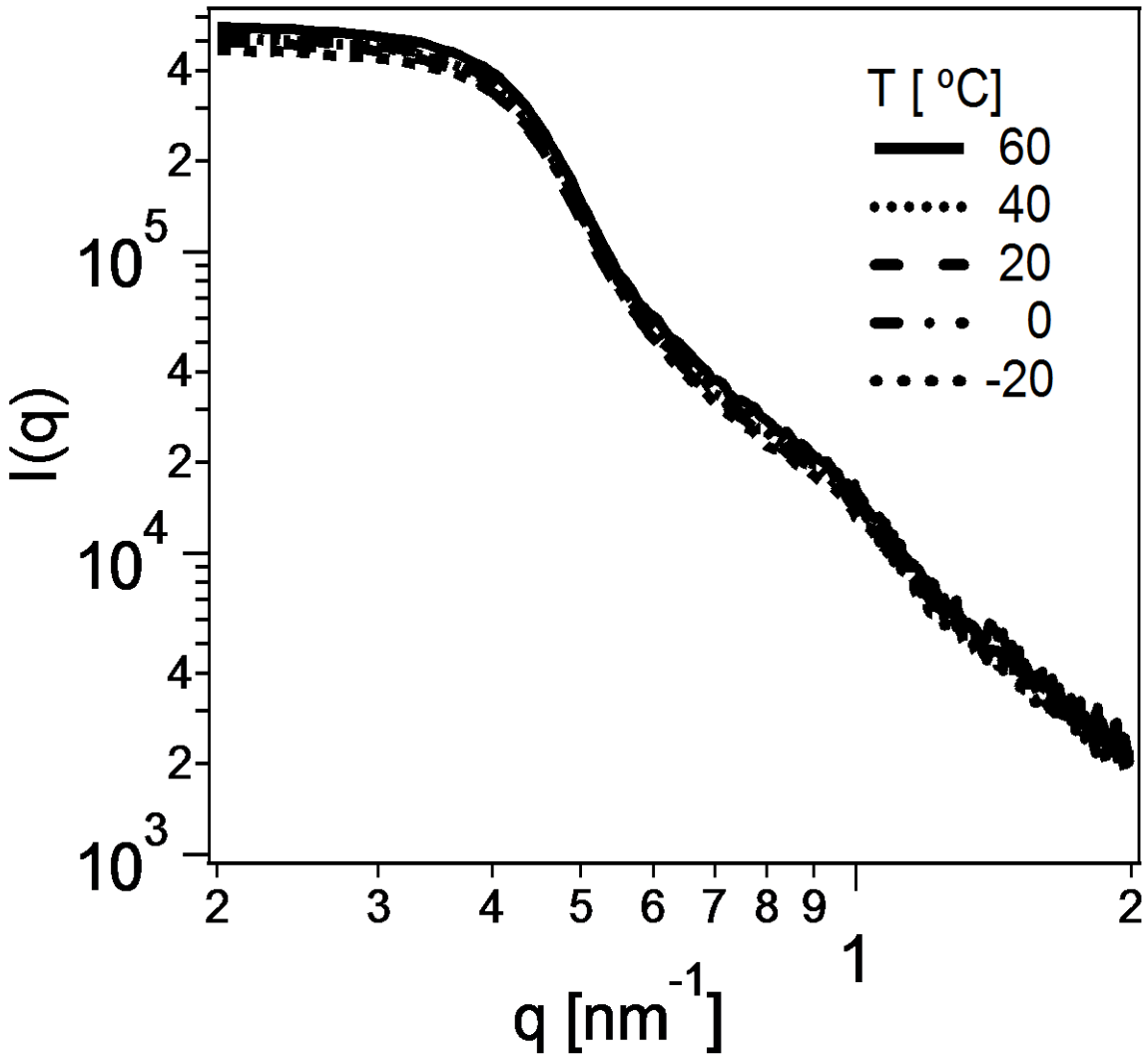

Figure 5.3 Intensity, *I(q)* vs. wave vector, *q*, obtained from small angle x-ray scattering, showing no noticeable change in the scattering pattern with a change in temperature

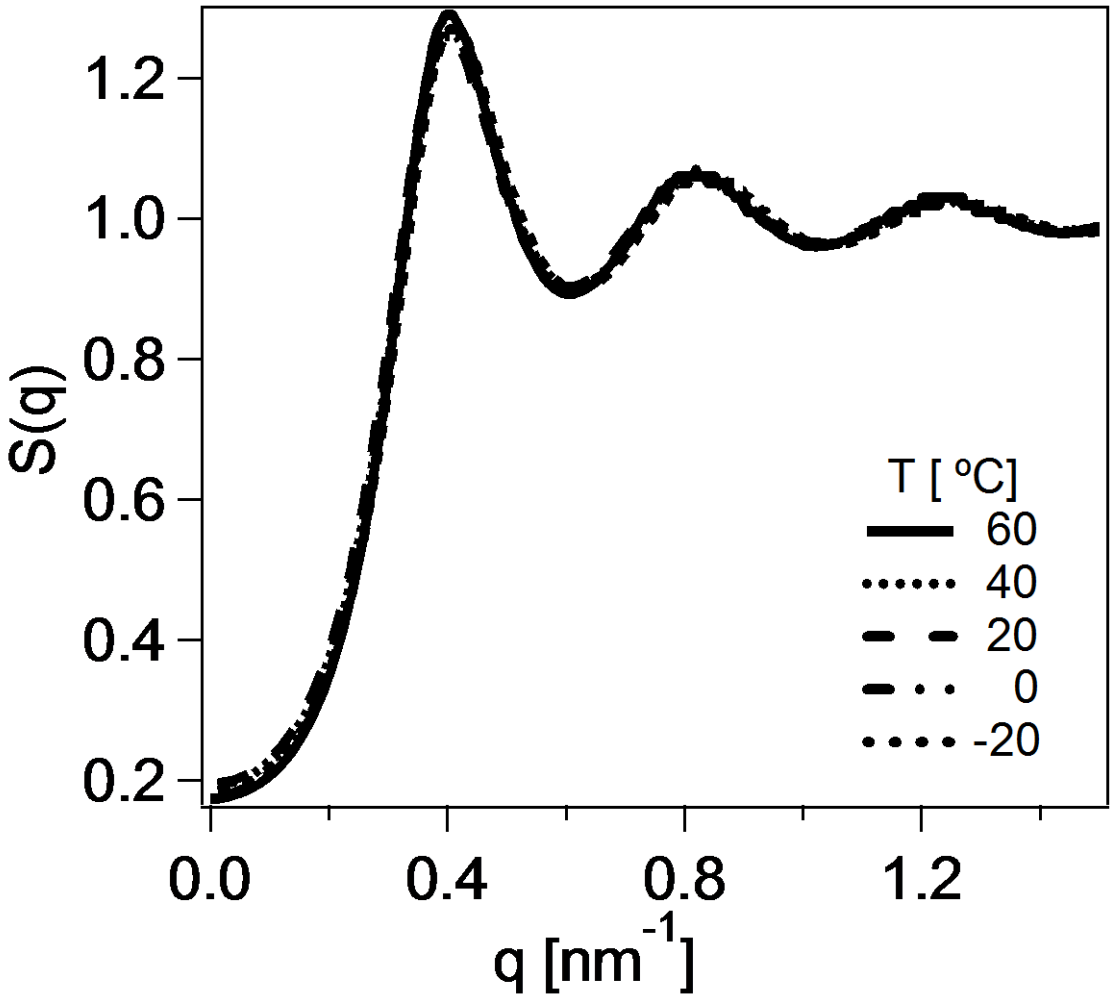

Figure 5.4 Structure factor, *S(q)*, vs. *q* obtained from the *I(q)* vs. *q* data, also showing no evident change in the *S(q)* with a change in temperature.

that the changes that produce thermal jamming must be quite local and reversible, in agreement with the mechanism proposed in figure 5.5.

The Soft glassy rheology (SGR) model proposed by Sollich and coworkers [9] is a widely accepted framework for theoretically predicting the rheology of soft glassy materials. In this model, a soft glass is assumed to be composed of elements which are trapped in the cages formed by their neighbors, wherein each element sees an energy landscape of multiple well depth to which it can hop. A key parameter in this model is the so-called noise temperature, *X*, which reflects cooperativity in the system and is indicative of the energy available for hopping out of a potential energy well in the energy landscape. *X* can thus be considered as the colloidal analog of temperature in molecular systems [9]. *X* can be related to the phase lag, δ between strain and stress by (see Appendix):

$$X = 1 + \frac{2}{\pi}\delta \qquad (5.1)$$

Figure 5.6 reports the noise temperature *X* derived from the *tan*δ vs. temperature data in figure 5.2. It is apparent from the figure that *X* decreases with an increase in temperature. This implies that lesser energy is available for hopping at higher temperature, supporting the aforementioned trends in figure 5.1. To the best of our knowledge, this is the first instance where *X* has been shown to be influenced by the thermodynamic, or measurement temperature of a glassy material. Our observation also provides a complementary method (to the widely accepted route of varying the volume fraction of particles in the suspension), for changing *X* in a colloidal suspension.

To verify the generality of our observations, we carried out similar experiments using self-suspended nanoparticles decorated with polymers of two other chemistries: polyethylene glycol

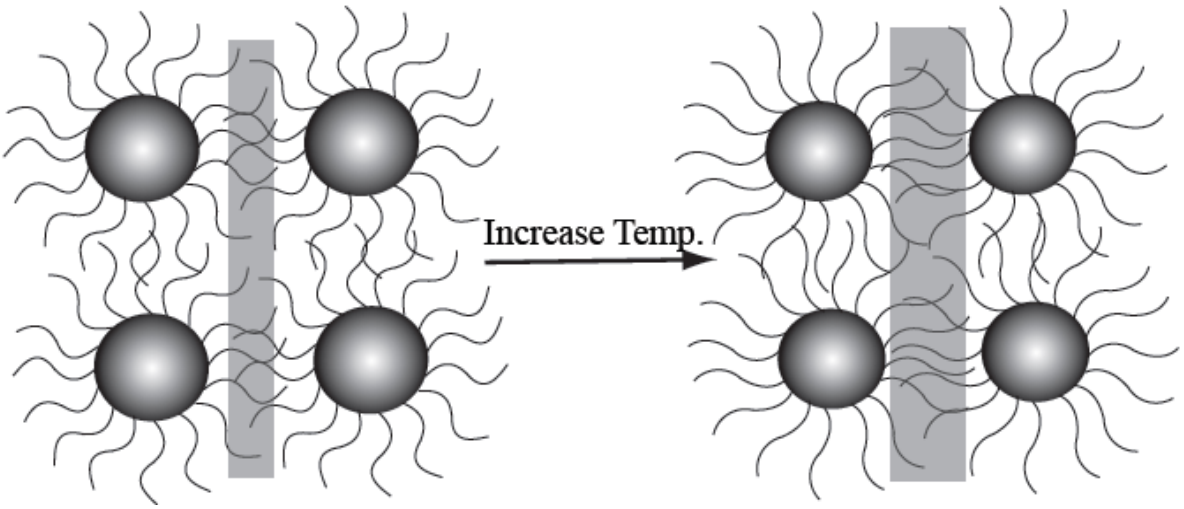

Figure 5.5 Schematic representation of the molecular process tentatively proposed to explain our observation of enhanced jamming at higher temperature. At higher temperature, tethered polymer chains experience a stronger driving force to uniformly fill the interparticle space, which enhances the excluded volume. For a fixed interparticle spacing, chains must therefore interpenetrate more, enhancing jamming of the particles.

(PEG) and polystyrene (PS). As illustrated in supplementary figures 5.8 – 5.10, the behavior is qualitatively identical to observations for the polyisoprene-based material in figure 5.1. The inset in figure 5.6 compares the temperature-dependent *X* values obtained for materials with very different chemistries. It is apparent from the figure that for all systems studied, *X* decreases with increase in temperature. Markedly, *X* vs. *T* data for all different materials can be fitted to Vogel-Fulcher-Tamman (VFT) [19] dependence:

$$X = Aexp\left(\frac{B}{T - T^*}\right) \qquad (5.2)$$

The parameters *A*, *B* and T^* are, respectively, the high temperature value of *X*, the activation energy, and Vogel temperature. Table 5.1 contains the VFT fit parameter values for the data for different samples shown in the inset of figure 5.6. For all the cases, value of *A* close to 1 indicating that the colloidal glass transition is approached at high temperature. The value of T^* is close to the glass transition temperature for polyisoprene and polystyrene and melting temperature for PEG, indicating that the tethered polymer chains play a critical role in the observed temperature dependence of *X*. Interestingly, the curvature of the *X* vs. *T* plot is reminiscent of that obtained by plotting dynamic properties, such as viscosity, against temperature in fragile glass forming liquids [10, 19].

To examine the SGR model predictions under similar conditions, we performed numerical simulations of SGR model at multiple noise temperature *X*. Specifically, the constitutive equation (5.3) proposed by Sollich et al. [9] has been solved numerically for the flow startup case after the application of a constant steady shear rate,

$$\sigma(t) = \gamma(t)G_0\left(Z(t,0)\right) - \int_0^t dt' \, \Gamma\left(t'\right)\gamma\left(t'\right)G_\rho\left(Z\left(t,t'\right)\right) \qquad (5.3)$$

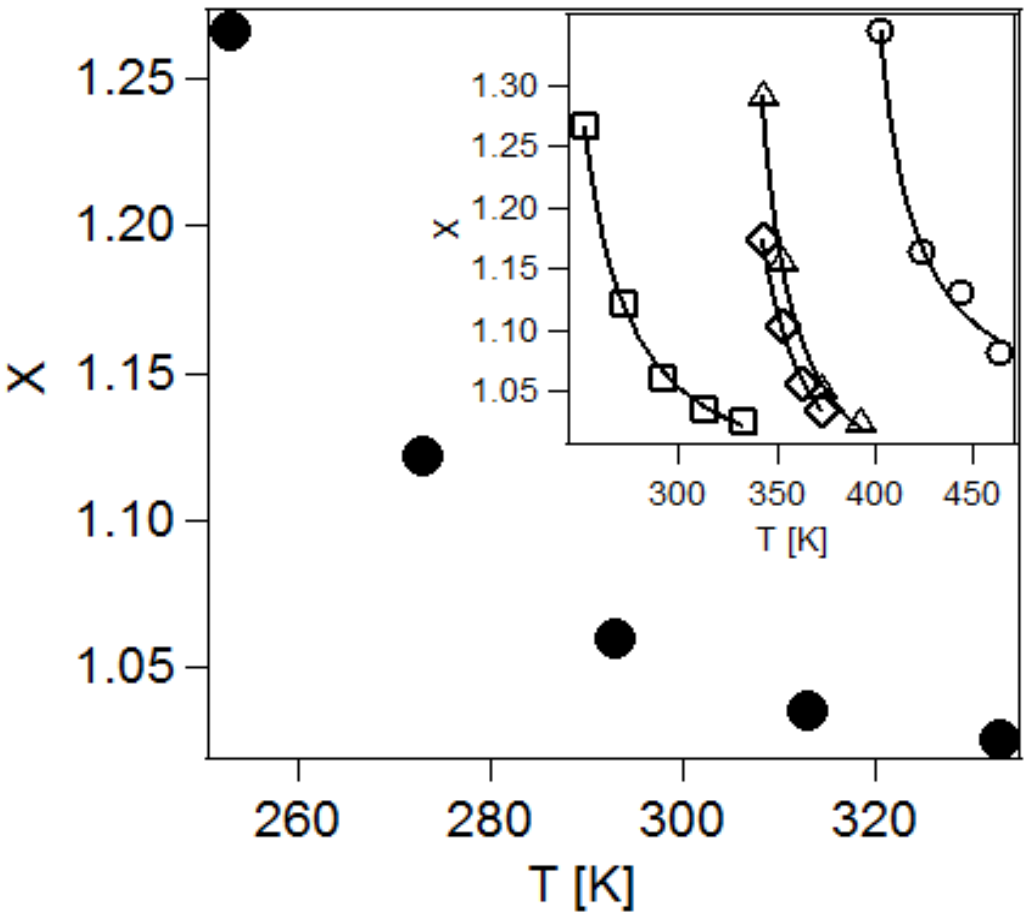

Figure 5.6 Noise temperature, *X*, as a function of temperature, obtained from the linear value of *tanδ* in figure 5.2. *X* decreases with an increase in the temperature, implying that lesser energy is available for hopping between the potential energy wells at a higher temperature. Inset shows the *X* vs. *T* plot for various materials encompassing different corona chemistry and molecular weights. Different symbols are, squares: 5000 M_w poyisoprene, diamonds: 2000 M_w polyethylene glycol (PEG), triangles: 5000 M_w PEG, circles: 3500 M_w polystyrene corona. Solid lines in the inset are fit with the VFT equation described in the text, fit parameters are provided in table 5.1.

Table 5.1 Value of the fit parameters for the VFT fits in the inset of figure 5.6

Corona type-M_w	***A***	***B***	T^*
Polyisoprene-5000	.95	7.2	227
Polyethylene glycol-2000	.91	7.2	314
Polyethylene glycol-5000	.93	5.9	324
Polystyrene-3500	1.01	5.7	382

Where the hopping rate, *Γ(t)* is obtained from solving the integral equation

$$1 = G_0\big(Z(t,0)\big) + \int_0^t dt'\Gamma(t')G_\rho\big(Z(t,t')\big) \qquad (5.4)$$

Here *σ(t)* is stress, *γ(t)* is strain, *Γ(t)* is the hopping rate, $G_0(z)(= \int dE\, P_0(E)\exp(-z\exp(-E/x)))$ and $G_\rho(z)(= \int dE\, \rho(E)\exp(-z\exp(-E/x)))$ are the surviving probabilities, $Z(t,t')(= \int dt"\exp[(\gamma(t") - \gamma(t')]^2/2x)$ is the effective time and $\rho(E)(= \exp(-E))$ is the probability distribution function for the yield energies. A more detailed discussion of the equations and involved parameters can be found in ref. [9].

As predicted by Sollich [9] and also observed experimentally [14, 15] the shear stress in a flow start-up experiment goes through an overshoot before reaching its steady-state value. Although the origin of the overshoot is not clearly understood, it is believed to reflect the breaking of cages in a jammed system. Figure 5.7 shows the effect of *X* on the transient stresses, where the stress values have been normalized with the respective steady-state values at the corresponding *X*. The figure shows that a decrease in *X* results in an increase in the height of stress maximum during the flow startup, which is qualitatively similar to the increased height of the *G"(γ)* maximum observed in oscillatory shear experiments performed at varying temperature (figure 5.1).

Shear startup experiments carried out at different temperatures using the same materials in figure 5.1 provide a direct test of the SGR model predictions. These results show that the relative height of the shear stress overshoot increases as the temperature is increased, as reported in figure 5.8.

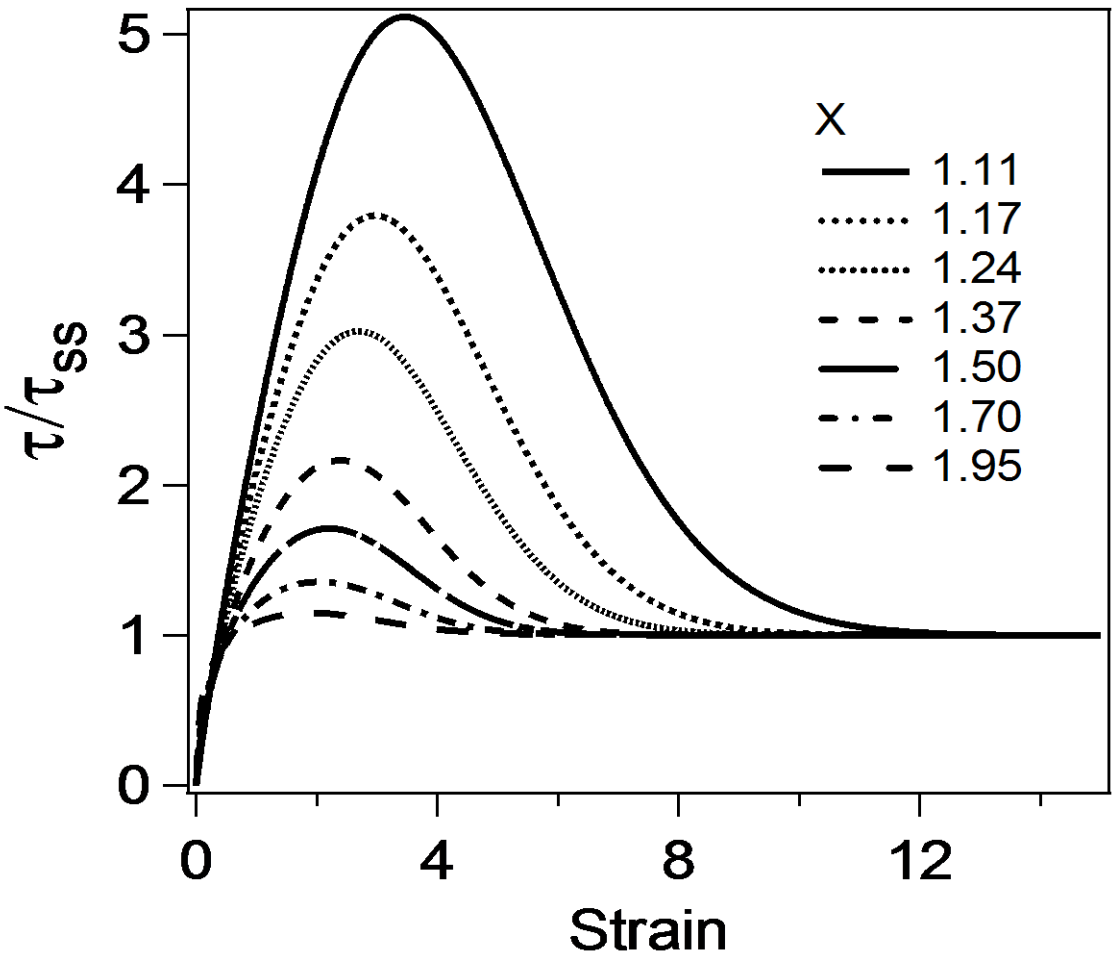

Figure 5.7 SGR model simulation results for a flow startup case at a shear rate of .01 sec^{-1}. Curves for different *X* values (increasing from top to bottom) demonstrate that decreasing *X* results in an increased overshoot in the stress during flow startup.

SGR model simulations were performed by S. Srivastava.

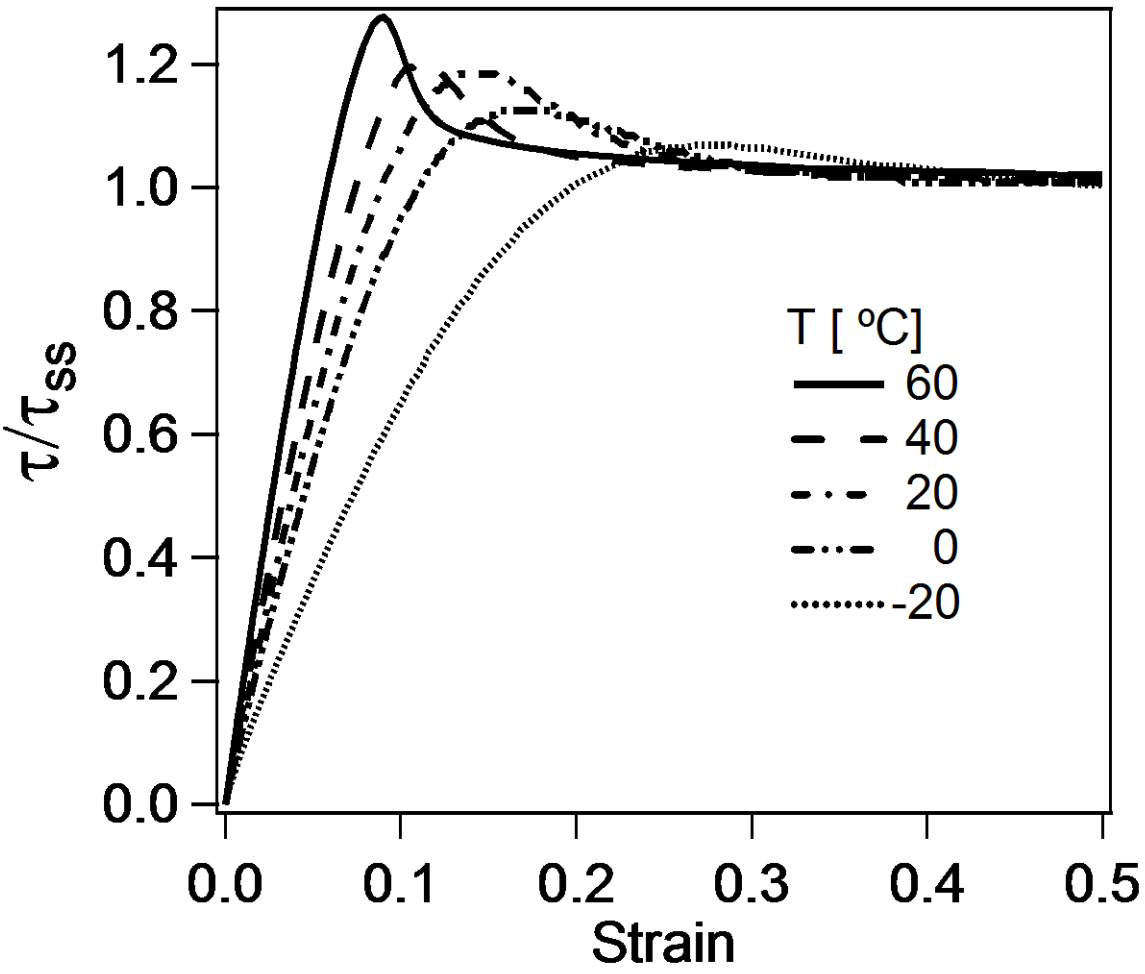

Figure 5.8 Experimental data for the startup of steady shear showing normalized stress vs. strain at different temperature at an applied shear rate of .01 sec^{-1}, waiting time of 500 s was allowed after preshearing for all the experimental measurements. There is a qualitative similarity in the trend of the height of the stress overshoot, where it increases with increase in temperature in the experiments and decreasing *X* in the SGR model.

This observation is consistent with the simulations results shown in figure 5.7 where *X*, is varied and further confirms our postulate from figure 5.6 that the noise temperature is a function of the measurement temperature. This agreement between experiments and simulations is observed at different shear rates, indicating that thermal jamming of soft glasses is a general characteristic of these materials.

Figure 5.1 and 5.8 also provide insights into the fragility [10, 19] of the glass phase with respect to strain. The maximum/overshoot in $G''(\gamma)$ and the stress overshoot during shear startup are understood to reflect shear-induced breaking of cages. Increases in the height and narrowing of the width of the overshoot in both the cases reflect a sharper transition from a solid to a liquid state, and hence are indicative of a mechanically more fragile glass phase. Therefore, increase in temperature leads to the formation of more jammed and yet mechanically more fragile glasses in this case.

Thermal jamming effect reported here bears resemblance to the reverse thermal vitrification behavior reported in solutions of star-branched polymers and blocks copolymer micelles by Vlassopolous and coworkers [12]. These authors found that the solution goes from a liquid to a solid state upon heating and argued that the behavior results from the formation of clusters of the stars upon heating, which give rise to the solid-like response observed. Primary reason for this effect was thought to be the change in solvent quality resulting from change in temperature. This mechanism should not be applicable to the materials studied here for two reasons: first the space filling requirement on the tethered chains [8] in a one component system such as the one studied here prevents formation of inhomogeneties and clusters; and second, the temperature dependent enthalpic effect that give rise to the formation of clusters are unlikely to be present in our system since the suspended and the suspending phase are the same.

5.4 Conclusions

In conclusion, we have discovered that an increase in temperature enhances jamming in a soft glassy material formed from polymer functionalized nanoparticles. The effect is visible from linear and nonlinear oscillatory shear measurements as well as from the magnitude and shape of the stress overshoot during start-up of steady shear flow. It is qualitatively the same for polymers of a variety of chemistries and can be described within the SGR model framework by coupling the noise temperature X to the conventional thermodynamic temperature. We conjecture that the origin of this unusual behavior originates from the affective attractive force between the polymer chains arising from the requirement that the tethered polymer chains have to uniformly fill the interparticle space. Such an attractive force should produce increasing excluded volume with increase in temperature. Our findings underscore the need for further studies that explicitly investigate the effect of temperature on the jamming phase diagram.

ACKNOWLEDGEMENTS

This work was supported by the National Science Foundation, Award No. DMR-1006323 and by Award No. KUS-C1-018-02, made by King Abdullah University of Science and Technology (KAUST. Facilities available though the Cornell Center for Materials Research (CCMR) were used for this study.

REFERENCES

1. A. J. Liu, S. R. Nagel, Nature **396**, 21 (1998).
2. V. Trappe, V. Prasad, L. Cipeletti, P. N. Segre, D. A. Weitz, Nature **411**, 772 (2001).
3. P.N. Pusey, W. van Megen, Nature **320**, 340 (1986).
4. T. G. Mason and D. A. Weitz, Phys. Rev. Lett. **75**, 2770 (1995)
5. Y. M. Joshi and R. K. Reddy, Phys. Rev. E **77**, 021501 (2008); A. Shahin, Y. M Joshi, Phys. Rev. Lett. **106**, 038302 (2011).
6. H. Lee, K. Paeng, S. F. Swallen, and M. D. Ediger, Science **323**, 231 (2009).
7. P. Agarwal, H. Qi, L. A. Archer, Nano Lett. **10**, 111 (2010); P. Agarwal, L. A. Archer, Phys. Rev. E **83**, 041402 (2011).
8. H. Y. Yu, D. L. Koch, Langmuir **26,** 16801 (2010).
9. P. Sollich, Phys. Rev. E. **58**, 738 (1998); P. Sollich et al., Phys. Rev. Lett. **78**, 2020 (1998).
10. J. Mattson et al. Nature **462**, 83 (2009).
11. C. Mayer et al., Nat. Mater **7**, 780 (2008).
12. M. Kapnistos et al., Phys. Rev. Lett. **85**, 4072 (2000); B. Loppinet, E. Stiakakis, D. Vlassopoulos, G. Fytas, J. Roovers, Macromolecules **34**, 8216 (2001); E. Stiakakis, D. Vlassopoulos, B. Loppinet, J. Roover, G. Meier, Phys. Rev. E **66**, 051804 (2002).
13. E. Stiakakis, D. Vlassopoulos, C. N. Likos, J. Roovers, G. Meier, Phys.. Rev. Lett. **89**, 20 (2002).
14. C. Derec et al. Phys. Rev. E **67**, 061403 (2003).
15. V. Carrier, G. Petekidis, J. Rheol. **53 (2)**, 245 (2009).
16. V. Awasthi, Y. M. Joshi, Soft Matter **5**, 4991 (2009).

17. G. Ovarlez, P. Coussot, Phys. Rev. E **76**, 011406 (2007).

18. de Gennes P.-G, Scaling concepts in polymer physics (Cornell Univ. Press, 1979).

19. C. A. Angell, K. L Ngai. G. B. Mckenna, P. F. Mcmillan, S. W. Martin, J. Appl. Phys. **88**, 3113 (2000).

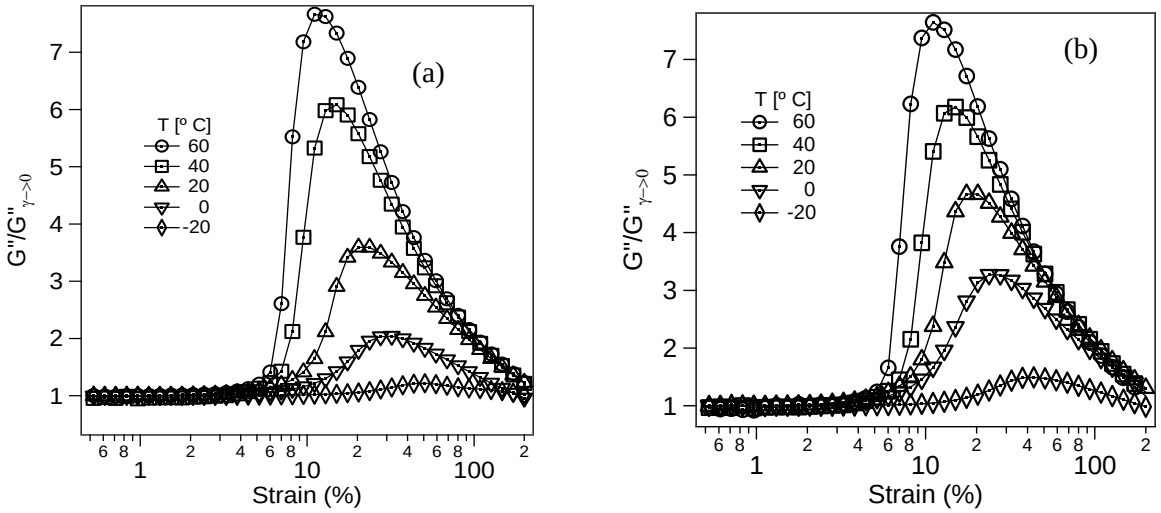

Supplementary figure 5.1 Oscillatory amplitude sweep at different temperatures at an angular frequency of **(a)** ω = 5 rad/s and **(b)** ω = 1 rad/s. Similar to figure 5.1, height of the maxima in *G"* increases with increase in temperature. Waiting time of 5000 s was allowed after the preshearing for the measurements at every temperature.

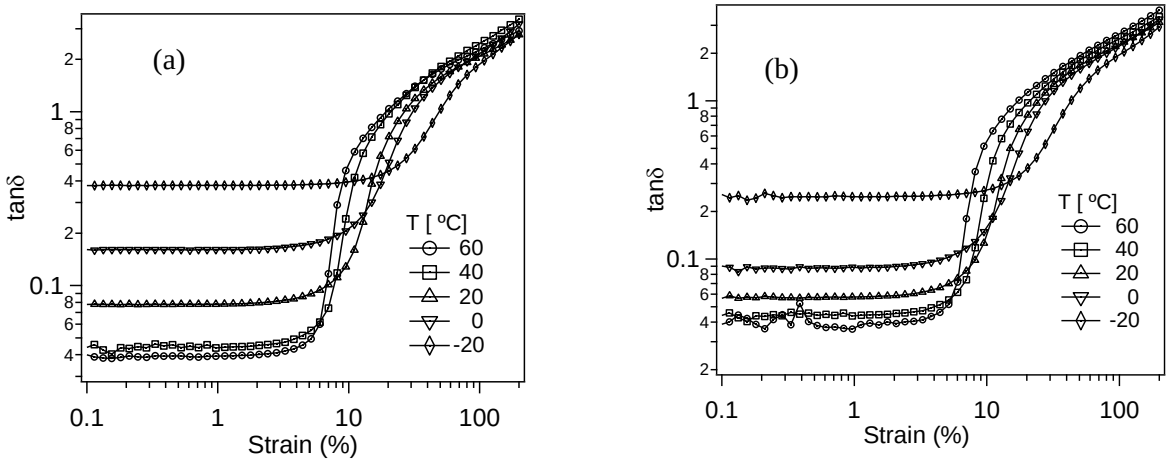

Supplementary figure 5.2 *tanδ* vs. strain amplitude at different temperature for the data in supplementary figure 5.1 **(a)** ω = 5 rad/s and **(b)** ω = 1 rad/s. Similar to figure 5.2, linear value of *tanδ* decreases with increase in temperature.

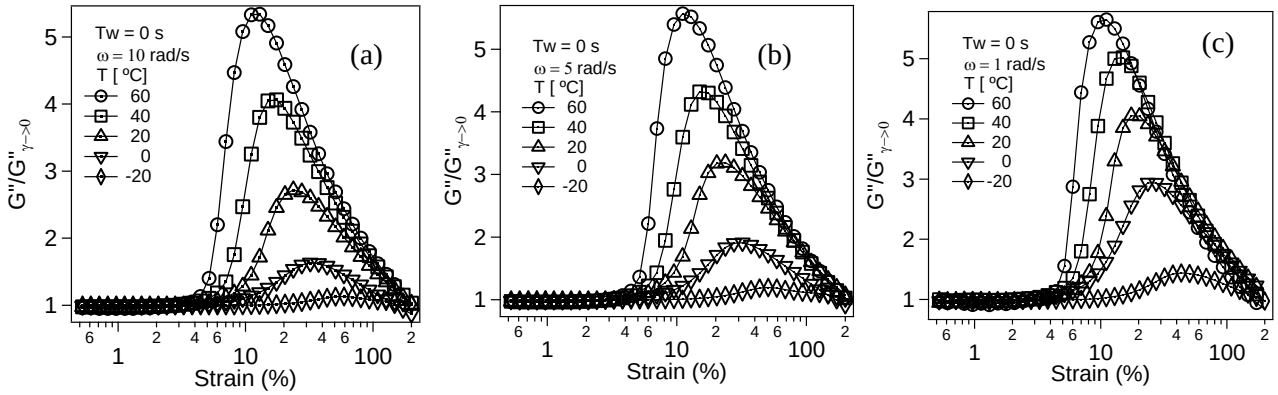

Supplementary figure 5.3 Measurements performed at a waiting time of 0 s: Oscillatory amplitude sweep at different temperatures at an angular frequency of **(a)** ω = 10 rad/s, **(b)** ω = 5 rad/s and **(c)** ω = 1 rad/s. Similar to figure 5.1, height of the maxima in *G"* increases with increase in temperature, even at a waiting time of 0 sec.

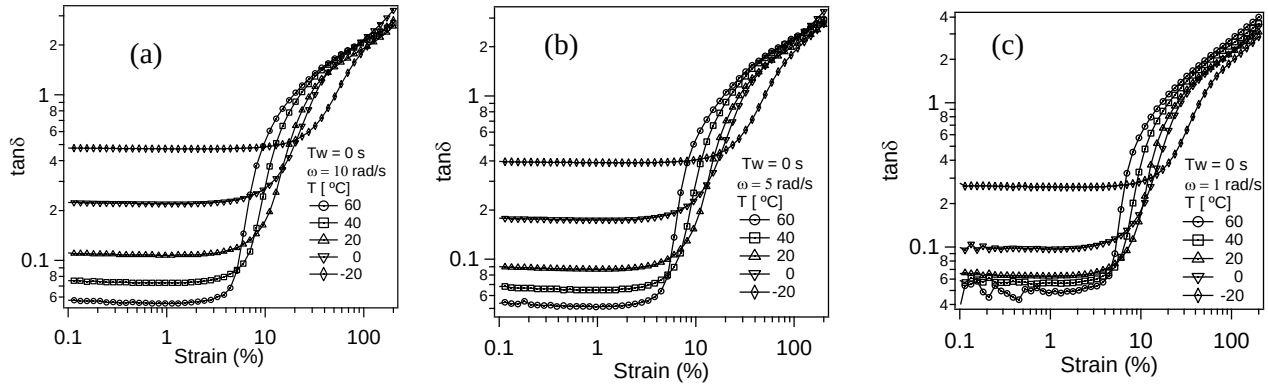

Supplementary figure 5.4 *tanδ* vs. stain amplitude for the data in supplementary figure 5.3: **(a)** ω = 10 rad/s, **(b)** ω = 5 rad/s and **(c)** 1 rad/s. Similar to figure 5.2, linear value of *tanδ* decreases with an increase in temperature.

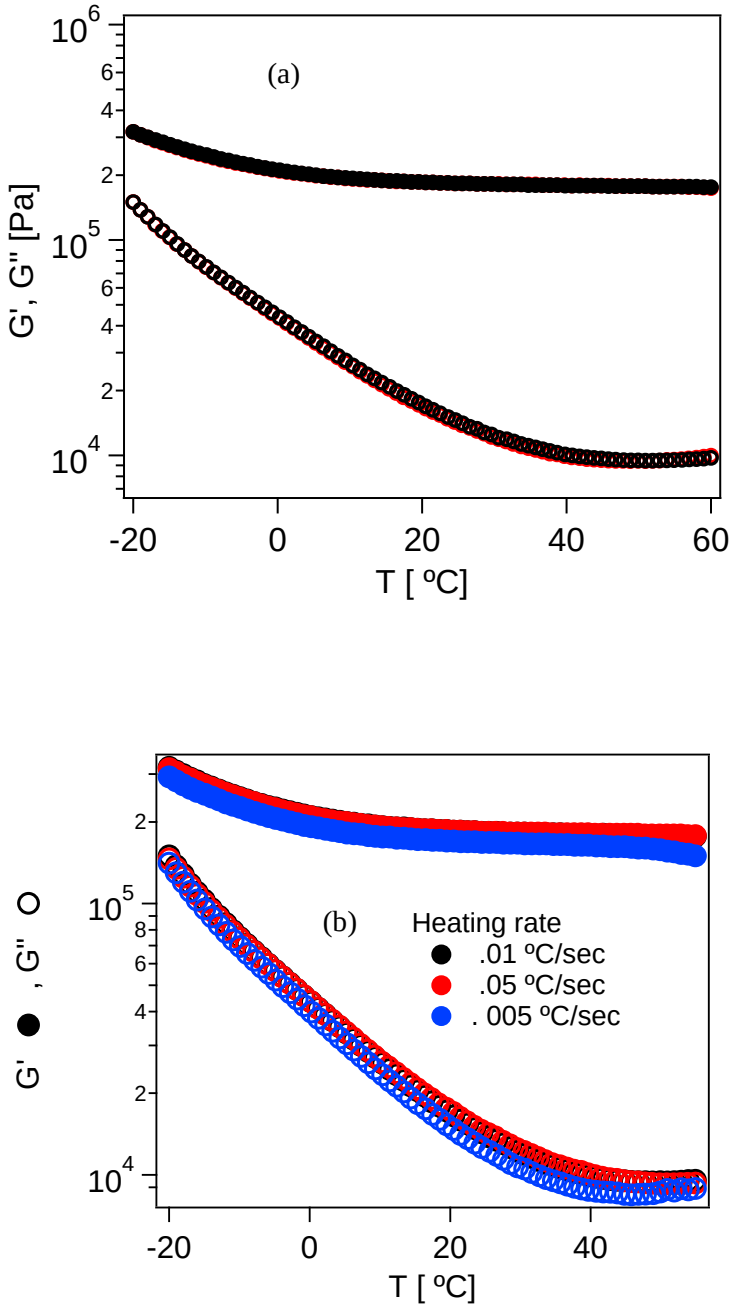

Supplementary figure 5.5 (a) Temperature sweep performed with increasing and decreasing temperature. Black symbols represent data for increasing temperature and red symbols represent data for decreasing temperature. Heating and cooling rate is .01 ˚C/min. It can be seen the effect of temperature change is completely reversible. **(b)**Temperature sweep carried out at different heating rates shown in the legend. Data is unaffected by the change in heating rate. Similar results were found to be valid for different cooling rates also.

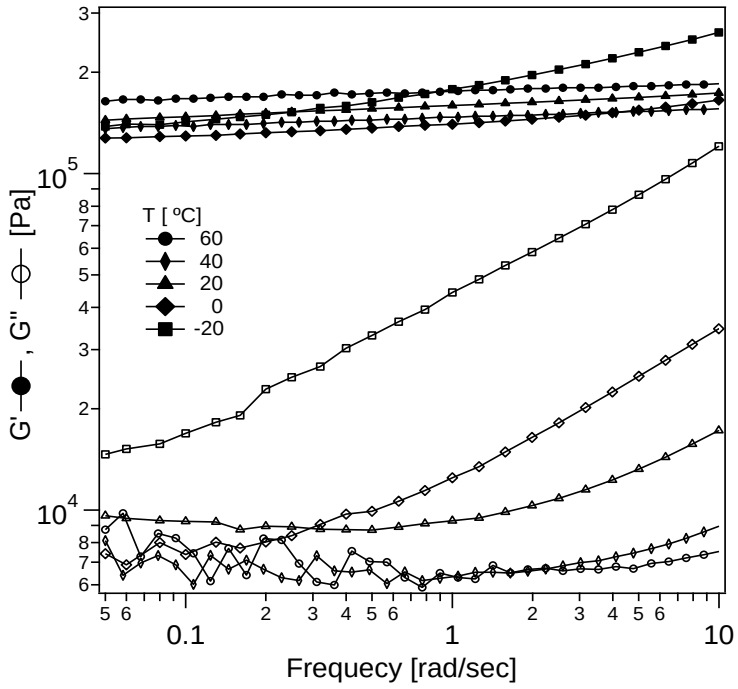

Supplementary figure 5.6 Frequency sweep at different temperatures, showing increasingly weaker frequency dependence of both *G'* and *G"*; implying a more solid like response with an increase in temperature.

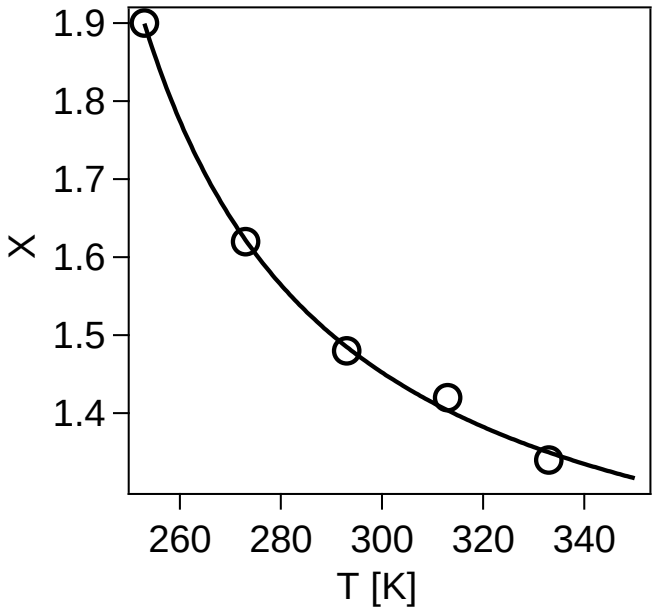

Supplementary figure 5.7 Noise temperature, *X*, as a function of temperature obtained from the slope of *G"* in the non linear regime following the overshoot. *X* is obtained from $G'' \sim \gamma^{2-X}$ as stated in ref [14]. Similar to figure 5.6, *X* obtained from the nonlinear regime also decreases with an increase in temperature. Line is guide to the eye.

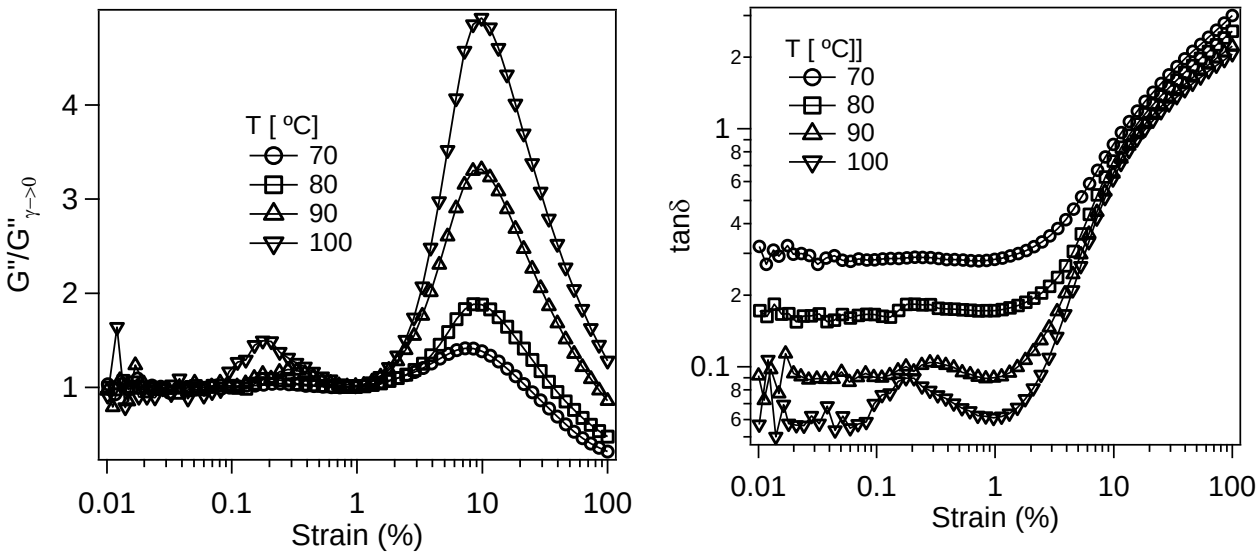

Supplementary figure 5.8 Data for self-suspended suspensions created by tethering polyethylene glycol (PEG) chains to silica nanoparticles. Molecular weight of the PEG chains is 2000 and the size of the silica nanoparticles is 10 nm with a core volume fraction of 16.1 %. In this system also, increase in temperature results in increased jamming implying that the reported thermal jamming is not dependent on the corona chain chemistry.

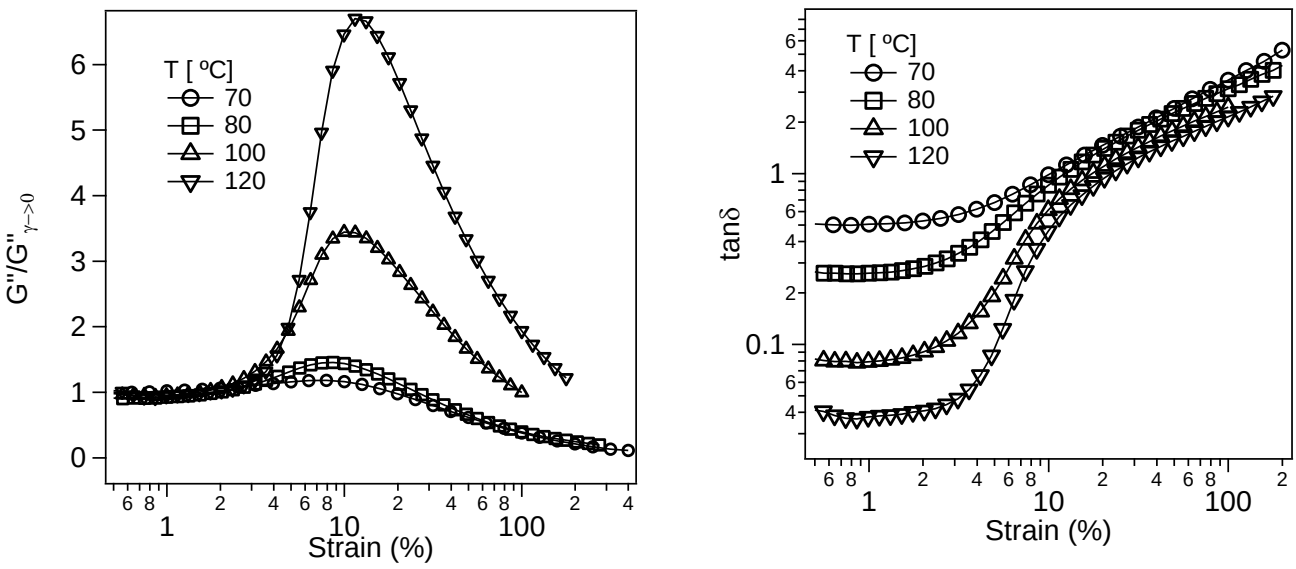

Supplementary figure 5.9 Data for self-suspended suspensions created by tethering PEG chains to silica nanoparticles, showing similar trends as figures 5.1 and 5.2. Molecular weight of the PEG chains is 5000 and the size of the silica nanoparticles is 10 nm with a core volume fraction of 12.2 %.

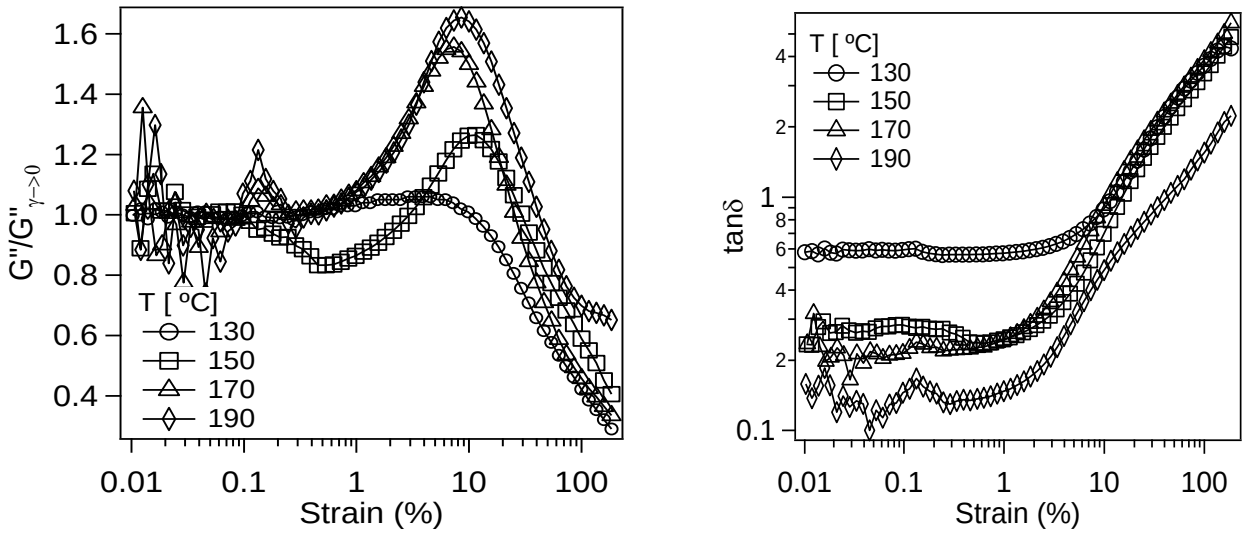

Supplementary figure 5.10 Data for self-suspended suspensions created by tethering polystyrene chains to silica nanoparticles, showing similar trends as figures 5.1 and 5.2. Molecular weight of the polystyrene chains is 3500 and the size of the silica nanoparticles is 10 nm with a core volume fraction of 17 %.

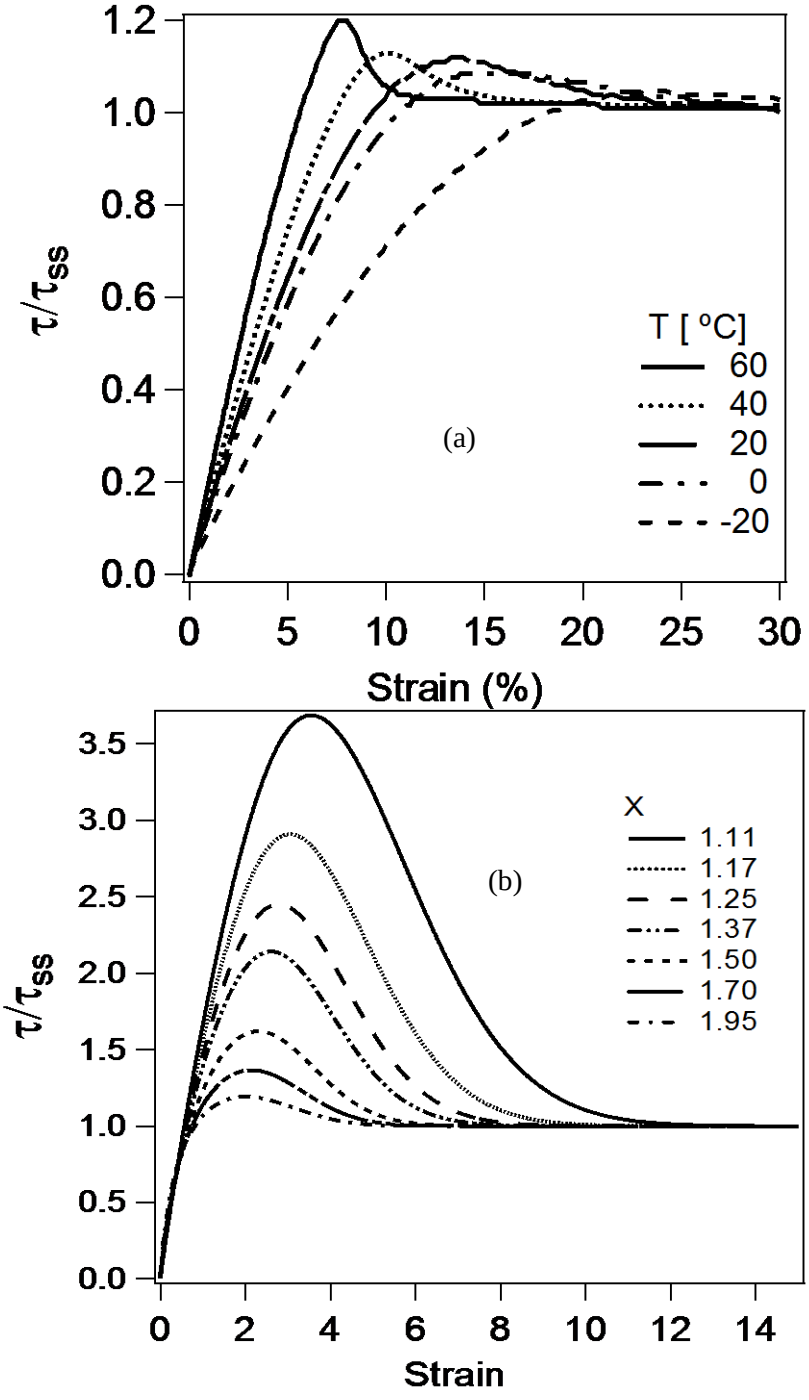

Supplementary figure 5.11 (a) Experimental data for the startup of steady shear showing normalized stress vs. strain at different temperature at an applied shear rate of .001 sec^{-1}. **(b)** SGR model simulation results for a flow startup case at a shear rate of .1 sec^{-1}.

Derivation for the expression relating *X* to *δ:*

G' and *G''* can be obtained from the Fourier transform of the relaxation modulus *G(t)* given by

$$G^*(\omega) = i\omega \int_0^\infty dt e^{-i\omega t} G(t)$$

In the SGR model, for $\rho(E) = \exp(-E)$, $G(t) \sim t^{1-X}$

so

$$G^*(\omega) \sim i\omega \int_0^\infty dt e^{-i\omega t}\, t^{1-X}$$

This can be simplified as

$$G' \sim \omega \int_0^\infty dt sin(\omega t) t^{1-X}$$

and

$$G" \sim \omega \int_0^\infty dt cos(\omega t) t^{1-X}$$

Substituting $\omega t = z$

$$G' \sim \omega^{X-1} \int_0^\infty dz sin(z) z^{1-X}$$

This gives

$$G' \sim \omega^{X-1} sin\left(\frac{\pi}{2}(X-1)\right)\Gamma(2-X) \qquad for\ 1 < x < 3$$

Similarly

$$G" \sim \omega^{X-1} cos\left(\frac{\pi}{2}(X-1)\right)\Gamma(2-X); \qquad for\ 1 < x < 2$$

Hence

$$tan\delta = \frac{G"}{G'} = tan\left(\frac{\pi}{2}(X-1)\right)$$

So

$$X = 1 + \frac{2}{\pi}\delta; \qquad for\ 1 < x < 2$$

We have performed simulations from SGR model for different values of *X* to verify the above expression. Below is the plot showing comparison of *X* with the above expression.

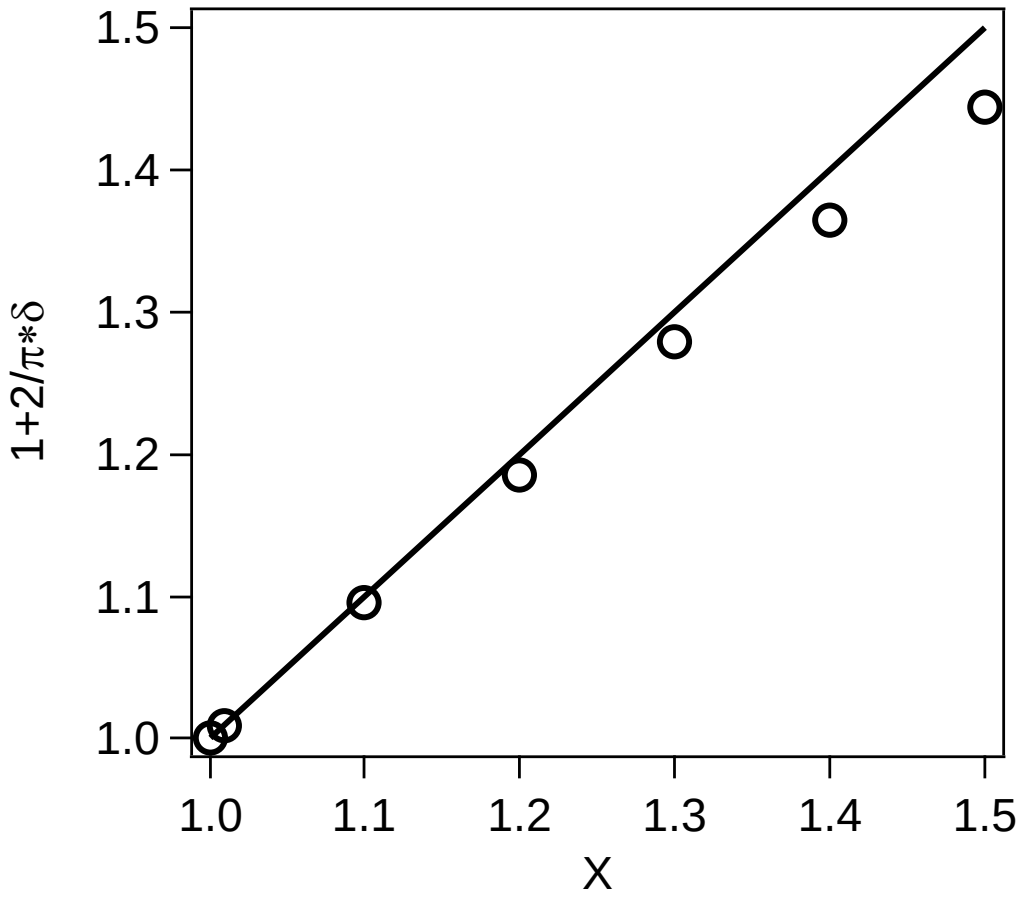

Supplementary figure 5.12 Results showing the value of $1 + (2/\pi)*\delta$ obtained from SGR model simulations for different values of *X*. The solid line is $y = x$ line for comparison. Value of $1+ (2/\pi)*\delta$ lies close to *X*, validating our expression.

CHAPTER 6

Strain Accelerated Dynamics of Soft Colloidal Glasses

Reproduced with permission from

Phys. Rev. E **83**, 041401 (2011)

P. Agarwal, L. A. Archer

6.1 Abstract

We have investigated the strain-accelerated dynamics of self- and oligomer-suspended nanoparticle fluids theoretically and experimentally. Mechanical rheology measurements performed on a variety of systems reveal significant evidence for speeding-up of relaxation at modest shear strains in both step and oscillatory shear flows. Using the Soft Glassy Rheology (SGR) model framework, we show that the observed behavior is a fundamental, but heretofore unexplored, attribute of soft glasses.

6.2 Introduction

The concept of deformation-accelerated dynamics in soft matter dates back to the seminal work of Eyring in the 1930s on polymeric glasses [1]. The central idea is that deformation lowers the energy barrier for molecular motions hence enhancing the molecular mobility of the glass phase. Within the last decade, there have been significant advances in the characterization tools for studying the effect of deformation on dynamics, which has lead to accumulating evidence of stress, strain, and strain-rate accelerated relaxation in polymeric glasses. Lee at al. [2], for example, used a photobleaching technique to probe the molecular mobility of poly(methylmethacrylate) during uniaxial elongation. These authors reported that more than a 1000-fold increase in molecular mobility of PMMA is produced by extension. More recently, Warren et al. [3] studied relaxation dynamics in deformed polymer glasses using molecular dynamic simulations. They found that macroscopic strain is the key variable controlling acceleration of relaxation dynamics, independent of the deformation protocol or aging time.

There has been a considerable interest in studying colloids as model systems to understand the glass transition [4, 5]. Colloidal glasses are now generally understood to exist in metastable

structural states in which individual material elements (particles) are trapped in potential energy wells deeper than thermal energy [6, 7]. In these systems, deformation is required to achieve any structural relaxation [6- 8]. In laponite suspensions, Joshi et al. [9] reported that an external shear stress produces an effect on structural relaxation analogous to temperature. Recently we reported that in large-amplitude oscillatory shear, the shear strain could be used in an analogous fashion to temperature in polymers to dramatically extend the dynamic range accessible to the experiments [10]. Termed time-strain superposition (TSS), this process is similar to the strain-rate frequency superposition (SRFS) methodology reported by Wyss et al. [11], wherein the strain rate is the variable used to extend the experimental time window. Herein we report direct evidence of strain-accelerated relaxation dynamics in soft glasses. We also show that these observations are consistent with soft glassy rheology (SGR) model and are in fact central to the recent discovery of TSS in soft glasses [10].

6.3 Materials and Methods

This study focuses on self-suspended suspensions [10, 12] created by tethering polyisoprene (PI) chains to silica nanoparticles. Termed Nanoscale ionic materials (NIMs), these materials are attractive because they display fluid like properties even in the absence of any external solvent. This feature arises in a straightforward way from the abundance of polymeric fluid tethered to the particles, but has fundamental consequences for the structure factor, particularly at small scattering angles [12]. Because the particles and suspending medium (tethered polymer) are chemically coupled, NIMs have been termed self-suspended nanoparticle fluids [10, 12], and are exceptionally stable against aggregation. We believe the latter feature makes them good models for soft glasses [10].

To characterize the relaxation dynamics of NIMs, mechanical rheology measurements were performed at a temperature of 25 °C in step and oscillatory shear using Rheometrics Scientific ARES and Anton Paar MCR 501 rheometers equipped with cone and plate fixtures. Before every measurement, sample was presheared by applying a large amplitude oscillatory shear strain sweep ranging from a strain of 0.01 % to 200 % at a frequency of 10 rad/s to erase any history due to loading or previous deformations. After the preshear, sufficient waiting time was allowed before performing the actual measurement and the waiting time was kept large as compared to the measurement time.

Results reported here are for a single NIMs material with silica volume fraction $\phi = 0.12$ and PI molecular weight of 5000, size of the silica nanoparticles is 10 ± 2 nm. To ensure that the experimental results are not specific to a particular material, we have carried out the same experiments on two more systems (a) NIMs system with polyethylene glycol (PEG) as corona and (b) suspensions created by dispersing PEG tethered hairy nanoparticles in PEG oligomer hosts. We have reported the results for these two systems in the Appendix.

6.4 Experimental Results

Wide variety of materials raging from foams, emulsion, suspension and star polymers etc. have displayed similar features in their rheology, understood to originate from metastability and disorder in these systems. “Soft Glass” is a commonly used term for such materials which display common rheological features including yield stress and slow dynamics. Figure 6.1 shows the effect of shear strain on the storage (G') and loss (G'') modulus of this material. All of the features displayed, including the G'-dominant linear viscoelastic regime followed by the pronounced loss maximum prior to the onset of strain-softening are consistent with expectations

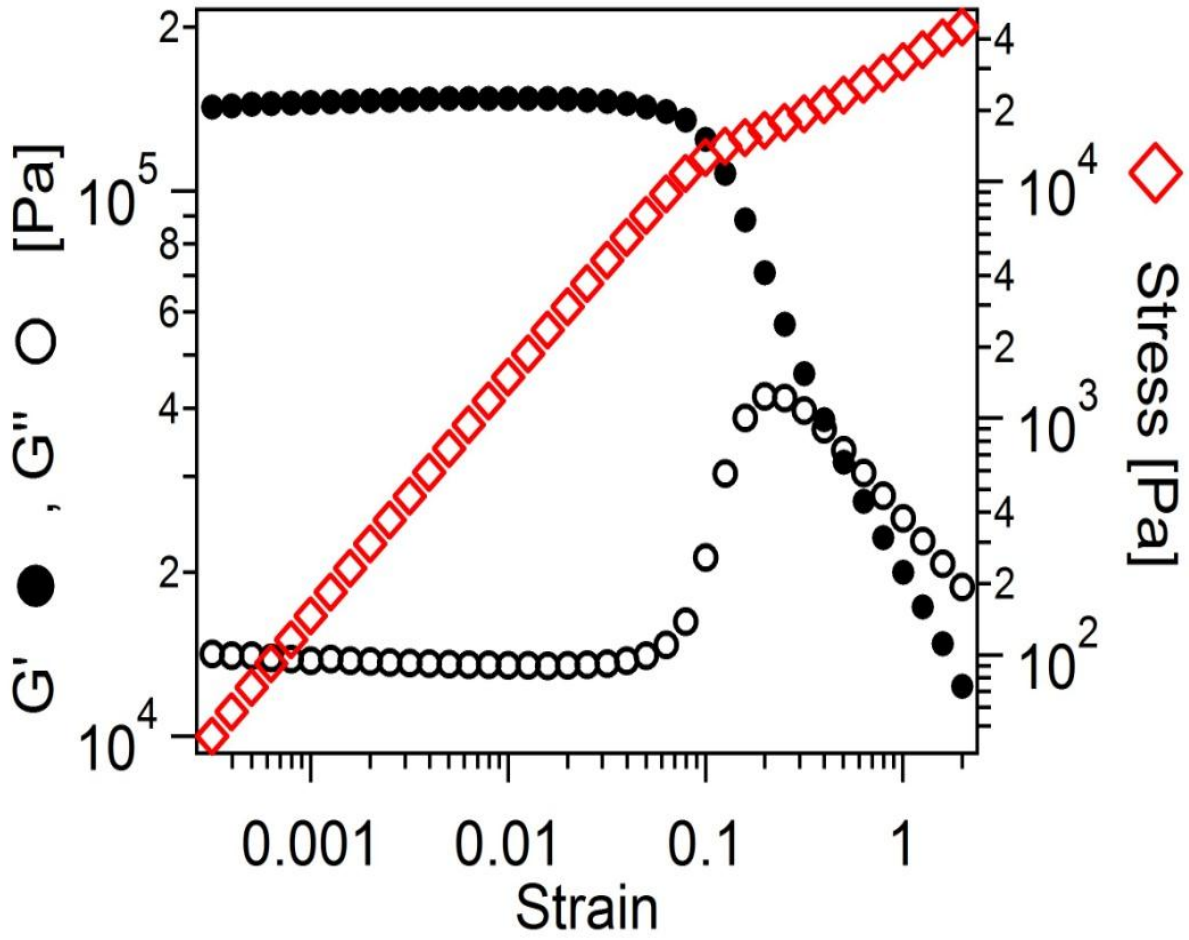

Figure 6.1 Strain sweep measurements at a frequency of 10 rad/sec.

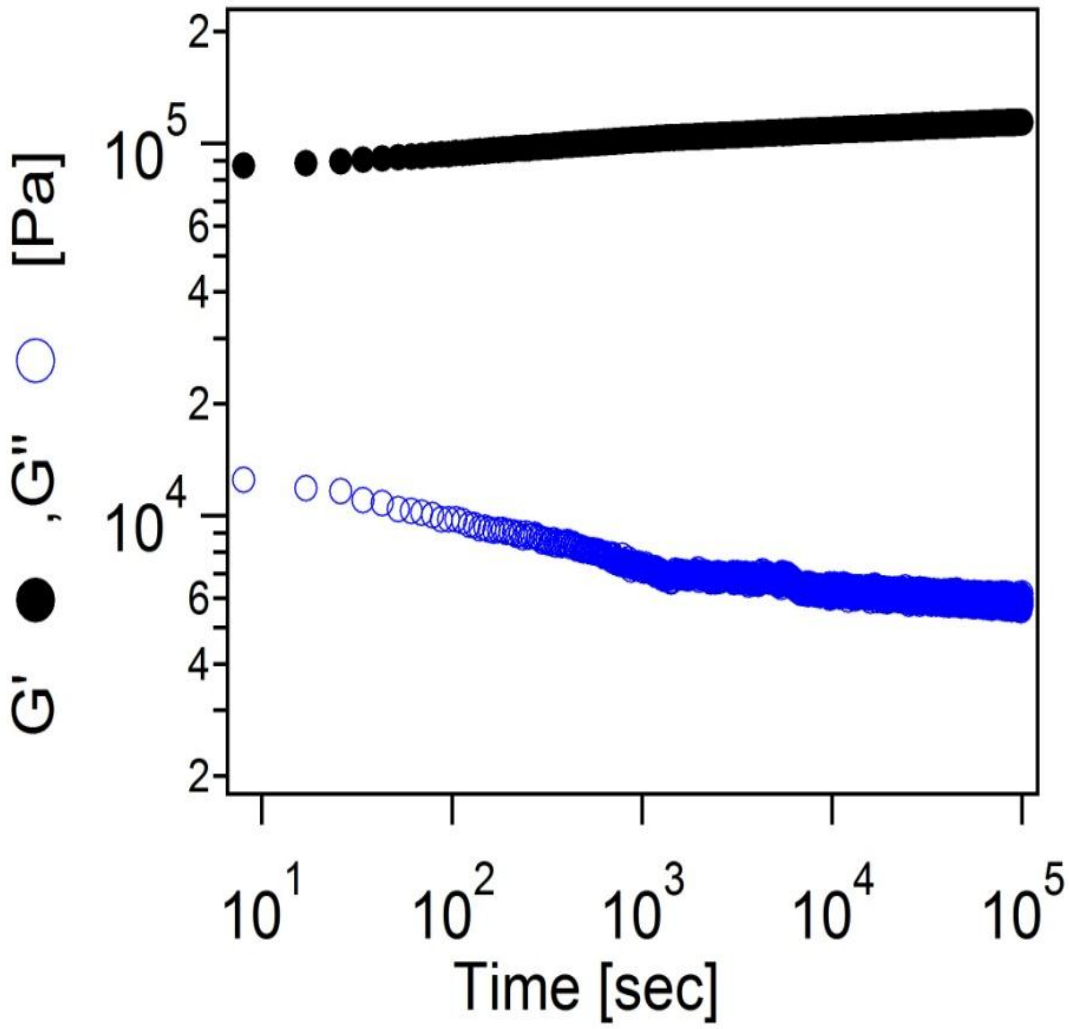

Figure 6.2 *G'* and *G''* as a function of time after preshear by strain sweep ranging from .01 % to 200 %. After the preshear, γ =. 5 % and ω = 5 rad/sec have been applied to record the moduli as a function of time.

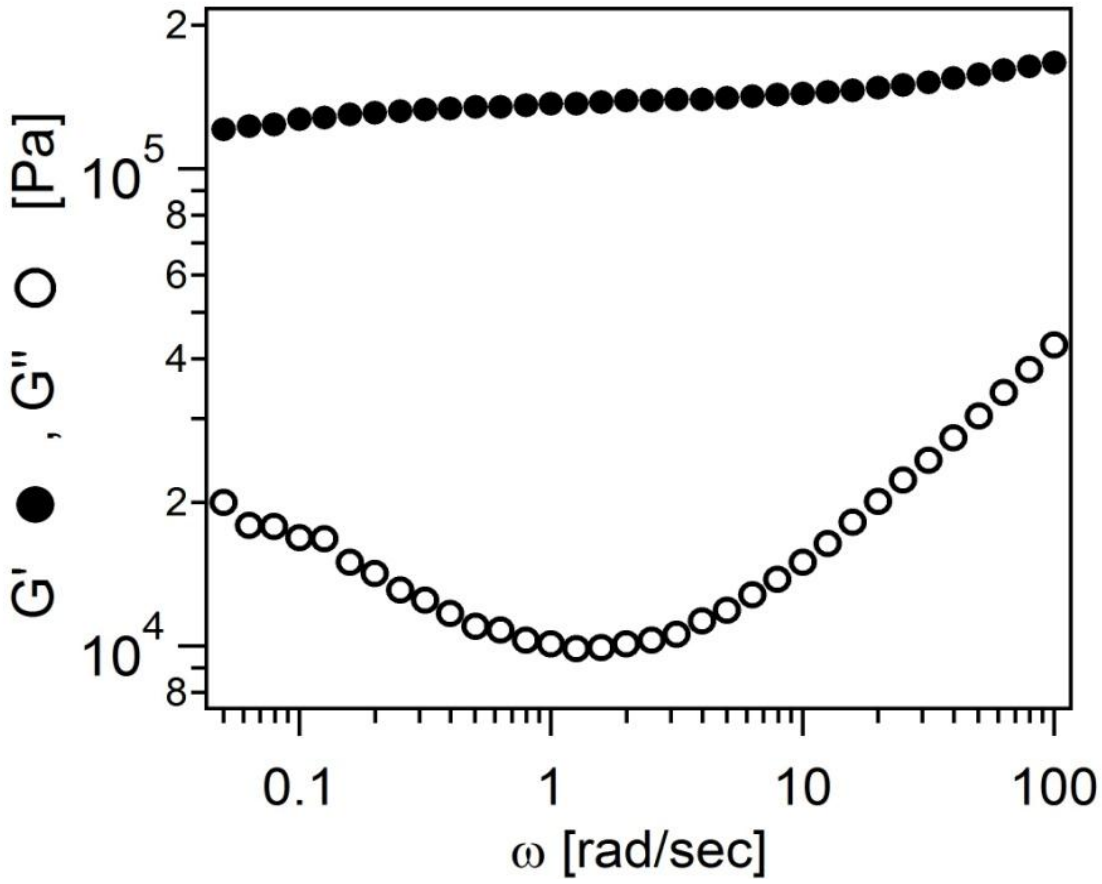

Figure 6.3 Frequency sweep at strain of .5%.

for soft glasses [5-7, 10-11, 13-14] where this behavior is attributed to the breaking of cages in the material at high strain.

One complication that arises in the study of soft glassy materials is that their properties change with time. This phenomenon is called “aging” and is understood in terms of material sampling deeper and deeper wells in the energy landscape [7] with elapsed time, which gives rise to waiting time dependent properties of the material. Figure 6.2 shows the time evolution of the viscoelastic moduli after preshear. It can be clearly seen from the plot that there is no significant change in the value of both *G’* and *G”* with time, signifying that the effect of aging in these systems is negligible.

Figure 6.3 shows the linear viscoelastic response of the same material as a function of shear frequency. The response is again seen to be typical for a soft glass [5-7, 11, 13-14]. The upturn in the loss modulus seen at low frequency in Figure 6.3 is also common for many soft glasses [5-7, 11, 13]; it appears to pre-sage a structural relaxation process outside of the frequency window accessed by the experiment. As reported previously for nanoparticle suspensions [15], measurement of the relaxation modulus $G(t) = \sigma(t)/\gamma$ following application of a step strain $\gamma(t) = \gamma H(t)$ where σ is stress and $H(t)$ is a step function, provides a straightforward method for extending the dynamic range of the oscillatory shear experiment and provides the most direct comparisons of experimental data with SGR model predictions [16]. Prior to each step strain measurement, the material was pre-sheared using large amplitude oscillatory shear and rested for a period of 5000 seconds. Figure 6.4 shows $G(t)$ at multiple shear strains for the first 500 seconds following imposition of the step strain; the observation time is limited to ensure that the measurement time is much smaller than the resting/waiting time [17, 18].

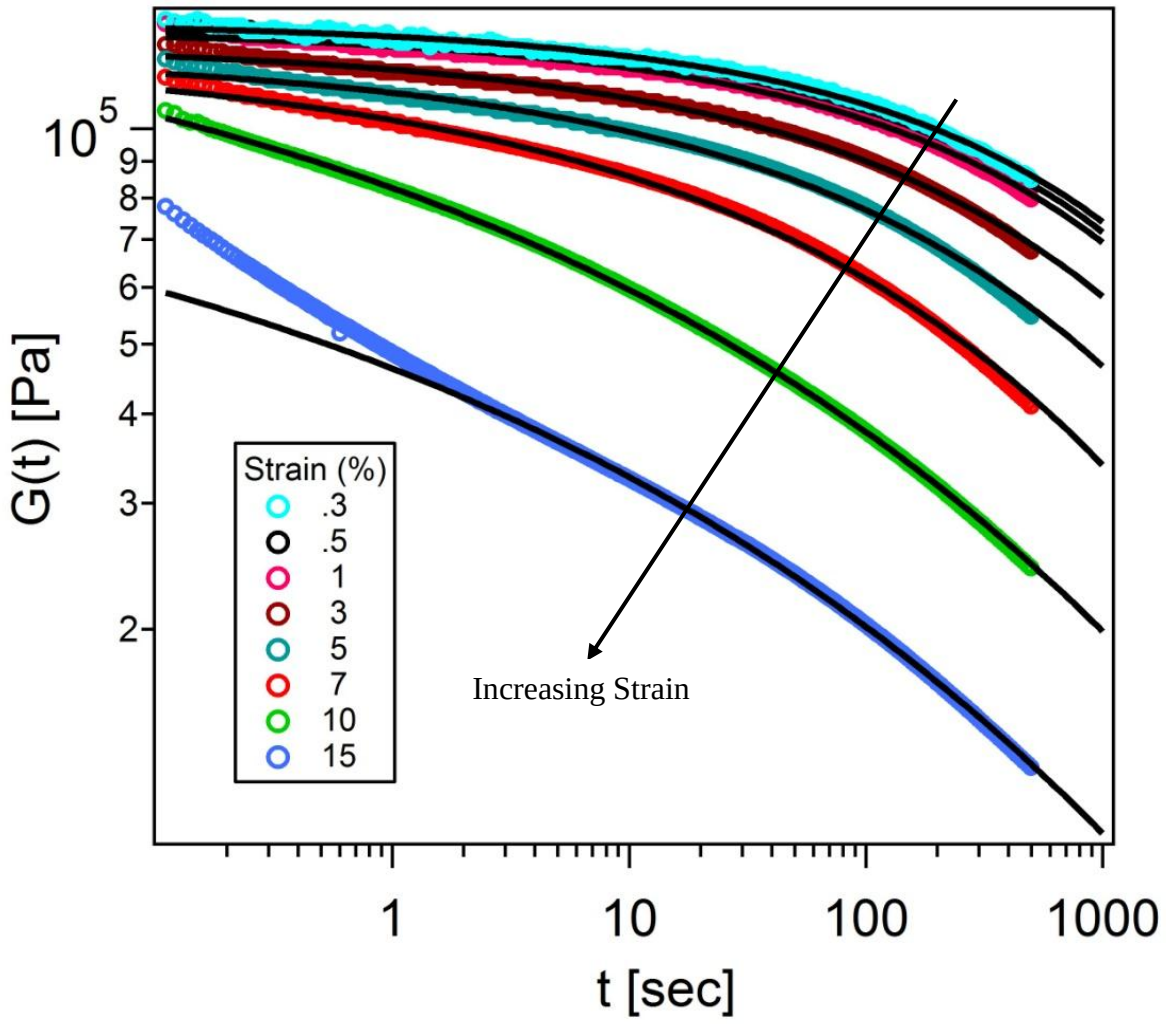

Figure 6.4 Relaxation modulus vs. time for increasing strain (from top to bottom), decay of the modulus is faster at higher strains. Lines are fits with the KWW expression described by *eq.* 6.1.

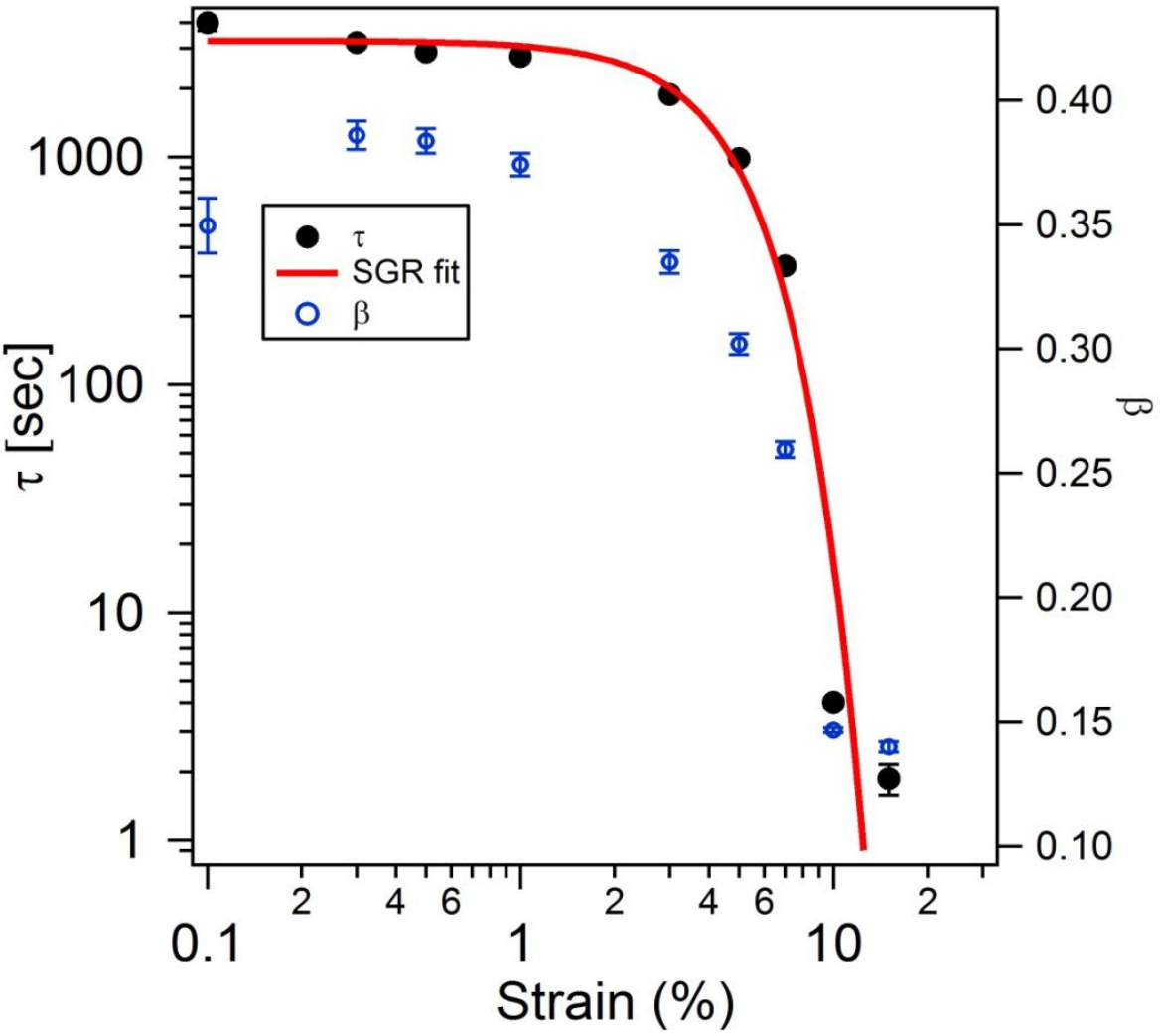

Figure 6.5 parameters τ and β obtained from KWW fits for different strains, characteristic time τ decreases with strain and β shows slight decrease with strain. Solid line is fit from *eq.* 6.2 with τ_0 = 3230.8 sec and k = 526.1

It is apparent that the long-time decay of $G(t)$ speeds up considerably with increasing shear strain. The continuous lines in the figure 6.4 indicate that the stress relaxation is of the stretched exponential or Kohlrausch – William –Watts (KWW) form [2, 19-22]:

$$G(t) = A\exp\left(-\left(\frac{t}{\tau}\right)^{\beta}\right) \qquad (6.1)$$

Where A is zero time or baseline value of the relaxation modulus, t is time, τ is the characteristic relaxation time and β is the coupling parameter. The characteristic time, τ, and coupling parameter β deduced from the fits are provided in Figure 6.5. It can be seen from the figure that τ is constant al low strains, indicative of linear viscoelastic regime and it decreases substantially at high strains, consistent with visual observation, as well as with the earlier reports by Lee et al. [2] and Warren et al. [3] for polymeric glasses. The exponent β decreases with shear strain, but the change is more modest than reports for polymeric glasses [2, 3], where the distribution of relaxation times is narrowed markedly by increasing the strain. Solid line in Fig. 6.5 is fit from the equation

$$\tau = \tau_0 \exp(-k\gamma^2) \qquad (6.2)$$

with τ_0 = 3230 ± 156 sec and k = 526 ± 105, where τ_0 is relaxation time under very small strain and k is a constant. As discussed later, origin of this functional form can be predicted from SGR model [6, 7].

As reported recently by Bandopadhyay et al. [19], $G(t)$ relaxes via a two-step (fast, followed by slow) decay, as clear in Figure 6.4 the fast relaxation mode at small time appears at a strain of 15 % which indicates towards the possibility that the fast mode appears only at strains higher

than the yield strain (the yield strain is determined from Figure 6.1 from stress vs. strain data as the strain at which stress vs. strain becomes nonlinear). Range of strains was limited for Figure 6.4 because beyond the yield strain, it is not possible to fit the entire spectrum using KWW function, implying that KWW may not be the appropriate functional form for of the stress relaxation at high strains. We have therefore probed the dynamics at higher strains using oscillatory shear measurements.

In a frequency sweep experiment, inverse of the frequency where the crossover between the storage and loss modulus occurs is an indicative of the relaxation time [23]. As shown in figure 6.3, within the linear regime (at low strain) the crossover between the two moduli is not accessible within the experimental frequency window. If strain accelerates structural dynamics of soft glasses, as evident from our step shear measurements, the crossover between the storage and loss modulus should be accessible in a frequency sweep experiment performed at high stains. Figure 6.6 shows that this is indeed the case for our materials, and that the cross-over from a *G'*-dominant to a *G"*-dominant dynamic mechanical response occurs at a progressively higher oscillatory frequency as the strain is increased implying decreasing relaxation time with increasing strain. The figure also shows that the value of the modulus at the crossover frequency remains essentially unaffected by the shear strain; an indication that the principal effect of strain in this range is to accelerate the dynamics.

6.5 Theoretical Results

The Soft glassy rheology model (SGR) proposed by Sollich et al. [6, 7] provides a theoretical framework for understanding the phenomena revealed by our experiments. For a step-shear strain of amplitude γ, this model predicts:

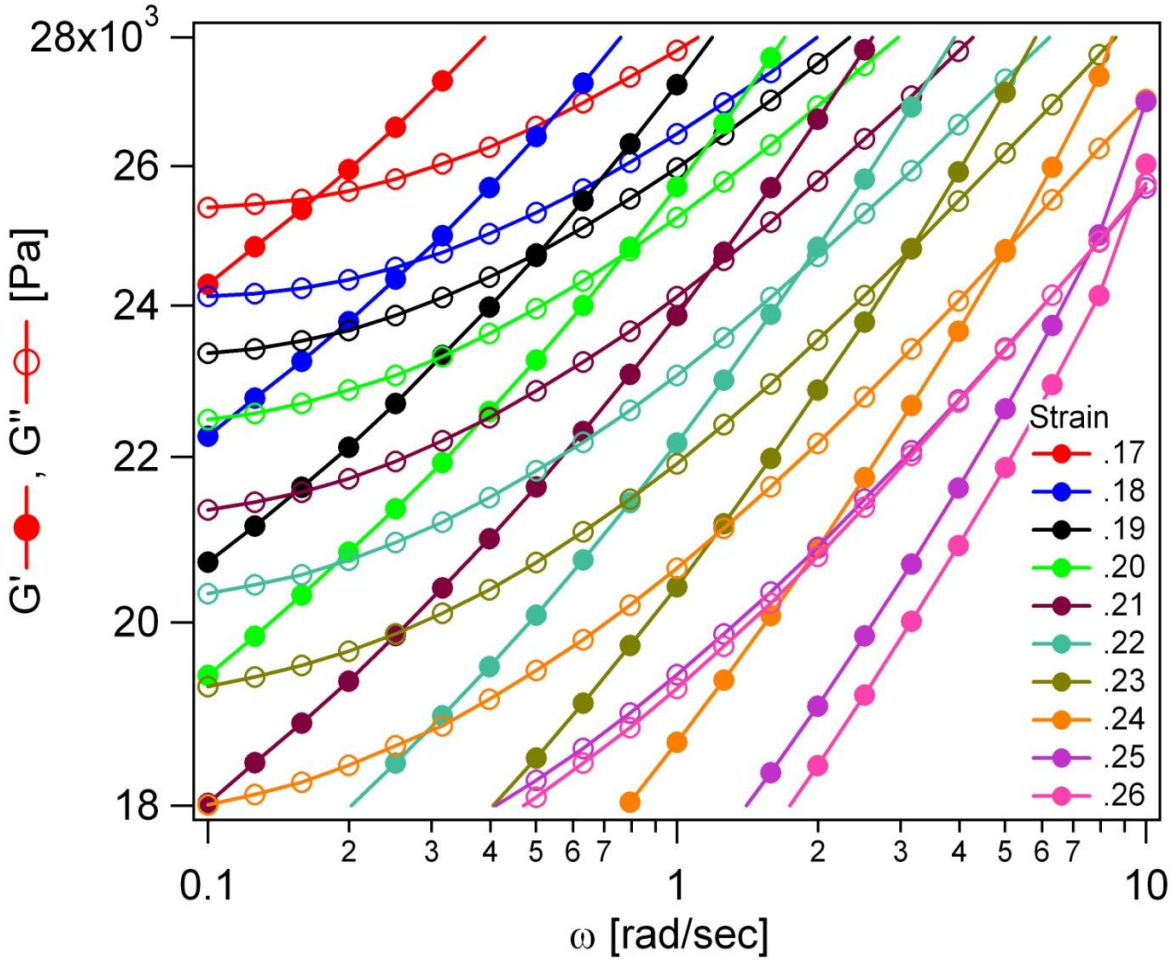

Figure 6.6 Storage and loss modulus vs. frequency at different strains: contrary to the linear viscoelastic regime, the crossover between the two is accessible at high strains. Crossover frequency increases with increasing strain, implying the decrease of characteristic relaxation time with increasing strain.

$$\sigma(t) = \gamma G_{eq}\left(e^{\frac{\gamma^2}{2X}}t\right) \qquad (6.3)$$

Thus, relaxation modulus $G(t)$ is given by:

$$G(t) = \frac{\int dE\rho(E)\exp\left(\frac{E}{X}\right)\exp\left(-\exp\left(\frac{\gamma^2}{2X}\right)t\exp\left(-\frac{E}{X}\right)\right)}{\int dE\rho(E)\exp\left(\frac{E}{X}\right)} \qquad (6.4)$$

Where $\rho(E)$ is the probability density of yield energies, X is the effective noise temperature describing the typical energy available for hopping, E is yield energy, t is time and G_{eq} is a function describing the decay of relaxation modulus with time (please see [6] for more details). Substituting $\rho(E) = \exp(-E)$ and integrating *eq*. 6.4 for different shear strains leads to the relaxation moduli reported in Figure 6.7. As was the case for the experimental results, it is again immediately apparent that the curves obtained at high strain are shifted towards lower times, implying that at high strain, it takes a smaller time for $G(t)$ to decay to the same value as at lower strains. It is also apparent from these plots that the shape of the relaxation modulus at different strains is self similar, implying that $G(t)$ obtained at discrete shear strains can be superimposed to form a master curve as shown in the Figure 6.8. This prediction of time-strain superposition behavior from the SGR model is consistent with our recent experimental discovery of the same [10].

Superposition in figure 6.8 is obtained by shifting the curves on the time axis by a shift factor a_γ which can be described as

$$G(\gamma, ta_\gamma) = G(0,t) \qquad (6.5)$$

The functional form of the strain-dependent acceleration factor a_γ can also be deduced from the SGR model by fitting (inset Figure 6.8) the strain dependence of the shift factors required to achieve superposition to give:

$$a_\gamma = \exp\left(-\frac{\gamma^2}{2X}\right) \qquad (6.6)$$

This functional form is, unsurprisingly, precisely the same as the factor multiplying the time scale in *eq*. (6.3). Shift factor a_γ in equation (6.5) describes the shifting of time scale in SGR model due to application of strain. Functional form of the shift factor (*eq.* 6.6) is strikingly similar to *eq.* 6.2 which describes the effect of strain on the relaxation time obtained from the fits to the measured relaxation modulus. The analysis reported here uses a value of the noise temperature $X = 1.05$ and can be extended to the case $X < 1$, following the framework provided by Fielding et al. [7], to account for aging in SGR model framework.

There have been numerous studies on the effect of shear on aging dynamics [24-26]. Particularly relevant to our findings is the work by Ozon et al. [26] where it was reported that shear speeds up aging and that the acceleration factor is of the form $exp(-\gamma/\gamma_c)$, where γ_c is critical strain. The authors argued that an Eyring type model describes the effect of shear on aging. Our observations are quite different. Specifically, we find that deformation accelerates relaxation dynamics during application of shear, and that the acceleration factor is of the form $exp(-\gamma^2/2X)$.

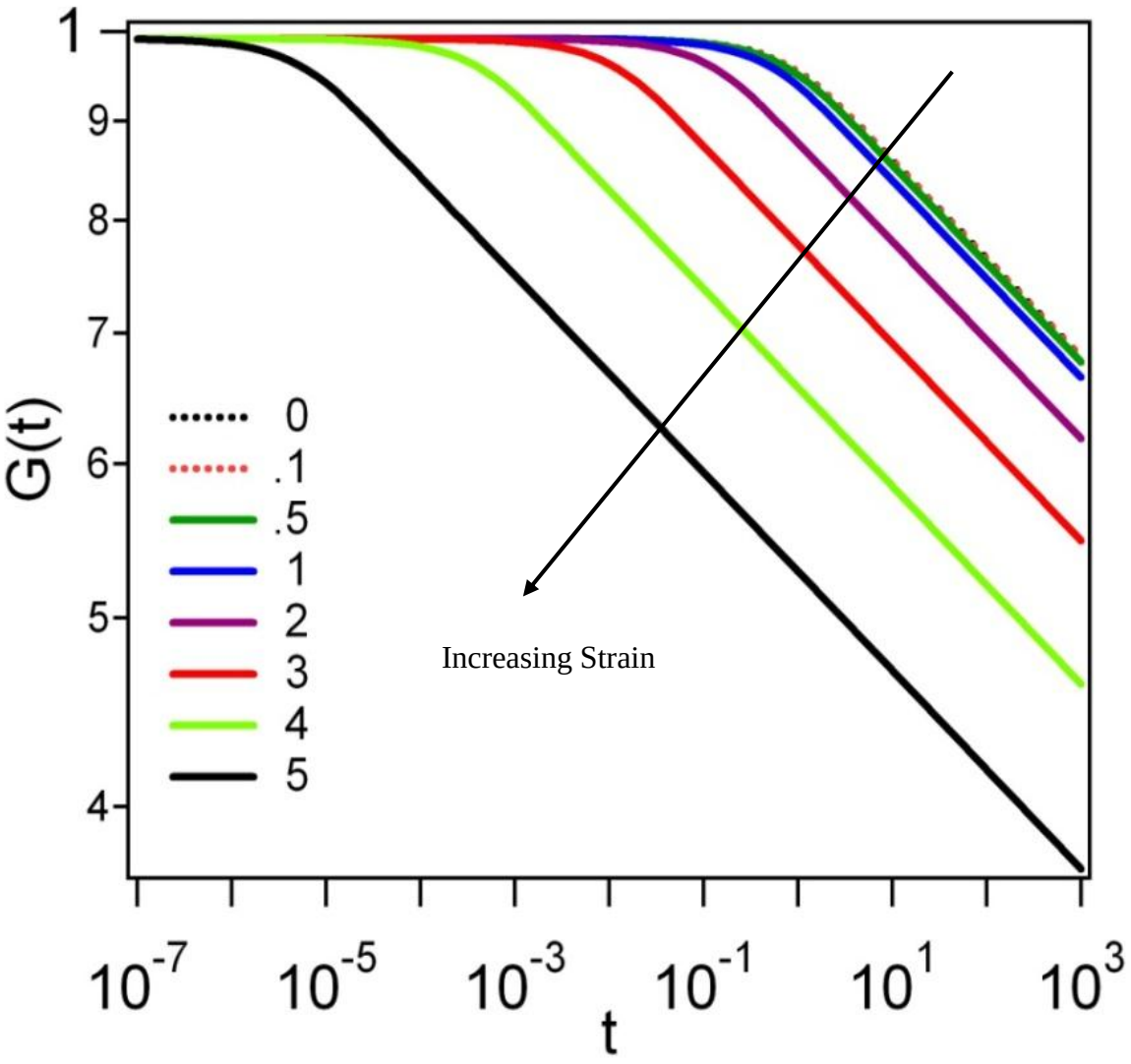

Figure 6.7 Relaxation modulus vs. time calculated from the SGR model for different strains. At higher strains, *G(t)* decays to the same value in smaller time.

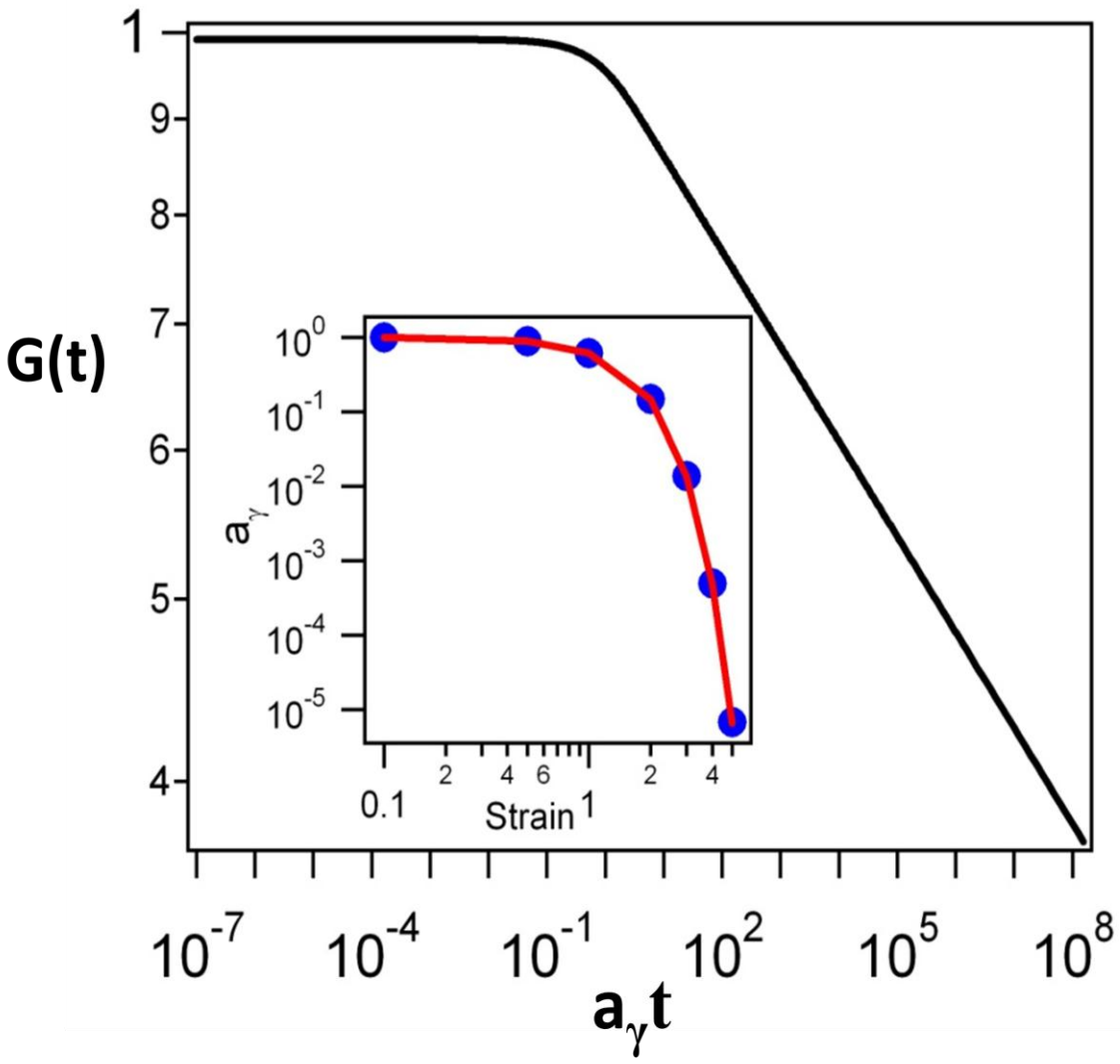

Figure 6.8 Master curve produced by superposition of the curves shown in 6.7. Inset shows shift factors vs. strain, solid line is fit to the expression given by *eq.* 6.5.

Further, we show that this form is consistent with the SGR model and originates from the elastic energy and its dependence on strain. Indeed, the remarkable agreement between the functional form of the experimentally determined $\tau(\gamma)$, (see fit in Figure 6.4 and *eq*. 6.2) and SGR model prediction (Figure 6.8, *eq.* 6.6) appears to validate the elastic energy based framework in the SGR model. The constant k in *eq*. 6.2 (obtained by fitting the SGR model to the data) is the effective spring constant for the system; it contains materialspecific information about the inter-particle interactions.

The appearance of a fast relaxation mode at high strain appears to be generic for our materials, but is not captured within the SGR framework. The possibility of a fast β relaxation processes in soft glasses has been discussed by Sollich [6], however, as pointed out by the author, such processes cannot be described within the low-frequency framework of the current SGR model. It can in fact be seen from Figure 6.7 that the short time response in this model is always elastic with $G = 1$ at all strains. Additionally whereas the experimental relaxation moduli are stretched exponential functions of time, the theoretical moduli are power-laws. We will discuss the origin of this discrepancy in a forthcoming article.

6.6 Conclusions

We have demonstrated both experimentally and theoretically that strain accelerates relaxation dynamics of self-suspended suspensions of SiO_2 nanoparticles densely grafted with polyisoprene chains, which manifest soft glassy rheology. In order to evaluate the generality of our findings, we performed similar experiments using suspensions of sterically stabilized SiO_2-PEG nanoparticles dispersed in oligomeric polyethylene glycol (PEG) hosts, as well as using self-suspended suspensions created by densely grafting PEG to silica nanoparticles [27]. As shown in

the appendix, both systems manifest soft glassy rheology and exhibit strain-accelerated dynamics qualitatively similar to what is observed for self-suspended SiO_2-PI. Our findings therefore suggest that strain-induced acceleration of relaxation dynamics is a generic feature of many soft glasses. That the phenomena are also predicted within the SGR framework, implies that it should be observed for all soft glasses governed by this framework.

ACKNOWLEDGEMENTS

This work was supported by Award No. KUS-C1-018-02, made by King Abdullah University of Science and Technology (KAUST), and by the National Science Foundation, Award No. DMR-1006323. Facilities available though the Cornell Center for Materials Research (CCMR) were used for this study.

REFERENCES

1. H. Eyring, J. Chem. Phys. **4**, 283 (1936).
2. H. Lee, K. Paeng, S. F. Swallen, M. D. Ediger, Science **323**, 231 (2009).
3. M. Warren, J. Rottler, Phys. Rev. Lett. **104**, 205501 (2010).
4. P. N. Pusey, W. van Megen, Nature **320**, 340 (1986).
5. T. G. Mason, D. A. Weitz, Phys. Rev. Lett. **75**, 2770 (1995).
6. P. Sollich, Phys. Rev. E. **58**, 738 (1998); P. Sollich et al., Phys. Rev. Lett. **78**, 2020 (1998).
7. S. M. Fielding, P. Sollich, M. E. Cates, J. Rheol. **44**, 323 (2000).
8. V. Kobelev, K. Schwiezer, Phys. Rev. E **71**, 021401 (2005).
9. Y. M. Joshi, R. K. Reddy, Phys. Rev. E **77**, 021501 (2008).
10. P. Agarwal, H. Qi, L. A. Archer, Nano Lett. **10**, 111 (2010).
11. H. M. Wyss et al. Phys. Rev. Lett. **98**, 238303 (2007).
12. H. Y. Yu, D. L. Koch, Langmuir **26**, 16801 (2010).
13. K. N. Pham et al., J. Rheol. **52**, 649 (2008); M. E. Hegelson, N. J. Wagner and D. Vlassopoulos, J. Rheol. **51,** 297 (2007).
14. J. L. Nugent, S. S. Moganty, L. A. Archer, Adv. Mater. **22**, 3677 (2010)
15. Q. Zhang, L. A. Archer, Langmuir **18**, 10435 (2002)
16. G. Yin, M. J. Solomon, J. Rheol. **52**, 785 (2008).
17. C. Derec et al. Phys. Rev. E **67**, 061403 (2003).
18. G. B. Mckenna, T. Narita, F. Lequeux, J. Rheol. **53,** 489 (2009).
19. R. Bandopadhyay, P. H. Mohan and Y. M. Joshi, Soft Matter **6,** 1462 (2010).
20. J. Mattson et al., Nature **462**, 83 (2009).

21. M. Cloitre, R. Borrega, F. Monti, L. Leibler, Phys. Rev. Lett. **90**, 068003 (2003).

22. P. A. O'Connell, G. B. Mckenna, Mech. Time-Depend. Mater **6**, 207 (2002).

23. M. Rubinstein, R. H. Colby, Polymer Physics (Oxford University Press, Oxford, 2003).

24. V. Viasnoff, F. Lequeux, Phys. Rev. Lett. **89**, 065701 (2002); V. Viasnoff, S. Jurine, F. Lequeux, Farady Discuss. **123**, 253 (2003).

25. D. Bonn et al., Phys. Rev. Lett. **89**, 015701 (2002).

26. F. Ozon et al., Phys. Rev. E **68**, 032401 (2003).

27. See appendix for the experimental data on the oligomer- and self-suspended SiO_2-PEG materials.

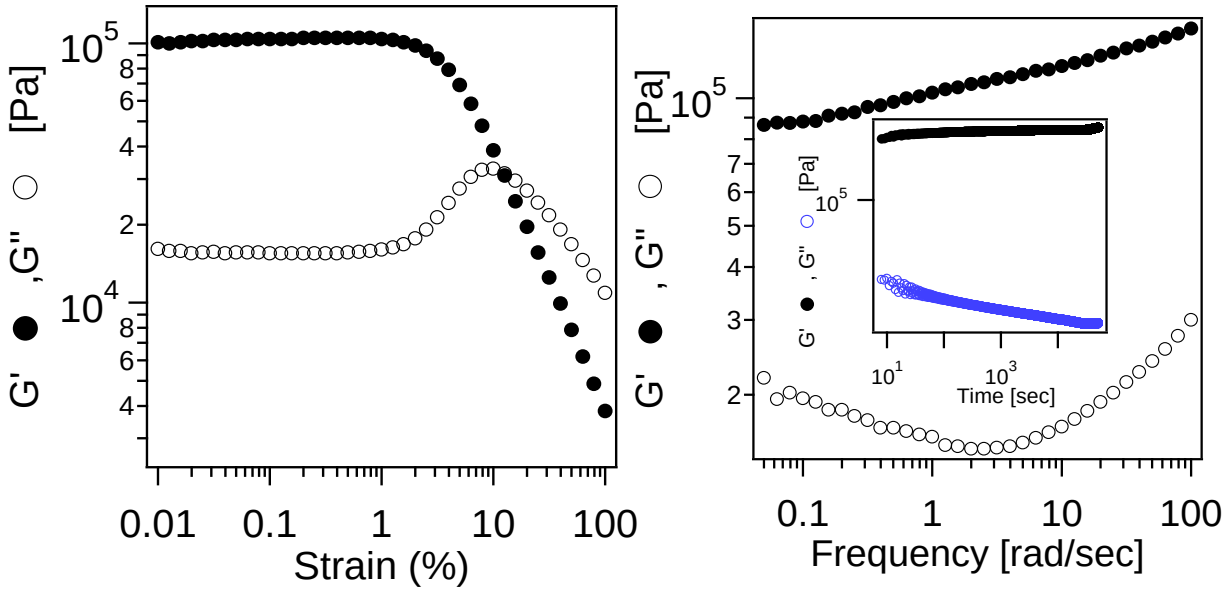

Supplementary figure 6.1 (a) Strain sweep at ω = 10 rad/sec and **(b)** frequency sweep measurement at γ = 0.5% for a suspension of silica nanoparticles sterically stabilized by PEG ($M_w \approx 660$ g/mol) and dispersed in low molecular weight ($M_w \approx 550$ g/mol) PEG. Volume fraction of silica nanoparticles ϕ = 0.30. Inset in (b) shows the time evolution of the viscoelastic moduli after the preshear, recorded at a frequency of 10 rad/sec and strain of 0.5 %. This and all subsequent measurements for this sample were carried out at 50 ˚C.

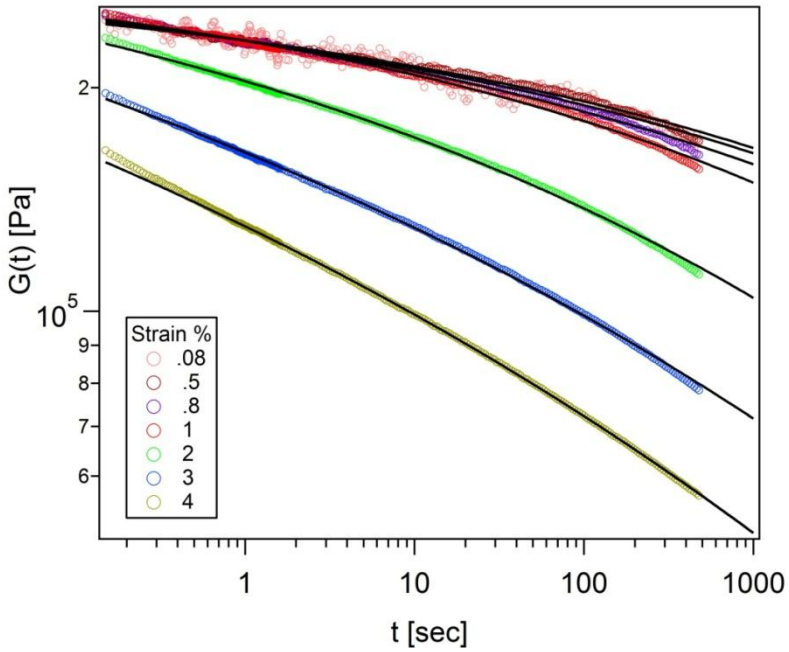

Supplementary figure 6.2 Relaxation modulus vs. time at different strains for the same material in supplementary figure 6.1. Solid lines are fits obtained using *eq.* 6.1.

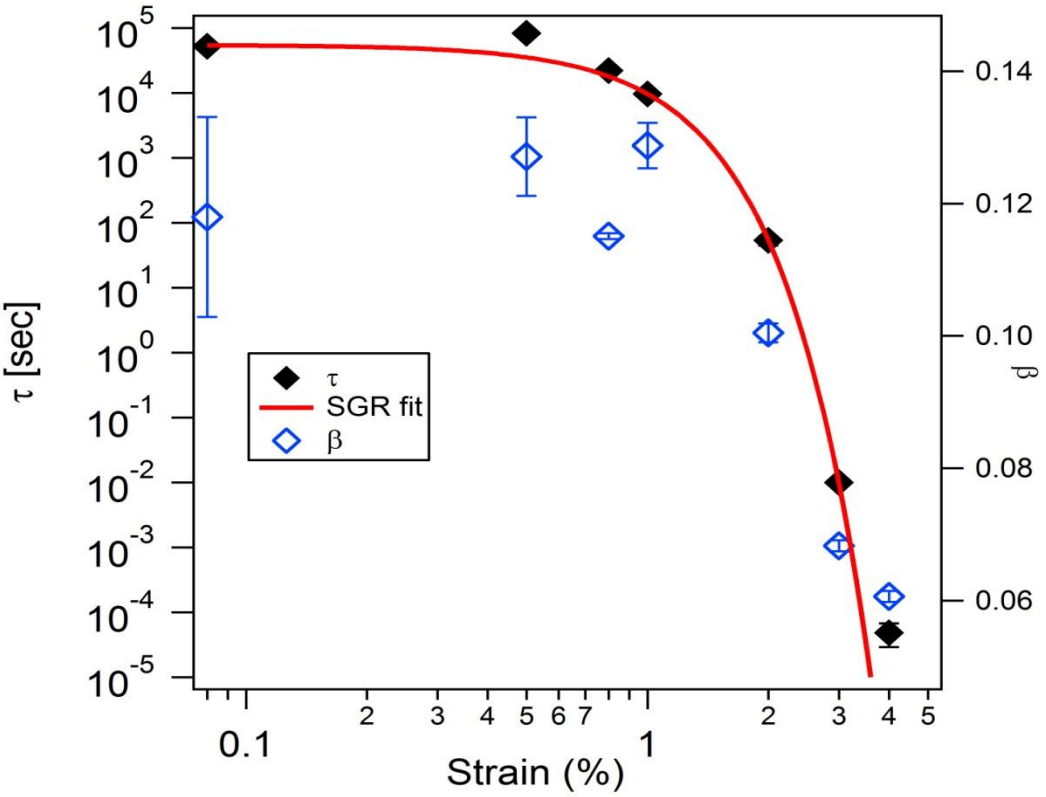

Supplementary figure 6.3 KWW fit parameters τ and β as a function of strain for the fits in supplementary figure 6.2. τ is again observed to decrease with increasing strain. Solid line is $\tau(\gamma)$ obtained using *eq.* 6.2 with $k = 1.7\text{x}10^4$ and $\tau_0 = 5.44\text{x}10^5$ sec.

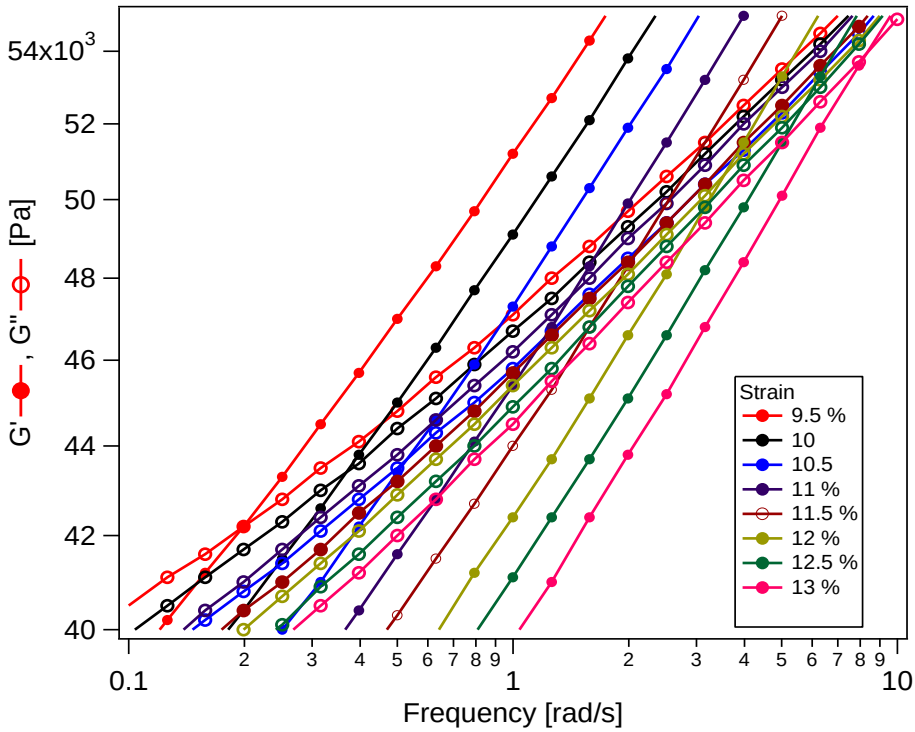

Supplementary figure 6.4 *G'* and *G"* as a function of frequency at different strains for the sample in supplementary figures 6.1-6.3 showing that the crossover frequency shifts to higher values with increasing strain.

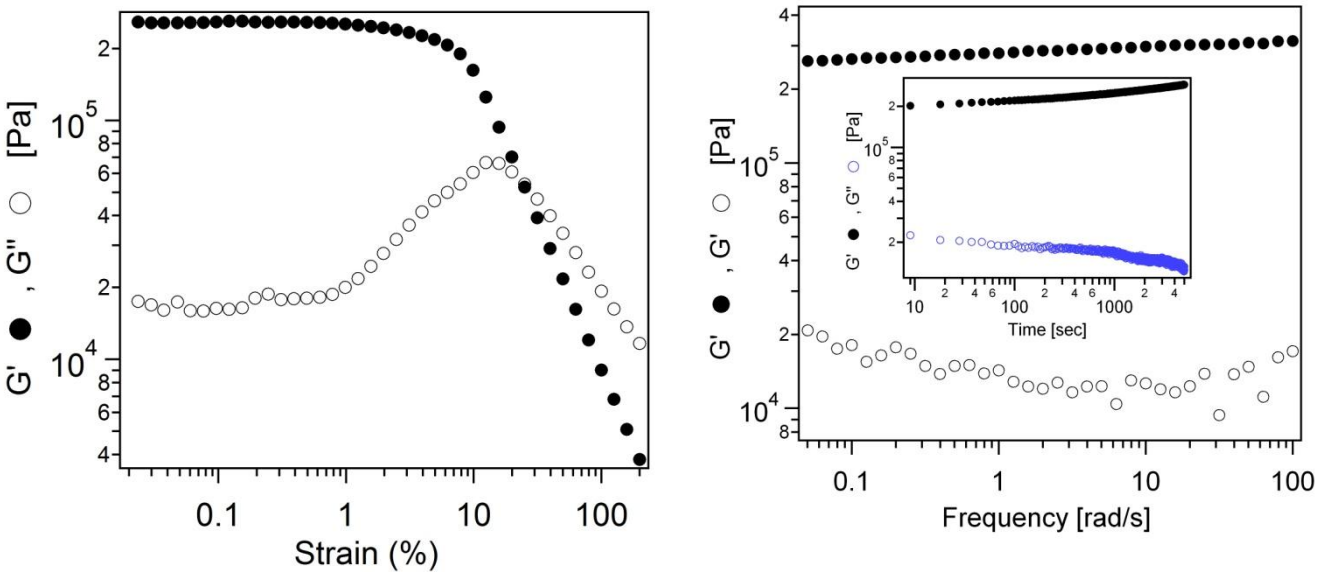

Supplementary figure 6.5 (a) Strain sweep at ω = 10 rad/sec and **(b)** frequency sweep measurement at γ = 0.01 % for a self suspended suspension of PEG tethered silica nanoparticles. Volume fraction of silica nanoparticle φ = 0.12. Inset in (b) shows the time evolution of the viscoelastic moduli after the preshear, recorded at a frequency of 3 rad/sec and a strain of 0.3 %. This and all subsequent measurements for this sample were carried out at 70 ˚C.

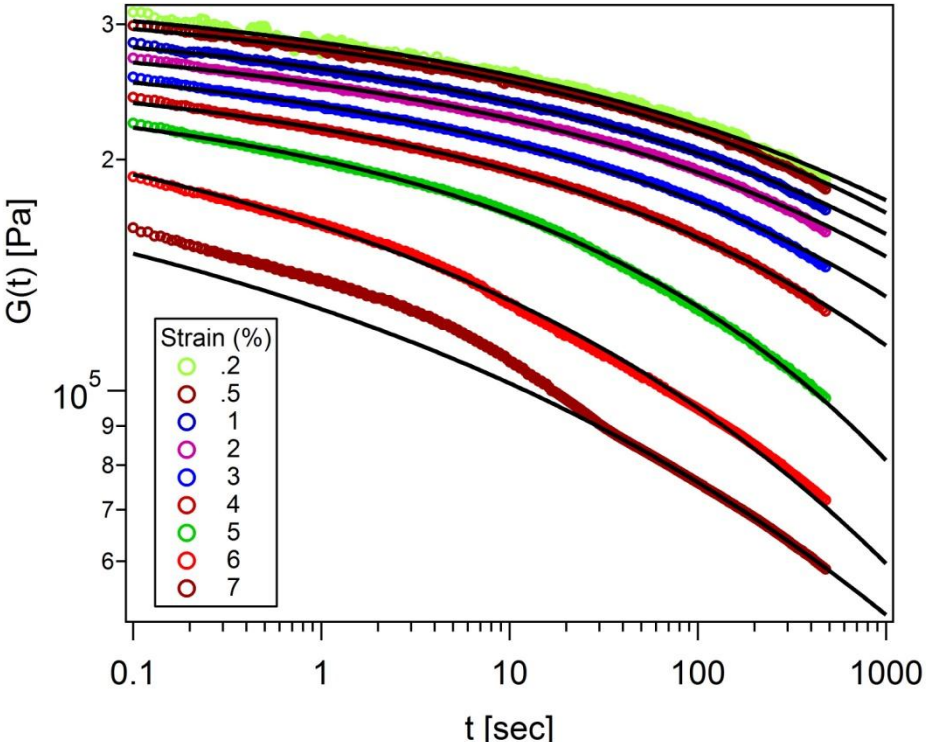

Supplementary figure 6.6 Relaxation modulus vs. time at different strains for the same material used for the experiments reported in supplementary figure 6.5. Solid lines are fits obtained using *eq.* 6.1.

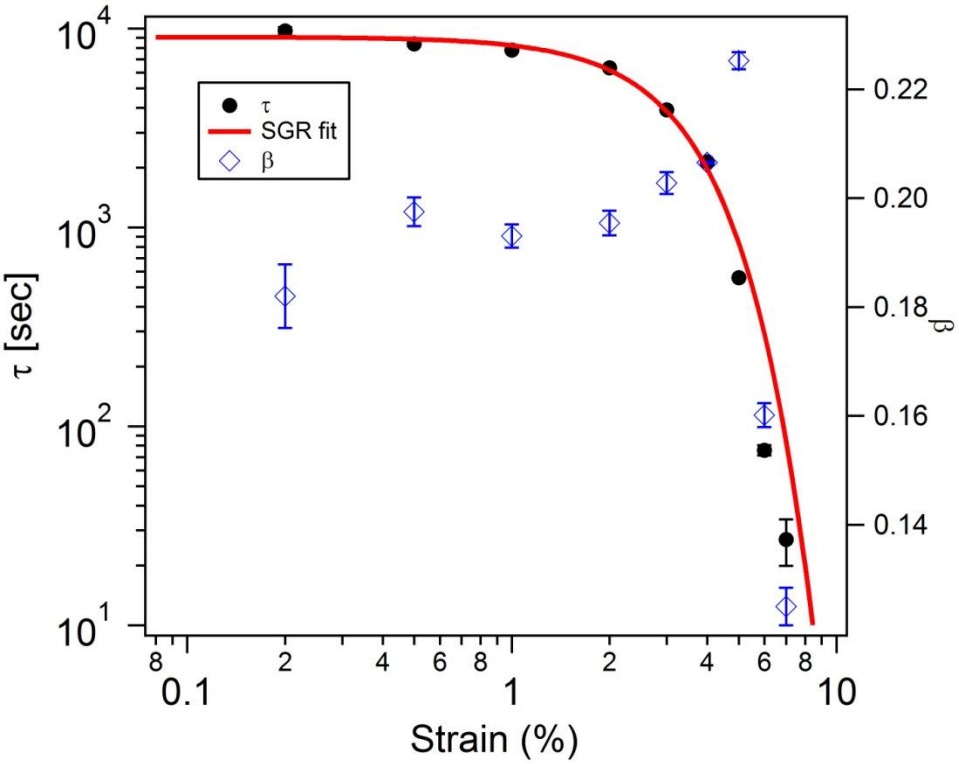

Supplementary figure 6.7 KWW fit parameters τ and β for fits in supplementary figure 6.6 as a function of strain. τ decreases with increasing strain. Solid line is fit with eq. 6.2 with k = 955.8 and τ_0 = 9054 sec.

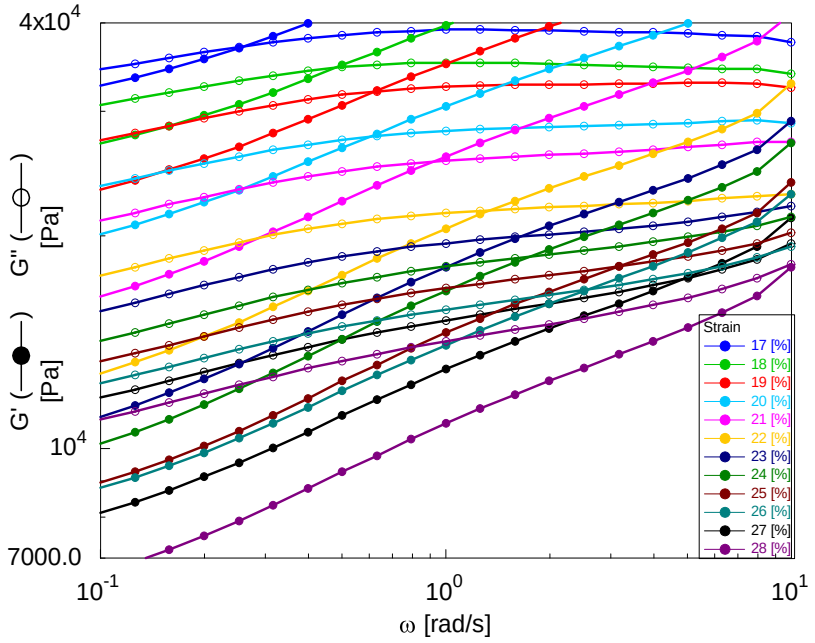

Supplementary figure 6.8 *G'* and *G"* as a function of frequency at different strains for the sample in supplementary figures 6.5-6.7. Crossover frequency shifts to higher and higher value with increasing strain. However, unlike the PI NIMs discussed before, the modulus at the crossover also decreases with strain.

CHAPTER 7

Nanoparticle Netpoints for Shape Memory Polymers

Reproduced with permission from

Angew. Chem. Int. Ed. **50**, 8670 (2011)

P. Agarwal, M. Chopra, L. A. Archer

7.1 Abstract

Shape memory polymers (SMP's) are a class of stimuli responsive materials which have the capacity to remember a pre-programmed shape imprinted during synthesis; can be reformed at a higher temperature to impart a desired temporary shape; and recover their original shape when acted upon by a stimulus, e.g. heat, light or magnetic field. Conventionally addition of nanoparticles as fillers in SMPs has resulted in slight improvement in their mechanical properties however at the same time deterioration of shape memory performance and broadening of the transition temperature. Here we report a new family of hybrid, inorganic-organic SMPs employing inorganic nanoparticles as netpoints where each netpoint is a junction for hundreds of polymer chains. We find that this network design leads to dramatic increase in the elastic modulus and yet sharp transition temperature and excellent shape memory properties of SMPs. Moreover this platform is capable of synthesizing SMPs with highly tunable mechanical properties and transition temperature.

7.2 Introduction

SMPs are attractive for a growing list of applications - from smart sutures and implants for minimally invasive surgery, to responsive, shape-shifting optical components [1, 2, 4-8]. Advantages that SMPs present over shape memory metal alloys [9, 10] range from their low density, more accessible and tailorable switching temperatures, lower cost, and flexibility [1-8]. Disadvantages of SMPs as compared to shape memory alloys involve low stresses generation due to their low elastic modulus [2, 4, 5]. There have been a very few reports on strong SMPs [11-13], however there still exists a need for a materials platform capable of synthesizing SMPs with high elastic modulus, excellent shape memory performance, tunable properties and multifunctionality [14-20].

SMPs typically consist of two elements: netpoints and switching segments [1, 2]. Netpoints are typically the connection points for polymer chains and are responsible for determining the permanent shape of the network and the switching segments are responsible for the shape memory effect due to entropic elasticity of the polymer chains. Netpoints can be chemical in nature, as in covalently connected polymer segments in cross-linked networks. They can also exist as physical cross-links, as has been realized in block copolymer based SMPs [1, 2]. For most covalent SMP networks reported in literature, netpoints are of molecular size; few known exceptions are the report by Xu et al. [21] where SMP's based on polyhedral oligosilsesquioxane (POSS) cores were demonstrated and Cao et al. [22] where nanoclay tethered SMPs were reported.

Recently we reported on a novel family of organic inorganic hybrids called nanoscale ionic materials (NIMs) [23-26]. Created by densely grafting functional oligomer chains, corona, to nanoparticle cores, these materials display fluid like properties in absence of any external solvent and have been termed as self-suspended suspensions [23, 24]. Physical properties of these materials such as viscosity, elastic modulus, glass transition and melting temperature can be facilely tuned by systematically changing the core volume fraction, corona molecular weight and grafting density [23-26]. Materials created from different nanoparticle core chemistry, size and shape have already been reported [23-26].

7.3 Results and Discussion

We have synthesized the hybrid polymeric networks by interconnecting the free ends of the NIMs corona. We demonstrate hybrid SMPs in the present work using the simplest configuration, NIMs comprised of a SiO_2 core and Polyethylene glycol (PEG) corona. A perhaps obvious advantage of these materials is that the inherent biocompatibility of the PEG corona [27]

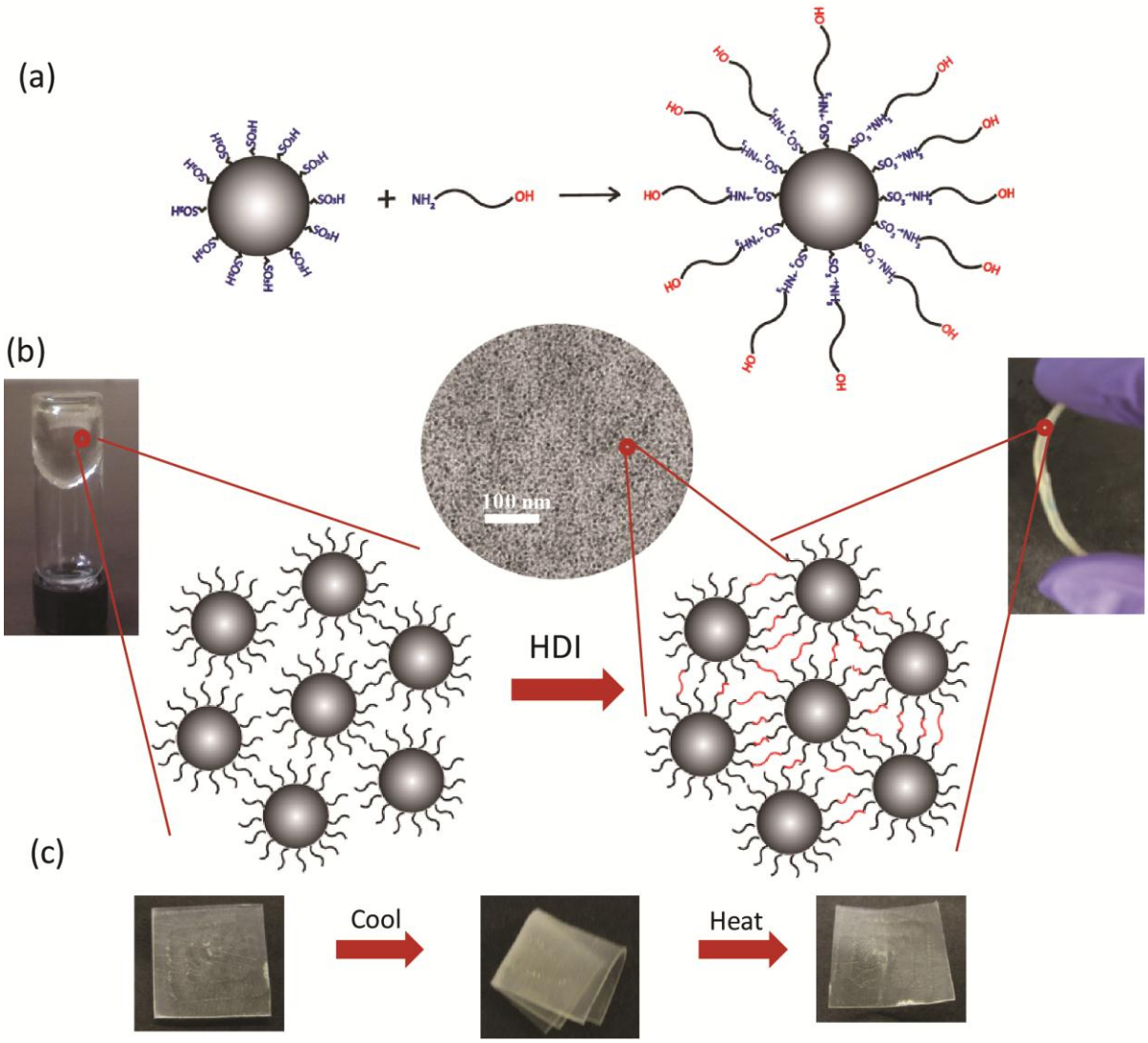

Figure 7.1 (a) Showing the schematic of the reaction scheme (b) Transformation of uncrosslinked, liquid like NIMs (left) to crosslinked solid SMP hybrids (right), Transmission Electron Microscope (TEM) picture of the SMP shows nanoparticles are well dispersed, size of the silica nanoparticles is 10 nm (c) pictures showing shape fixing and recovery, shape fixing is done at -10 ˚C and recovery is done at 60 ˚C.

and silica [28] cores immediately renders them attractive candidates for biomedical applications. In the synthesis scheme, silica nanoparticles are first grafted with sulfonic acid groups using the procedure reported previously [23, 25]. The resultant sulfonic acid functionalized particles are subsequently reacted with dual functional PEG chains containing amine and hydroxyl end groups. The tethered sulfonic acid reacts selectively with the amine groups to produce particles hydroxyl group at the end of tethered PEG chain as shown in the reaction scheme in Figure 7.1(a). As shown in figure 7.1(b), reaction of these particles with hexamethylene diisocynate (HDI) yields cross-linked polymer networks in which the SiO_2 cores of the NIMs are the netpoints. We have shown previously, that densely functionalized nanostructures comprised of as many as 1-2 polymer chains/nm^2 can be created using this approach [23], which translates up to 300 - 600 chains/particle for the 10 nm particle size use in this study. As illustrated in figure 7.1 (c) these materials manifest shape memory properties, wherein they can be cooled to remember their shape and when heated again, they quickly recover their original fixed shape.

Figure 7.2 shows the storage modulus vs. temperature for samples created using a PEG corona with a molecular weight of 5000 g/mol and polydispersity of 1.06. Particle content has been varied between different samples by changing the number of polymer chains attached to each particle and measured by thermogravimetric analysis (TGA). It can be clearly seen from the figure that the addition of particles results in a significant increase in both the rubbery and glassy moduli, and that there is a systematic increase with increasing the particle volume fraction. At a moderate particle volume fraction of 0.16, the rubbery modulus of the material is of the order 100 MPa at room temperature, which is substantially higher that the improvement in mechanical properties reported previously for SMP composites [6, 7], where typically the enhancement is comparatively modest.

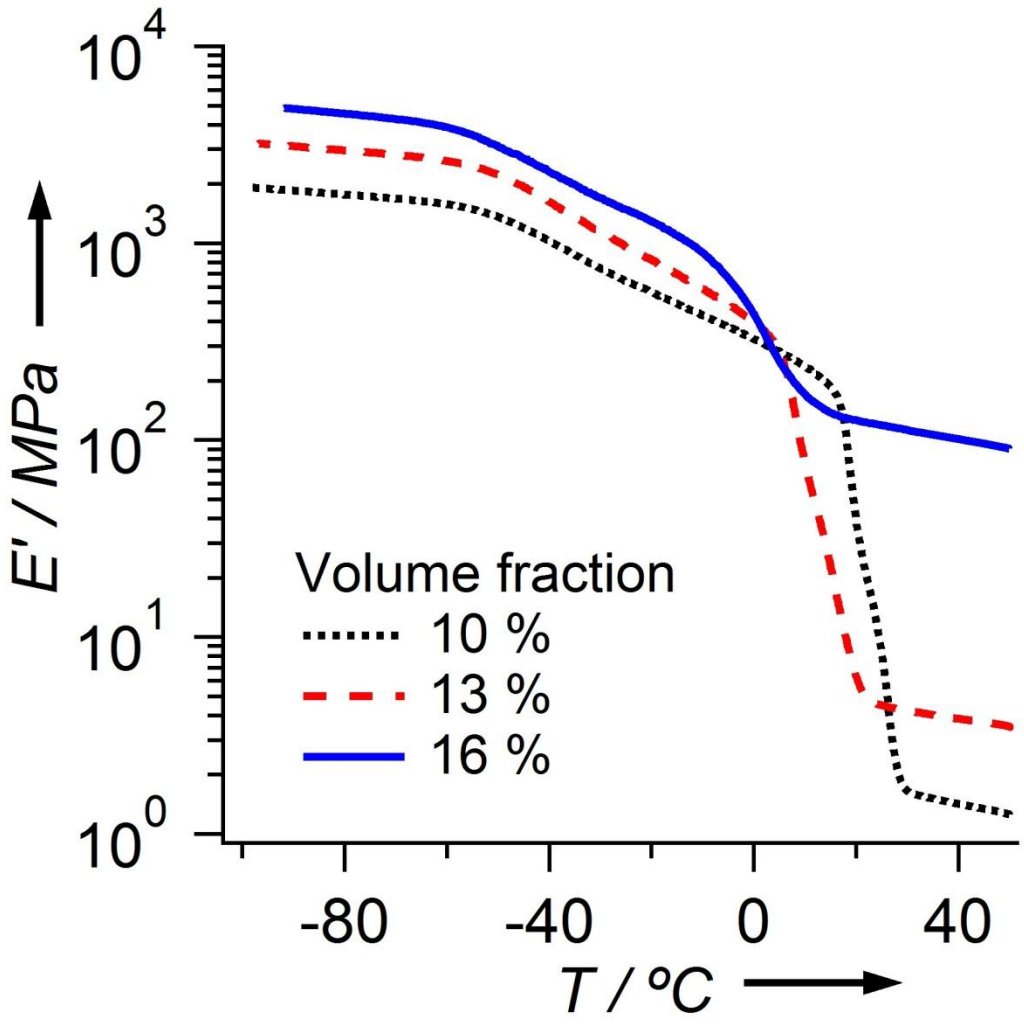

Figure 7.2 Elastic modulus vs. temperature for the SiO_2-PEG SMP samples with the corona molecular weight of 5000 with varying nanoparticle volume fraction.

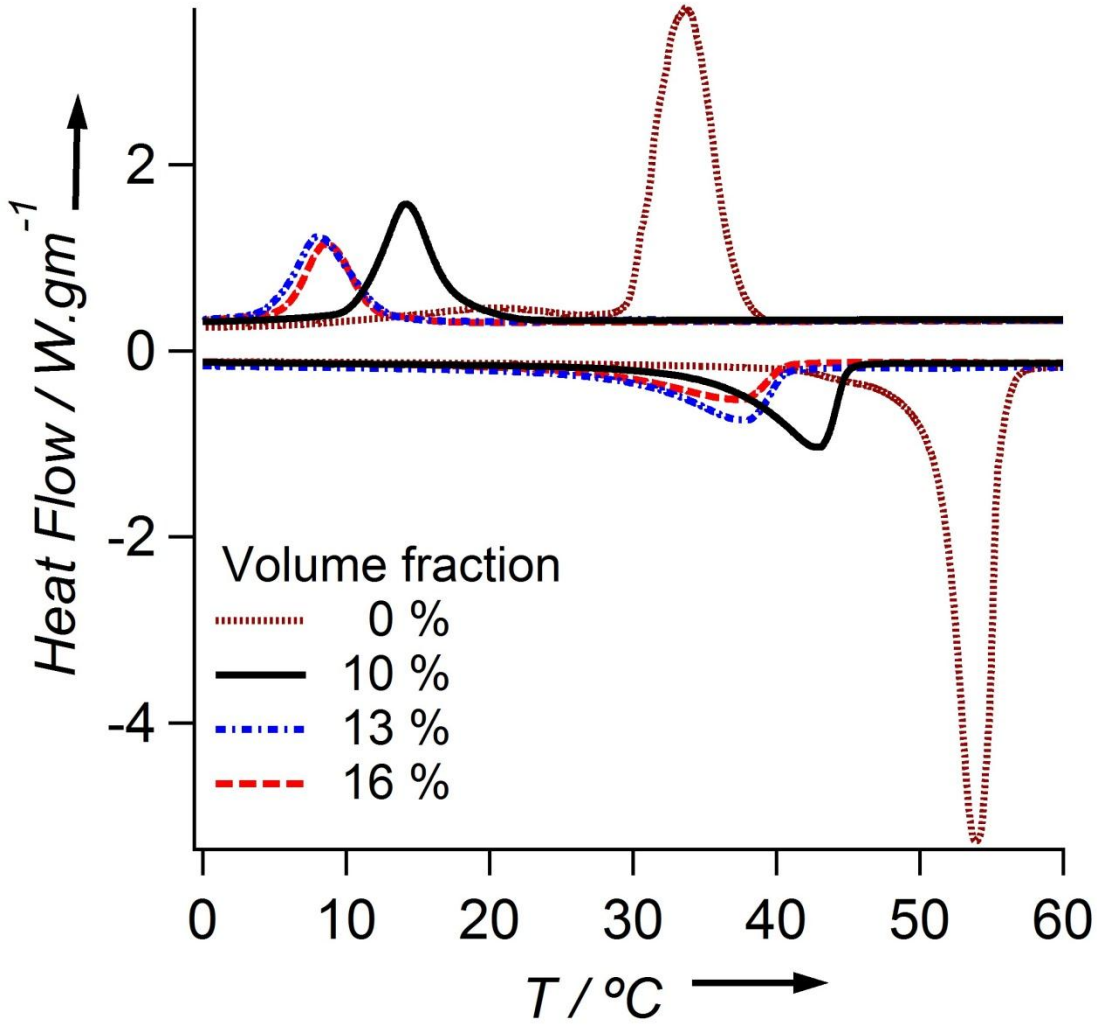

Figure 7.3 DSC traces for the samples in figure 7.2 and also of unattached NH_2 and OH terminated PEG.

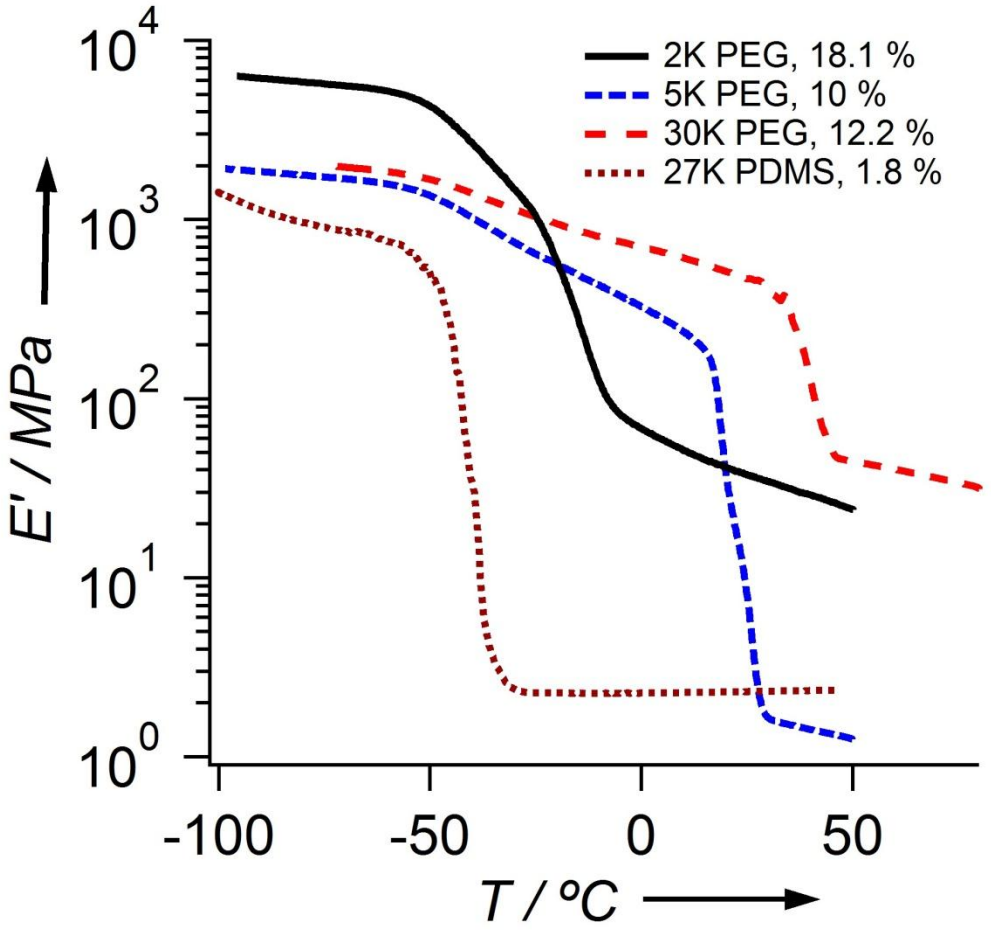

Figure 7.4 Elastic modulus, *E'*, vs. temperature for the hybrid SMPs created with varying corona chemistry, molecular weight and particle content.

Figure 7.3 shows the differential scanning calorimetry (DSC) traces for the same samples and also the untethered PEG. These results indicate that T_{trans} for the material is due to the melt-crystalline transition of PEG [29] chains anchored to the netpoints. During the cooling cycle, crystallization happens in a temperature range of 10 - 15 ˚C and during the heating cycle, the melting transition appears within the temperature range of 35 - 45 ˚C which is close to physiological temperatures and compares well with the typical transition temperature range of 20 ˚C to 80 ˚C for the SMPs reported in literature [1, 2]. As evident from both dynamic mechanical analysis (DMA) and DSC results, the transition from a rubbery state to a glassy state is very sharp in our materials. This is an important observation because a sharp transition temperature is crucial for quick shape recovery and fixity; it could be contrasted with the broad distribution of transition temperatures reported for SMP nanocomposites [4, 6, 7]. DSC results indicate that addition of particles leads to the reduction in the transition temperature and crystallinity of the hybrid SMP as compared to the free polymer which could possibly be explained by the fact that polymer chains are more constrained due to immobilization of both the chain ends.

Figure 7.4 shows the DMA results for hybrid SMPs created using a range of corona molecular weight and chemistry. It can be clearly seen that the modulus and transition temperature values can be tuned over a wide range by changing the corona molecular weight, chemistry and particle content. Figure also shows that the corona chemistry is not limited to PEG-based materials. Specifically, it is shown that SMPs based on polydimethyl siloxane (PDMS), are possible to synthesize. The figure clearly shows that both the storage modulus and transition temperature can be facilely manipulated by changing the corona chain molecular weight or chemistry. For samples having PEG as the tethered chain, the transition temperature corresponds to the melting transition, as mentioned before, whereas for the samples having PDMS as the tethered chain,

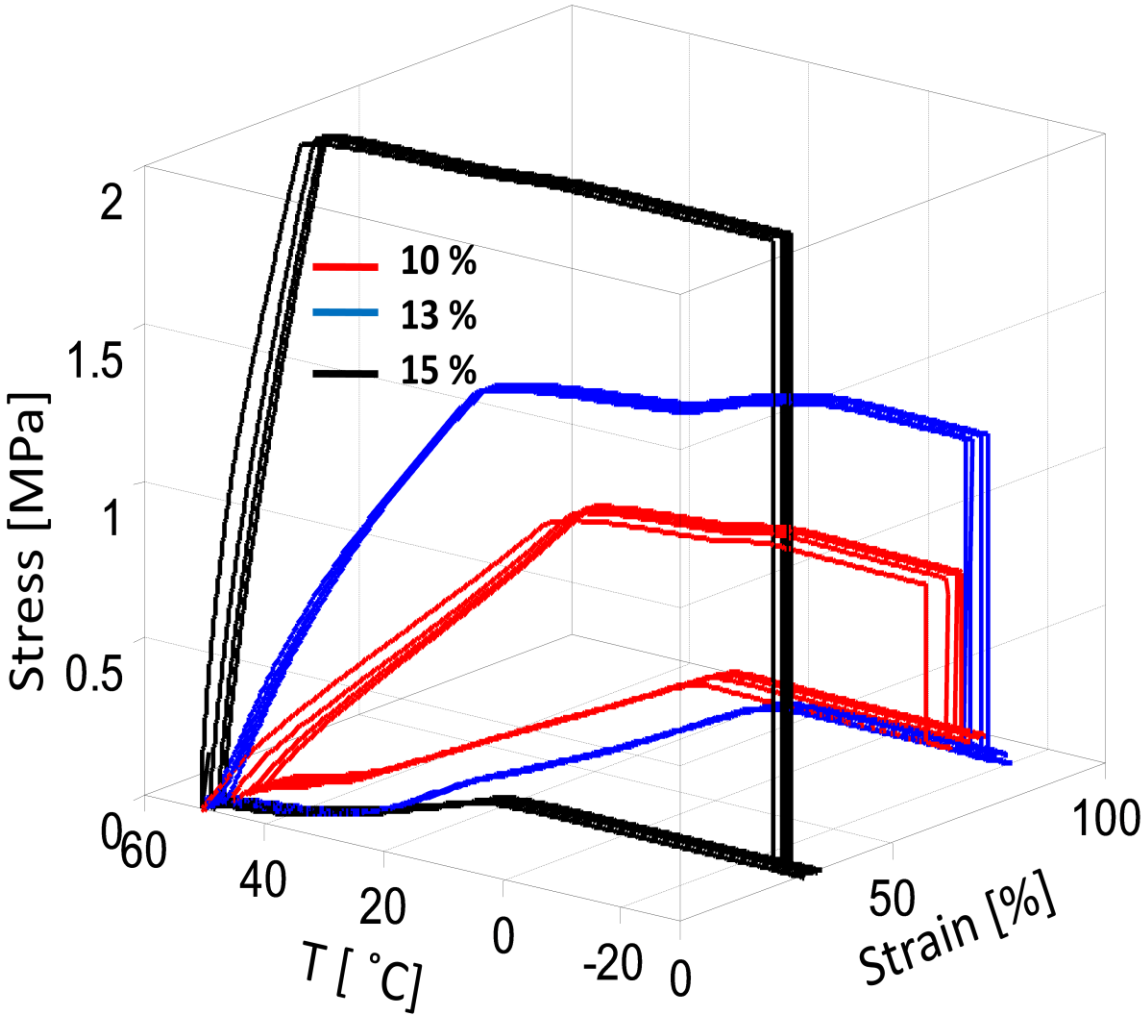

Figure 7.5 Cyclic thermomechanical tensile test results for SiO_2 PEG hybrids with variable core volume fraction. Molecular weight of the polymer chain is 5000 gm/mol.

transition corresponds to the glass transition.

SMP composites have been reported to suffer from a deteriorated shape memory performance upon addition of nanoparticles [7]. This observation can be speculated to stem from the fact that particulate fillers can act as defects within the network structure and thereby destroy its symmetry. Another possibility could be the loss of elastic energy due to frictional dissipation arising from polymer filler interaction. This drawback is not seen in the hybrid SMPs reported here presumably because nanoparticles which provide mechanical reinforcement are acting as junction points for the network branches. We have characterized the shape memory performance of the materials shown in figure 7.2 using cyclic thermo mechanical analysis as shown in figure 7.5. In these tests, the material is first stretched at a temperature higher than T_{trans} and then cooled below T_{trans} at the fixed stress to fix the shape. Stress is then reduced to zero and the decay of the strain during this step characterizes shape fixity; it is apparent from the figure, there is no noticeable decay in the strain implying that these materials have good shape fixity. For the recovery, the material is heated to a temperature above T_{trans} and shape recovery is characterized by recovery of strain under stress free conditions. It can be seen from the figure that during this process, the strain recovers almost fully implying that these materials are able to recover to their original shape. This process is repeated for multiple cycles and shows that the materials possess good shape fixity and recovery after multiple cycles of loading and unloading. Values of the shape fixity and recovery ratios along with various physical other properties are provided in Table 7.1.

Table 7.1 Summary of physical properties of samples reported in Figure 7.2 and 7.5

φ (%)	T_c [˚C]	T_m [˚C]	E_g [GPa]	E_r [MPa]	R_f (%)	R_r (%)	σ_r [MPa] (50 ˚C)	ε_r [%] (50 ˚C)	σ_r [MPa] (0 ˚C)	ε_r [%] (0 ˚C)
10	15	43	1.9	1.6	98.5	98.3	0.48	223	8.3	7.1
13	8	38	3.2	4.9	99.5	99.4	3.0	207	9.0	16.1
16	8	37	4.8	126	97.0	96.8	8.8	95	11.5	25

φ is the volume fraction of silica nanoparticles.

T_c the crystallization temperature of PEG chains determined from DSC.

T_m is the melting temperature of PEG chains determined from DSC.

E_g is the glassy modulus determined from DMA.

E_r is the rubbery modulus determined from DMA.

R_f is the shape fixity ratio.

R_r is the shape recovery ratio.

σ_r is the stress at break.

ε_r is the elongation at break.

7.4 Conclusions

In conclusion, we have presented a novel material platform for synthesizing hybrid shape memory polymers which incorporates nanoparticles as netpoints. Advantages presented by this material design involve significant increase in the elastic modulus, sharp transition temperature and excellent shape memory properties. Issues stemming from immiscibility of filler nanoparticles in the polymer matrix are inherently avoided in these materials by tethering the polymers to the nanoparticle core. These materials open up the potential for strong, biocompatible SMPs with continuously tunable mechanical properties and transition temperatures, as well as high shape memory performance. By taking advantage of the large available libraries of available nanoparticle shapes, sizes, chemistries, and mass distributions [30], our materials provide a facile framework for creating SMPs with multifunctional features like remote actuation, biodegradability and drug release capabilities [14-20].

7.5 Experimental

Synthesis of end functionalized NIMs: Commercially available silica nanoparticles (LUDOX-SM30) (Sigma Aldrich) were functionalized with sulfonic acid using the chemistry reported previously [25]. α-amino ω-hydroxy terminated PEG (Polymer source inc.) was added to the sulfonic acid functionalized particles and the mixture was allowed to react for a few days. Amine end of the polymer reacts with the sulfonic acid group on the particles and the product contains PEG tethered silica nanoparticles with a free hydroxyl group at the chain end. Product was dried afterwards and the excess polymer was removed by dissolving the sample in chloroform and doing a repeated precipitation with hexane. For the samples involving PDMS similar method was employed with a diamino functionalized PDMS (Sigma Aldrich) and the

purification was done by precipitation with methanol. Particle weight fraction in the sample was characterized by doing thermogravimetric analysis (TGA).

Synthesis of SMP: For crosslinking, the product was dissolved in chloroform and reacted with excess hexamethylene diisocyanate (HDI) (Sigma Aldrich). Solution was then poured into the Teflon molds and the solvent was evaporated by slowly heating at 70 ˚C to create SMPs with silica nanoparticle as netpoints.

SMP Characterization: Elastic modulus of the sample was measured as a function of temperature by cutting a rectangular film from the sample. Sample was cooled at a rate of 3 ˚C/min and a small deformation was applied at a frequency of 1 Hz. DSC was performed in heat cool heat cycle at a heating and cooling rate of 5 ˚C/min from a temperature range of 100 ˚C to -50 ˚C. Shape memory performance was evaluated by cyclic thermomechanical test in stress control mode. Sample was stretched up to a certain strain at 50 ˚C, then keeping the stress constant sample was then cooled to -20 ˚C for 10 % and 13 % volume fraction sample and to -30 ˚C for the 16 % volume fraction sample. Shape fixity was evaluated from the decrease in the value of strain under stress free conditions. Shape recovery was quantified from the recovery of strain during heating the sample to 50 ˚C under stress free conditions.

Instrumentation: DMA was performed on TA instrument model Q800 with a tension clamp. DSC was performed on TA instruments model Q2000 in heat cool heat cycle with liquid nitrogen as coolant. TGA was done by TA instruments model Q5000 under Nitrogen flow. For TEM imaging, sample was sectioned into thin sections using Leica Ultracut-UCT microtome and TEM was performed using FEI Technai T12 at 120 kV.

ACKNOWLEDGEMENTS

This work was supported by Award No. KUS-C1-018-02, made by King Abdullah University of Science and Technology (KAUST), and by the National Science Foundation, Award No. DMR-1006323. Facilities available though the Cornell Center for Materials Research (CCMR) were used for this study.

REFERENCES

1. A. Lendlein, A. M. Scmidt, R. Langer, Proc. Nat. Acad. Sci. **98**, 842 (2001); A. Lendlein, S. Kelch, Angew. Chem. Int. Ed.**41**, 2034 (2002).
2. C. Liu, H. Qin, P. T. Mather, J. Mater. Chem. **17**, 1543 (2007); P. T. Mather, X. Luo, R. Rousseau, Annu. Rev. Mater. Res. **39**, 441 (2009).
3. M. A. Cohen Stuart et al. Nat. Mater. **9**, 101 (2010).
4. P. Miaudet et al., Science **318**, 1294 (2007).
5. X. Luo, P. T. Mather, Soft Matter **6**, 214 (2010).
6. Y. Liu, K. Gall, M. L. Dunn, P. McCluskey, Mechanics of Materials **36**, 929 (2004).
7. S. A. Madbouly, A. Lendlein, Shape Memory Polymers **226**, 41 (2010).
8. A. T. Neffe, B. D. Hanh, S. Steuer, A. Lendlein, Adv. Mater. **21**, 3394 (2009).
9. L. C. Chang, T. A. Read, J. Met. **47**, 191 (1951).
10. W. J. Buehler, J. V. Gilfrich, R. C. Wiley, J. Appl. Phys. **34**, 1475 (1963).
11. T. Xie, I. A. Rousseau, Polymer **50**, 1852 (2009).
12. J. S. Leng, X. Lan, S. Y. Du, W. M. Huang, N. Niu, S. J. Phee, Q. Yuan, App. Phys. Lett. **92**, 014104 (2008); J. S. Leng, X. Lan, Y. Liu, S. Du, Smart. Mater. Struct. **18**, 074003 (2009).
13. Q. Cao, P. Liu, Polym. Bull. **57**, 889 (2006).
14. A. Lendlein, H. Jiang, O. Junger, R. Langer, Nature **434**, 879 (2005).
15. R. Mohr, K. Kratz, T. Weigel, M. L. Gabor, A. Lendlein, Prot. Natl. Acad. Sci. **130**, 3540 (2006).
16. H. Koerner, G. Price, N. A. Pearce, M. Alexander, R. A. Vaia, Nat. Mater. **3**, 115 (2004).

17. A. Lendlein, R. Langer, Science **296**, 1673 (2002).

18. T. Xie, Nature **464**, 267 (2010).

19. X. Luo, P. T. Mather, Adv. Func. Mater. **20**, 2469 (2010).

20. M. Behl, I. Bellin, S. Kelch, W. Wagermaier, A. Lendlein, Adv. Func. Mater **19**, 102 (2009); J. Zotmann, M. Behl, D. Hofmann, A. Lendlein, Adv. Mater. **22**, 3424 (2010); I. Bellin, S. Kelch, R. Langer, A. Lendlein, Prot. Natl. Aca. Sci. **103**, 18043 (2006).

21. J. Xu, J. Song, Prot. Natl. Acad. Sci. **107**, 765 (2010).

22. F. Cao, S. C. Jana, Polymer **48**, 3790 (2007).

23. P. Agarwal, H. Qi, L. A. Archer, Nano Lett. **10**, 111 (2010).

24. H. Y. Yu, D. L. Koch, Langmuir **26**, 16801 (2010).

25. R. Rodriguez, R. Herrera, L. A. Archer, E. P. Giannelis, Adv. Mater. **20**, 4353 (2008).

26. A. B. Bourlinos et al., Adv. Mater **17**, 234 (2005); A. B. Bourlinos et al., Adv. Func. Mater **15**, 1285 (2005); A. B. Bourlinos et al., Small **2**, 513 (2006).

27. C. M. Yakacki, R. Shandas, D. Safranski, A. M. Ortega, K. Sassaman, K. Gall, Adv. Func. Mater. **18**, 2428 (2008).

28. P. T. Knight, K. M. Lee, H. Qin, P. T. Mather, Biomacromolecules **9**, 2458 (2008).

29. J. Brandrup, F. H. Immergut, Polymer Handbook (3rd ed. New York, Wiley, 1989).

30. X. W. Lou, L. A. Archer, Z. C. Yang, Adv. Mater. **20**, 3987 (2008).